FIELD ION MICROSCOPE STUDIES ON SURFACE ENERGY ANISOTROPY AND FACETING BEHAVIOR OF METALS

A THESIS

Presented to

The Faculty of the Division of Graduate

Studies and Research

by

Rajinder Kumar

In Partial Fulfillment

of the Requirements for the Degree

Doctor of Philosophy in the School

of Chemical Engineering

Georgia Institute of Technology

August, 1974

FIELD ION MICROSCOPE STUDIES ON SURFACE ENERGY ANISOTROPY AND FACETING BEHAVIOR OF METALS

Approved:

Chairman

Date Approved by Chairman: 7/8/24

ACKNOWLEDGMENTS

I am highly indebted to Dr. Helen E. Grenga, my thesis advisor, for her continued encouragement and guidance in this research. Had it not been for her this work would have never come to fruition. I am grateful to Dr. R. F. Hochman and Dr. B. G. LeFevre for review and constructive criticism of this work.

I express my appreciation for a pleasant working relationship with the faculty and fellow graduate students in the Metallurgy Program at Georgia Tech. I wish to thank Mr. Charles A. Blackwood and Mr. James Nabors of Georgia Tech, and Mr. S. B. McLane of Pennsylvania State University for helping me turn my designs into reality.

To my friend, Mr. Shashi Tiwari, I extend my special thanks for helping me with the computer programs. Mr. Kamal Jeet Singh was very helpful in the preliminary analyses of some of the results and in final proof-reading of this work.

I gratefully acknowledge the support of School of Chemical Engineering at Georgia Tech and the National Science Foundation, which have allowed me to pursue this work.

The unselfish consideration of my brother, Chander Mohan, and his wife, Shobha, who contributed to my morale, is deeply appreciated. To their children, Bemu and Sanjay, I extend my love for filling my spare hours with joy. Last, but not least, I have high gratitude and admiration for my parents for encouraging, through letters, my efforts for further accomplishments.

TABLE OF CONTENTS

TABLE OF CONTENTS (Continued)

TABLE OF CONTENTS (Continued)

TABLE OF CONTENTS (Continued)

LIST OF TABLES

LIST OF ILLUSTRATIONS

LIST OF ILLUSTRATIONS (Continued)

LIST OF ILLUSTRATIONS (Continued)

SUMMARY

The purpose of this work was to study the faceting behavior of iridium, tungsten, iron and platinum in vacuum and in hydrogen and to determine their surface energy anisotropies. High purity metals were annealed in the selected environment and observed with field-ion microscopy. From the size of the resulting facets, the surface energy anisotropy was calculated.

The observed anisotropies in vacuum were compared with those predicated by Morse and Mie potentials, and pairwise bonding theory. For iridium and platinum the best fit was found with the pairwise bonding theory with $\sigma_2=0.4$, $\sigma_3=0.2$ and $\sigma_2=0.3$, $\sigma_3=0$, respectively. For tungsten and iron the results were in close agreement with those predicted by Mie potential calculations with m=5, n=7, and m=6, n=12, respectively. The maximum anisotropy values were found to be 8.8, 4.3, 6.6, 16.8% for iridium, tungsten, iron and platinum, respectively.

The facets formed in hydrogen were generally larger than those formed in vacuum under the same annealing conditions. The higher growth rate was attributed to a weakening of the metal-metal bond energy, and therefore a lowering of the surface energy. For iridium and tungsten, hydrogen lowered the surface energy of the closest packed planes by more than 1%, which is a significant value for these calculations. For iron, the surface energy of (110) planes was lowered by approximately 14%.

The growth rates of iridium (111) and tungsten (110) facets were measured in vacuum, and it was found that the changes in facet sizes

were proportional to $t^{0.36}$ and $t^{0.315}$, respectively, and the facet sizes were proportional to $t^{0.20}$ in both cases.

The activation energies for growth of iridium (111) and tungsten (110) facets were also found to be 45.7 and 54.5 k cal/mole, respectively. These activation energies can be explained as the result of a surface diffusion mechanism in which detachment of atoms from kink sites is the rate controlling step.

CHAPTER I

INTRODUCTION

Many areas such as physics, chemistry and materials science encounter the need to understand properties of metal surfaces. The surface free energy, which is one of these properties is closely related to the strength of materials. The surface energy is the energy required to create a unit area of the new surface. Since the surface depends upon the crystallographic orientation, the surface energy of a metal is also orientation dependent. Hydrogen environments are known to affect the mechanical properties of metals, and the effect of hydrogen on the surface energy is one of the mechanisms invoked to explain the mechanical property changes. However, there is no information available in the literature concerning the effect of hydrogen on the surface energy of metals.

The present studies were undertaken to determine the surface energies of several metals and the effect of hydrogen on the surface energy. Field-ion microscopy was chosen for these studies because of the high degree of surface cleanliness that can be obtained and the large number of orientations that can be observed simultaneously by this technique.

The imaged end forms after annealing in vacuum are used to calculate the surface energy anisotropy of single crystal planes. The effect of hydrogen is assessed from additional annealing experiments.

Information concerning the kinetics of faceting is also obtained from growth rate and activation energy measurements and a mathematical model is proposed to explain faceting on field-ion specimens. A computer program is used to predict growth rate curves from the model and these curves are compared with the observed growth rate curves.

CHAPTER II

LITERATURE SURVEY

The object of this chapter is to review briefly the principles that control the morphology of solid surfaces approaching equilibrium and to summarize briefly the previous experimental work in this area. The lowering of the surface energy is generally recognized as the driving force for morphological changes of metals at elevated temperatures. The mechanism by which these changes are accomplished, however, may vary depending on the experimental conditions. Possible mechanisms include[1]:plastic or viscous flow, evaporation and condensation, volume diffusion and surface diffusion. The experimental conditions used in the present studies are those for which surface diffusion has been established[2,3] as the dominant mechanism. Therefore, only the surface diffusion mechanism is considered. The literature on surface energy and surface diffusion studies is voluminous, and only those studies most pertinent to the present work are included.

A. Surface Energy

It is well recognized that the surface atoms of a metal differ from those of the bulk. This arises due to the fact that a surface atom is bonded only to other atoms in the same plane and below it. The general assumption that a surface atom has the ability to form additional bonds leads to the expression of "unsaturated valencies" of surface atoms. The energy thus associated with the surface is called the surface

free energy. Surface energy is a thermodynamic quantity and is equal to the energy required to create a unit area of the surface under conditions of constant temperature, volume and chemical potentials.[4] In a one component system it is called the specific surface free energy.

1. Theoretical Calculations

Surface energy may be expressed[5] as a sum of the energies of broken bonds associated with surface atoms. The bond energy of a surface atom depends upon the number and position of neighboring atoms, and the surface energy of metals therefore varies with crystal orientation.

The absolute values of surface energy of various orientations is difficult to obtain because the interatomic bond strength is not precisely known. However, theoretical calculations have been made for the ratio of surface energies of various orientations of face-centered (FCC) and body-centered (BCC) cubic crystals. There are many ways[6-10] to develop these values, but in the present work the method used by Drechsler and Nicholas[10] is adopted. According to Drechsler and Nicholas, the surface energy anisotropy (λ_{hkl}) of a particular plane (hkl) is the ratio of its surface energy, γ_{hkl}, to that of the closest packed planes, that is,

$$\text{for FCC crystals; } \lambda_{hkl} = \gamma_{hkl}/\gamma_{111}, \text{ and}$$

$$\text{for BCC crystals; } \lambda_{hkl} = \gamma_{hkl}/\gamma_{110}.$$

The maximum anisotropy is the ratio of maximum surface energy to minimum surface energies, i.e.

$$\lambda_{max} = \gamma_{max}/\gamma_{min}.$$

There are basically two methods currently available to calculate bond energies of surface atoms and the resulting surface energy anisotropies: i) Morse and Mie potentials, and ii) pairwise bonding theory. These methods are thoroughly discussed in the references cited below, and only a brief account is given here.

a. Morse and Mie Potentials. Drechsler and Nicholas[10] have used the following potentials to calculate the bonding energies of surface atoms:

$$\text{Morse:} \quad E(r)/E_o = \left[1-\exp \{-a(r-r_o) / r_o\} \right]^2 - 1$$

$$\text{Mie:} \quad E(r)/E_o = \{n(r_o/r)^m - m(r_o/r)^n\}/(m-n), \text{ with } n > m$$

where a,m,n = variable parameters,

$E(r)$ = the interaction energy for two atoms, r distance apart,

E_o = the maximum interaction energy, and

r_o = separation distance for maximum interaction energy.

No particular values were assigned to E_o, since the results were used only to calculate the surface energy anisotropies. However, the value of r_o was also adjusted to minimize the total lattice energy of a perfect unstrained crystal at 0^oK. The calculations were also made for crystals in which the lattice parameter deviated up to $\pm$ 2.5% from the ideal value to account for temperature (expanded lattice) and pressure (contracted lattice) effects on the surface energy. The surface energy anisotropy was found to be dependent upon the values chosen for a,m and n. These calculations took into account the interactions between all

first nearest neighbors only and included about fifty surface orientations. The calculations for the surface energy of FCC crystals, show that the surface energies of high index planes, such as (210) and (311) are always greater than those of the lower index planes, such as (111), (100) and (110). The order of increasing surface energy within these low index planes varies depending upon the values selected for a or m and n. Similar calculations for BCC crystals show that the surface energy of (211) planes is greater than those of the (110) and (100) planes.

The calculated anisotropies were used to determine the equilibrium shapes of FCC and BCC crystals and these results were compared with shapes of well annealed field emitters. A qualitative agreement was found with Morse potential for all metals investigated. However, quantitative agreement was claimed with a Mie potential for molybdenum, tungsten, vanadium and α -iron, using m=5 and n=7,8; for tantalum and niobium, using m=4.5 and n=8-14; and for nickel, using m=4.5 and n=7.

b. Pairwise Bonding Theory. In the pairwise bonding theory the dependence of nearest neighbor bond energies on interatomic distance is not considered, and no equation is given to calculate individual bond energies. The rather simplified assumption is that one can directly compare the number and type of nearest neighbor bonds in order to obtain surface energy anisotropies. Mackenzie et. al.[5] gave a detailed list of number and type of broken bonds on different orientations of FCC and BCC crystals. They, using the results for number of first nearest neighbor bonds only, calculated[5] surface energy anisotropies for various orientations of FCC and BCC crystals. Their results gave a qualitative

agreement with experimental observations and they suggested that calculations including second and third nearest neighbors' interactions should produce better results.

Recently Sang and Miller[11] extended the calculations on surface energy anisotropies to include second and third nearest neighbor bonds. They used the following equalities for first ϕ_1, second ϕ_2 and third ϕ_3 nearest neighbor bond energies; $\phi_2 = \sigma_2\phi_1$ and $\phi_3 = \sigma_3\phi_1$, where σ_2, σ_3 constants, always less than one, and $\sigma_2 \geq \sigma_3$.

According to Sang and Miller[11] the surface energy of the (hkl) plane is given by:

$$\gamma_{hkl} = (\phi_1 \, a/ \, 2\Omega) \, (A \sin\phi \cos\theta + B \sin\phi + C \cos\phi)$$

where a = lattice constant,

Ω = atomic volume,

ϕ = angle between (100) and (hk0) planes,

θ = angle between (100) and (hkl) planes,

ϕ_1 = energy of first nearest neighbor bond, and

A,B,C = constants, which are a function of σ_2, σ_3 and (hkl) orientation.

The surface energy anisotropies for FCC and BCC crystals can thus be calculated from the above equation assuming certain values of σ_2, σ_3 and without knowing the value of ϕ_1.

Surface energy anisotropy calculations based on the pairwise bonding theory also show that for FCC crystals high index planes, such as (311) and (210), have higher surface energies, γ, than those of the lower index planes, such as (111), (100) and (110), for all the values of σ_2. Only when the second and third neighbor interactions are very strong, i.e.

$\sigma_2 \simeq 1.0$ and $\sigma_3 \simeq 0.9$, γ_{210} is less than γ_{100}. These high values for σ_2 and σ_3, however, are unrealistic. Similar calculations for BCC crystals show that the order (110), (211), (111), (310) and (100) is maintained for increasing surface energy for values of σ_2 up to 0.3 if $\sigma_3 = 0$. The order becomes (110), (211), (100), (310) and (111) for σ_2 between 0.3 and 0.5. On further increasing the value of σ_2, the order changes to (110), (100), (211), (310) and (111). The results on nickel[9] and gold[12] using twin boundary grooving technique gave good agreement with the pairwise bonding theory and are reported in Section II-C-1a.

2. Relation to Equilibrium Shapes and Thermal Facets

a. Equilibrium Shapes. The total surface energy of a body is given by the integral of the form $\int \gamma\,(n)\,ds$ extended over the total surface area, s, of the body, where surface energy, γ, is a function of orientation, (n).[13] From this equation it is seen that the total surface energy will be a minimum when the orientations with lower surface energy occupy an optimum amount of the surface area; the condition for attaining the equilibrium shape of a crystal. Wulff[14] has extended this reasoning to construct the equilibrium shapes of crystals from the orientation dependence of surface free energy. According to him, to arrive at the equilibrium shape, a plane is constructed perpendicular to the radius vector at each point on the three dimensional polar plot of surface energy versus direction. Then the volume which can be reached from the center of this plot without crossing any of the planes is geometrically similar to the ultimate equilibrium shape of the crystal. In the general case the shape consists of some flat areas of low surface energy and some curved regions of higher surface energy. A simple relation for all orientations appearing on

the surface of the equilibrium shaped crystal is given[10] by

$$\gamma_i / h_i = \text{constant},$$

where γ_i is the surface energy for a given orientation and h_i is the perpendicular distance from the center of the crystal to this orientation. In other words, γ_{hkl} is directly proportional to the perpendicular distance from the center of the crystal to the hkl orientation on the surface.

b. Thermal Facets. Thermal faceting studies, the results of which are reported in a later section on previous experimental studies, are essentially based on the above considerations of equilibrium shapes. A review of the subject has been given by Moore.[15] Originally thermal faceting referred to the formation of low energy facets on initially smooth surfaces with an orientation close to that of the low energy plane. At equilibrium a certain fraction of the surface is covered with low energy planes of low Miller indices and the remaining surface with planes of more complex indices, which is necessary to keep the average surface orientation parallel to that of the original surface.[15]

More recently, the term "thermal faceting" has also been used[3,16] to describe the changes in shape due to the 'growth' of low index planes on heated field-ion specimens. At equilibrium the end form, as discussed later, consists primarily of low energy facets (planes), from which the surface energy anisotropy can be found.

3. Gas Adsorption Effect.

The effect of gas adsorption on surface energy, γ, has been

discussed in detail by Shewmon and Robertson.[17] The variation of γ with orientation, in the presence of a solute that is adsorbed at the surface, can be more pronounced than the variation found on clean metal surfaces.

It is often found that the first layer of solute is strongly bound or adsorbed at the surface. Whether or not a solute will adsorb at the interface in a given situation depends on whether or not it decreases the total free energy of the system.[17]

A thermodynamic relationship exists between γ and the number of atoms adsorbed per unit area Γ_2.[18,19] If the solute is slightly soluble in the solvent, the relationship is reduced to the form, expressed by Shewmon and Robertson[17] as

$$\Gamma_2 = -\left(\frac{\partial \gamma}{\partial \mu_2}\right)_T$$

where μ_2 = chemical potential of the solute being adsorbed and is proportional to the logarithm of the solute partial pressure, P_2, i.e., $\partial \mu_2 = RT\ \partial \ln P_2$,

R = gas constant, and

T = absolute temperature.

Both Γ_2 and γ vary with μ_2, and for simplicity it is assumed that the heat of adsorption is the same for all sites at which adsorption occurs. The results on variation of γ with μ_2 have been given by Shewmon and Robertson.[17] If μ_2^o is defined as the value of μ_2 when one half the surface sites are occupied, then when μ_2 is much less than μ_2^o, there is no adsorption and the value of γ is that of a clean

surface, γ_o. When μ_2 is equal to μ_2^o, γ is slightly less than γ_o. When μ_2 is much greater than μ_2^o, Γ_2 is essentially a constant and γ decreases linearly with μ_2.

The linear decrease of γ and constant Γ_2 has been interpreted as follows: When $\mu_2 \gg \mu_2^o$, the mean chemical potential of the adsorbed atoms is μ_2^o; the surface energy of the system equals γ_o minus Γ_2 times $(\mu_2 - \mu_2^o)$. Therefore the energy required to create a new surface in the presence of a gas is the sum of the work required to create a unit area of clean surface and the decrease in free energy due to the solute atoms that leave the vapor phase to adsorb on the newly created surface.

B. Surface Diffusion

The process of an atom migrating over its own surface is defined as surface self diffusion and is the primary topic of this section. It plays a dominant role in establishing the equilibrium shape when a crystal is heated to a temperature close to half its melting point. Surface diffusion has been reviewed by Blakely[20], Neumann and Neumann[21] and recently by Gjostein[18,22] and only a brief review of the process is given in this section.

1. Classification of Surfaces.

Frank[20,23] has suggested a classification of surfaces according to their specific free energies; i.e., singular, vicinal and non-singular. Singular refers to the orientations with low surface energy e.g. (111) in FCC crystals. Vicinal refers to the small range of orientations near a singular surface where the surface energy varies most rapidly. Non-singular surfaces are those with a high step density and for which surface

energy is believed to be highest and practically constant.

Singular surfaces coincide with certain low index orientations of the crystal. The atom positions are essentially the same as the normal lattice positions. At elevated temperatures, some atomic roughening is possible due to the formation of adatom-vacancy pairs; as the thermal vibrations increase in amplitude with temperature, some of the atoms leave their normal sites and adsorb on the surface leaving a vacancy in the original surface. It is of interest to discuss how the atoms migrate on their own lattice and the forces which govern their motion.

2. Theory of Mass Transport

This section is devoted to the formal theory developed by Herring and Mullins[1,4,24-28] for mass transport motivated by changes in surface energy. The transfer of atoms is always in such a direction as to decrease the overall surface energy of the system. Herring has shown that the difference in the chemical potential of an atom, μ, and that of a lattice vacancy, μ_h, immediately beneath a curved surface of principal radii of curvature, R_1 and R_2 is given by

$$(\mu - \mu_h) - \mu_o = \Omega \left\{ \gamma_s (1/R_1 + 1/R_2) + \frac{\partial^2 \gamma_s}{\partial n_1^2} \cdot 1/R_1 + \frac{\partial^2 \gamma_s}{\partial n_2^2} \cdot 1/R_2 \right\}$$

where μ_o = chemical potential of a plane surface,

Ω = atomic volume,

γ_s = surface free energy, and

n_1, n_2 = direction vectors associated with the principal radii of curvature R_1 and R_2, respectively.

In case of a planar surface, for which the diffusion coefficient, D_s, and surface energy, γ_s, do not vary over the range of orientations involved, the above equation becomes as follows:

$$(\mu - \mu_h) - \mu_o = \frac{2\Omega\gamma_s}{R} = \mu'$$

where R = average radius of curvature.

Then the flux of atoms, J_x, migrating in direction x, is given by

$$J_x = -(N D_s/kT)\,\partial\mu'/\partial s$$

where N = number of surface atoms per unit area,

k = Boltzmann constant,

T = absolute temperature, and

s = arc length measured along the profile.

For a given surface the temperature dependence of D_s is expressed by an Arrhenius type relationship:

$$D_s = D_o \exp(-Q_s/kT)$$

where D_o = constant, commonly referred to as a frequency factor, and

Q_s = activation energy for surface diffusion.

Thermodynamically the activation energy, Q_s, is the sum of two contributions, namely the energy involved in creating a vacancy, Q_f, and the energy for its migration through the lattice, Q_m; i.e. $Q_s = Q_f + Q_m$. For a singular surface, Q_f is the energy to create an adsorbed atom leaving a vacancy in the singular plane and Q_m is the energy involved in atom

migration between equilibrium adsorption sites.

Based on the above equations, Blakely[20] derived the following equation for the diffusion coefficient:

$$D_s = a^2 \nu \exp\left(-\frac{\Delta G_f + \Delta G_m}{kT}\right) \quad \text{or}$$

$$D_s = a^2 \nu \exp\left(\frac{\Delta S_f + \Delta S_m}{k}\right) \cdot \exp\left(-\frac{\Delta H_f + \Delta H_m}{kT}\right)$$

where a = mean jump distance between adsorption sites on the surface,

ν = vibrational frequency,

$\Delta G_f, \Delta G_m$ = Gibbs free energies associated with vacancy creation and its migration, respectively,

$\Delta H_f, \Delta S_m$ = corresponding enthalpy changes, i.e., Q_f and Q_m respectively, and

$\Delta S_f, \Delta S_m$ = corresponding entropy changes.

The theory of surface diffusion has been applied[29] to thermal changes on field emitters, in which the surface is nearly hemispherical. The following expression has been derived[29] for the flux migrating from the apex towards the shank of the emitter:

$$J_M = \frac{\gamma \Omega_o^2}{A_o} \cdot \frac{a_M}{r^2 kT} \cdot D_o \exp\left(-Q_s/RT\right)$$

where J_M = volume of material (cm^3/cm sec) passing at a point M on the emitter surface,

γ = surface energy (dynes/cm),

Ω_o = atomic volume (cm^3),

A_o = surface area per atom (cm^2)

r = average radius of curvature at the apex of the emitter (cm),

k = Boltzmann constant,

T = absolute temperature,

D_o = diffusion coefficient at $0^{\circ}K$ (cm^2/sec),

Q_s = activation energy (cal/mole),

R = gas constant ($cal/^{\circ}K$ mole), and

$a_M = 0.625 \sin \theta_M$, θ_M is the angle between apex and point M.

If the flux is expressed as atoms migrating per second, J_A, the following relationship is derived from the above equation, assuming an average distance of atom migration, s, in cm.:

$$J_A = \frac{\gamma \Omega_o}{A_o} \quad \frac{a_M \, s}{r^2 \, kT} \quad D_o \exp(-Q_s/RT).$$

3. Gas Adsorption Effect.

The effect of adsorbed gases and impurities on surface diffusion has been discussed by Neumann and Neumann[21] and Gjostein.[22] A brief summary is given here.

The impurities may diminish or accelerate the rate of surface diffusion, depending upon the system under observation.[21]

a. Diminishing Rate. When sub monolayer impurities adsorb at kink positions along a ledge, pinning of the ledges occurs, and D_s is apparently lowered. This effect is quite important at low temperatures for mass transfer processes in which migration occurs over all orientations. However, at elevated temperatures the adsorbed gases have high surface mobilities and will not serve as pinning points.

When monolayer or multilayer adsorption takes place, and particularly when the first layer is strongly bonded to the surface, diffusion occurs by a surface vacancy mechanism involving a large Q_s, which in effect lowers the diffusion rate. This mechanism was supported by the results obtained from field emission microscopy on tungsten in the presence of water vapor,[30] oxygen and nitrogen.[31]

b. Accelerating Rate. In contrast to the above effect, a high rate of surface diffusion was observed for gold[32] and attributed to adsorbed impurities.The presence of oxygen on copper[33] and silver[34] also increased the rate of surface diffusion. The mechanism[21] involved for accelerating the diffusion rate is that the impurity adsorption lowers the surface energy, which in effect lowers the binding strength or the activation energy, Q_s for surface diffusion.

The bulk impurities may also influence the surface diffusion process, and the techniques using macroscopic changes in surface profiles, e.g.,scratch smoothing, grain boundary grooving, etc., are more susceptible to bulk impurity effects than are the methods using microscopic changes in surface profiles,e.g., field emission and field-ion microscopy.

C. Previous Experimental Studies

A brief account of the results from previous studies on surface energy by several techniques and on surface diffusion primarily by FEM and FIM techniques are given in this section. The limitation on surface diffusion studies is considered appropriate since the "growth rate" of facets on extremely small and highly curved specimens is of primary interest in the present studies.

1. Surface Energy

The absolute values of surface energy of solids are very difficult to determine experimentally. Therefore, the ratio of surface free energy of a given orientation to either that of the closest packed plane, γ_{min}, or that of the orientation with the highest surface energy, γ_{max}, has been generally reported. For convenience the surface energy results have been subdivided below into the following classes:

a. Planar surfaces

b. Small particles

c. Field emitters

a. Planar Surfaces

i) Thermal Faceting

The subject of thermal faceting on planar surfaces has been reviewed by Moore.[15] As stated earlier (see Section II-A-2b), a solid surface facets when heated in a vacuum or in a gaseous environment at elevated temperatures. If the environment is a reactive gas, the process is called thermal etching, which has been reviewed by Shuttleworth.[35]

Ponslet and Bariaux[6] used thermal faceting techniques to determine the surface energy anisotropy of copper single crystals. For copper faceted in a vacuum of 10^{-6} torr at 1000°C, they reported the following results:

$$\text{Copper } 1000^{\circ}\text{C}, \quad \frac{\gamma_{111}}{\gamma_{max}} = 0.845, \quad \frac{\gamma_{100}}{\gamma_{max}} = 0.900 \text{ and } \frac{\gamma_{110}}{\gamma_{max}} = 0.985.$$

Thermal faceting results for tungsten single crystals heated in a vacuum of 10^{-5} to 10^{-6} torr and in a hydrogen atmosphere have been reported by Adam and Wever.[7] They reported the following anisotropy values:

$\frac{\gamma_{110}}{\gamma_{max}}$ = 0.820 and 0.940 in high vacuum and hydrogen, respectively, and

$\frac{\gamma_{112}}{\gamma_{max}}$ = 0.866 both in high vacuum and in hydrogen.

ii) Thermal Grooving

One of the most sensitive techniques for determining the orientation dependence of the surface energy of metals is the study of grooving behavior at the intersections of twin boundaries and grain boundaries with the planar surfaces. The twin boundary technique, which is limited to FCC metals, has been reviewed by Winterbottom and Gjostein.[36]

The surface energy anisotropies of nickel[9] and gold[12], within the stereographic triangle (111)-(100)-(110), were determined at 1000°C and 1030°C, respectively, by twin boundary grooving. Some of the results were as follows:

nickel 1000°C, $\frac{\gamma_{111}}{\gamma_{100}}$ = 1.060, $\frac{\gamma_{110}}{\gamma_{100}}$ = 1.065 and $\frac{\gamma_{max}}{\gamma_{100}}$ = 1.085

gold 1030°C, $\frac{\gamma_{111}}{\gamma_{210}}$ = 0.948, $\frac{\gamma_{100}}{\gamma_{210}}$ = 1.016, $\frac{\gamma_{110}}{\gamma_{210}}$ = 0.993 and

$\frac{\gamma_{max}}{\gamma_{210}}$ = 1.021.

These results were found to be in qualitative agreement with the pairwise bonding theory for surface energy calculations, but the values for σ_2 and σ_3 were not reported.

McLean and his associates[8,37-40] investigated the temperature dependence of surface energy anisotropy of metals using twin boundary and grain boundary grooving techniques. For copper wires annealed in dry hydrogen at 1030°C the following anisotropy values were reported:[8]

Copper 1030°C, $\frac{\gamma_{111}}{\gamma_{100}} = 0.994$, $\frac{\gamma_{110}}{\gamma_{100}} = 1.011$, and $\frac{\gamma_{max}}{\gamma_{100}} = 1.015$

They also reported[37] that the surface energy anisotropy of platinum decreased with increasing temperature. The values for $\gamma_{max}/\gamma_{111}$ for platinum were reported to decrease as follows:

Temperature °C	920	1080	1300	1500
Platinum, $\frac{\gamma_{max}}{\gamma_{111}}$	1.133	1.111	1.104	1.078

The (111) surface of platinum remained atomically smooth up to 1600°C, whereas (100) surfaces were roughened at about 1350°C.

Recently surface energy anisotropy of iron -3% silicon, BCC structure, was reported[39] at various temperatures between 1000°C and 1400°C. The anisotropy values were normalized to γ_{110} and the maximum anisotropy value was reported to vary from 1.07 to 1.10. The relative magnitudes of surface energy of the principal planes varied with temperature as follows:

$\gamma_{111} < \gamma_{110} < \gamma_{100}$ at 1000°C, 1100°C,

$\gamma_{110} < \gamma_{111} < \gamma_{100}$ at 1200°C,

$\gamma_{110} < \gamma_{100} < \gamma_{111}$ at 1300°C, and

$\gamma_{100} < \gamma_{110} < \gamma_{111}$ at 1400°C.

The results up to 1200°C, showing $\gamma_{100} > \gamma_{111}$ and γ_{110}, were explained in terms of a silicon/oxygen complex adsorbate on the (111) and (100) planes; the complex dissociated between 1300°C and 1400°C, giving rise to a decrease in the surface energies of the (111) and (100) planes at 1400°C.

b. Small Particles. A direct method of determining the surface energy anisotropy is to study the equilibrium shape of small particles. Sundquist[41] investigated the equilibrium shape of small metal particles (~1 μdiameter) resting on an inert substrate and equilibriated in vacuum or in a hydrogen atmosphere. The γ plot of the metals was obtained directly from the equilibrium shapes of the particles. The resulting anisotropies of the FCC metals, γ-iron, gold, silver, copper and nickel, were the same as that predicted by the pairwise interaction model of surface energy using a correction for the energy contribution of kinks on surface steps. For α-iron, however, the $\frac{\gamma_{110}}{\gamma_{100}}$ ratio fell in the range of 1.0 - 1.25, whereas the pairwise interaction model predicted this ratio to be 0.874 for $\sigma_2 = 0.5$. Sundquist[41] explained the higher $\frac{\gamma_{111}}{\gamma_{100}}$ observed ratio than the corresponding predicted ratio in terms of preferential adsorption of impurities on (100) surface.

c. Field Emitters. Surface energy anisotropies have also been found by observing the shape of well annealed field emitters. Detailed accounts of the instruments and techniques are given in a number of publications[42-49] and the results of a few of the most pertinent studies are given here. In this technique a small nearly hemispherical single crystal is annealed at a particular temperature in vacuum or in the selected environment. The imaging field is then applied to observe the facets formed during the annealing treatment. There is very little evaporation occurring on the specimen during the time the imaging field is raised from zero to the best imaging field to reveal size of each facet. The primary advantages of studying field emitters are the cleanliness of the surface and the large number of orientations that can be investigated simultaneously. Furthermore, this technique is less susceptible than other techniques to bulk impurity effects.

Drechsler and Nicholas[10] have reported the equilibrium shapes and surface energy anisotropies for a number of metals using field emission microscopy. The specimens were annealed in ultra high vacuum, and the equilibrium shapes consisted of flat areas surrounded by curved regions. The maximum surface energy anisotropies, λ_{max}, for a number of refractory metals (W, Mo, Ta, V, Nb, Ir, Pt, Rh) as well as for α-iron and nickel were found to be in the range of 1.02-1.10. These results are summarized in Section II-A-1a. The values were reported to be in quantitative agreement with anisotropy calculations using a Mie potential.

Brenner[3] reported that on heating in vacuum at 990°C or below field evaporated iridium surfaces developed (111), (100) and (210) facets. The development of (111) and (100) facets was in agreement

with the broken bond model of surfaces, but the formation of (210) facets was not. From the size of (111) facets formed on iridium at 990°C, Brenner estimated the surface energy anisotropy $\gamma_{111}/\gamma_{max}$ to be nearly equal to 0.96. The surface energy anisotropy for (100) and (210) facets were not calculated. Brenner also investigated the faceting in several gaseous environments at 700°C and found that impurities changed the nature of faceting. In an oxygen atmosphere, (210) facets were eliminated, and (110) and (113) facets appeared; whereas in carbon monoxide, hydrogen and nitrogen, at pressures up to 0.1 torr, there were only minor effects, i.e., the vacuum configuration was essentially maintained. However, in a mixture of 25% carbon monoxide and 75% oxygen a mixed surface configuration appeared showing (111), (100), (110), (311) and (210) facets.

Recently Müller and Drechsler[50] used field-ion microscopy to determine the surface free energy anisotropy of tungsten along [111], [100] and [110] zones. The specimens, annealed in ultra high vacuum at 2580°K, were assumed to have the equilibrium shape. The shape of the crystal was determined from the field-ion images using correction terms to account for local variation in magnification and the top ring contraction effect. The following equation was given for the true facet size:[50]

$$\theta_{hkl} = \theta^{ob}_{hkl} \cdot M_o/M_r \cdot M_o/M_k$$

where θ_{hkl} = corrected facet size of hkl plane, in degrees,

θ^{ob}_{hkl} = measured facet size of hkl plane, in degrees,

M_o/M_r = magnification correction term, and

M_o/M_k = top ring contraction term.

Müller and Drechsler[50] also discussed how to calculate the correction terms from FIM images, and a brief description is given below:

i) Magnification Term.

The magnification depends on the local radius of curvature and the correction term, M_o/M_r, equals $(r_o/r)^{2/3}$; where r is the local radius of curvature and r_o is the average tip radius. The magnification term can also be determined from the "best image" voltage of each surface region.

ii) Top Ring Contraction Term.

An indirect approach is taken to determine the contraction term. On a partially field evaporated facet, the number of plane rings, n, between the faceted plane (hkl) and a nearby plane (h'k'l'), ϕ degrees apart, are counted. Then the true facet size, in degrees, is given by:

$$\Theta_{hkl} = 2 \sin^{-1} \frac{d}{2r}$$

where $d = 2\sqrt{2rb - b^2}$ and

$b = r(1 - \cos\phi) - n\,a$

The top ring contraction term is then given by:

$$M_o/M_k = (\Theta_{hkl}/\Theta^{ob}_{hkl})/(M_o/M_r)_{hkl}$$

where Θ_{hkl} = true facet size, in degrees, of hkl plane,

r = local radius of curvature, in Å, of (hkl) region,

ϕ = angular separation of (hkl) and (h'k'l'), in degrees,

n = number of plane rings between (hkl) and (h'k'l'),

a = (hkl) interplanar distance, in Å,

Θ^{ob}_{hkl} = observed facet size, in degrees, on a partially field evaporated image, and

$(M_o/M_r)_{hkl}$ = magnification term for (hkl) region.

The results of Müller and Drechsler[50] on surface energy anisotropy of tungsten at 2580°K in vacuum were in quantitative agreement with the calculated anisotropy using a Mie potential with m=5,n=7 and + 1.5% lattice change. Only qualitative agreement was found with calculations using the Morse potential or the pairwise bonding theory. They also reported the effect of carbon adsorption at 1700°K on the annealed end form, which revealed large (110), (100) facets along with (334) facets. No quantitative analysis was given to ascertain the effect of adsorption on surface energy of tungsten.

2. Surface Diffusion

Mullins[51] has calculated the rate of increase of width of an isolated low index facet, assuming various mechanisms of growth. The facet was assumed to have already grown to a finite size, with a contact angle Θ to the original surface. According to him the following rates of growth of the facet under different mechanisms were found:

$d \propto t^{1/2}$ for evaporation and condensation,

$d \propto t^{1/3}$ for volume diffusion,

$d \propto t^{1/4}$ for surface diffusion

where d is the facet width and t is growth time. Robertson[52] has measured the time exponent, n, of growth laws for several facets formed on copper in H_2O/H_2 mixtures. In cases where the facets were very narrow, n was about 1/4, which suggested that the surface diffusion mechanism was important for small facets.

The changes in surface profiles that occurred on field emitters at elevated temperatures were in the range of 0.1 - 1μ and Boling and Dolan[2], from the field emitter shapes, observed by electron microscopy, established that surface diffusion was the dominant mechanism.

a. Field Emission Microscopy (FEM) Studies. Field emission microscopy has been used extensively for surface self diffusion studies. The experiments are carried out in ultra high vacuum on clean surfaces and the surface migration covers a wide range of orientations. The research by FEM has been limited primarily to refractory metals, because they could be flash cleaned easily without appreciable blunting.[29,30] There are three methods utilizing FEM to study surface diffusion. These methods are briefly described below, and the principal results from studies using these methods are summarized in Table 1.

i) Ring Rate Decay Method

In this method the rate of change of emitter length at a fixed temperature is found by pulsed field emission microscopy[29,54] and used to calculate D_o and Q_s, the diffusivity constant at 0^oK and the activation energy for surface migration, respectively.

ii) Build Up and Protrusion Decay Methods

In FEM the tendency of the emitter to increase in radius can be counteracted by the application of a large dc field. As a result,

Table 1. Surface Diffusion Studies by Field Emission Microscopy

1. Ring Rate Decay				2. Build-up and Protrusion Decay				
Metal	Q_s K Cal/mole	D_o cm^2/sec	Ref.	Metal	Q_s K Cal/mole BU	BU(Zero)	PD	Ref.
W(110)	72.0	4.0	29	W	56.3	65.3	-	53
W(110)	68.0	0.50	54	W	54.4	-	73.8	55
W(100)	62.3	0.30	54	W	-	-	72.0	58
Re(10$\bar{1}$0)	53.0	0.90	54	Mo	46.2	66.0	48.4	57
Re(0001)	48.4	-	54	Pt	19.1	20.6	29.5	59
Ir(111)	53.0	-	54	Ni	26.3	29.7	21.4	59
Rh(111)	41.5	0.04	54					

3. Condensate Spreading

Metal	Q_s K Cal/mole	Ref.
W (100)	45.0	30
W (110)	76-84	30
W (110)	37-46	60
W (112-111)	42-51	60
W (123-122)	42-51	60
W (112-113)	65-74	60
W (123-012)	69-79	60
W (001-012)	83-92	60
W (001-113)	83-92	60
W (013-113)	88-101	60
Re(10$\bar{1}$0)	36.0	61
Re(10$\bar{1}$1)	20.0	61
Re(11$\bar{2}$2)	26.0	61

the initial rounded geometry forms low index facets and the tip assumes a polyhedral shape. This process is called build up (BU) and has been investigated by Bettler and Charbonnier[53] and Sokolovskaia.[55,56] At high temperature in the absence of the field the build up form reduces to the rounded shape of the emitter and this process is called protrusion decay (PD). In some cases the calculations were done for zero field on the emitter in case of build up technique.

iii) Condensate Spreading Method

In this technique the rearrangement and spreading of atoms, deposited onto the tip from a nearby filament, are observed. Müller[30] and Drechsler and Vanselow[60] investigated surface diffusion of tungsten, whereas Maiwald and Stark[61] studied the migration of rhenium atoms.

b. Field-Ion Microscopy (FIM) Studies. The field-ion microscope not only allows one to locate individual atoms, but also provides smooth and perfect surfaces, which are essential for diffusion studies. Some of the results obtained by FIM are given in Table 2. A brief account of the methods used is given below.

In adatom migration studies,[62] in which atoms were deposited on a clean specimen and changes in the position of atoms after heating for various times were recorded, Ehrlich and Hudda[62] derived the diffusion parameters using the following relationship based on the random walk theory:[63]

$$\langle r^2 \rangle = N l^2 = 2 D_s \tau \quad \text{and} \quad N = \nu\tau$$

where $\langle r^2 \rangle$ = mean square displacement,

N = number of jumps,

Table 2. Surface Diffusion Studies by Field-ion Microscopy

Metal	Q_s K Cal/ mole	D_o cm^2/sec	Ref.
W (110)	22.0	$3X10^{-2}$	62
W (321)	20.0	$1X10^{-3}$	62
W (211)	13.0	$2X10^{-7}$	62
Ir (111)	45.0	-	3
W (011-112-233)	41.5	-	16
W (112-233-111)	48.4	-	16
W (011-112-113)	50.7	-	16
W (013-112-001)	53.0	-	16

l^2 = average of the square of the individual distances spanned by the N atomic jumps,

D_s = diffusion coefficient,

ν = jump frequency per second, and

τ = time interval.

From the D_s values for (110), (321) and (211) planes at various temperatures the diffusion parameters, D_o and Q_s were determined and the results are given in Table 2.

Brenner[3] used FIM to study the growth of (111) facets on iridium. The change in size of (111) facets was found to follow $t^{1/3}$ law, where t is the time of annealing. When the data was analyzed for facet size versus time, it was found that the facet size was proportional to $t^{1/5}$. From the change in (111) facet size at various temperatures, Brenner calculated an activation energy of 45 k cal/mole for (111) facet growth. This value was about 0.3 times the heat of vaporization, and he concluded that the rate controlling step for faceting was the removal of atoms from kink sites.

The rearrangement of field evaporated tungsten surfaces at elevated temperatures has been investigated by Basset.[16] The tungsten surfaces, flash cleaned and field evaporated, were heated in helium at a pressure of 10^{-3} torr, and the displacements of atoms from one site to another were recorded. From the displacement rate at a particular temperature and the number of kink sites in that region, the activation energies were calculated. Some of the results of the investigation are given in Table 2. Another feature, observed on heating tungsten specimens, was the development of surface steps more than one atom layer high around the low index planes.

CHAPTER III

APPARATUS AND EXPERIMENTAL TECHNIQUES

A. Field-Ion Microscope

A conventional stainless steel system was used in these studies. A schematic diagram of the system is given in Figure 1.

1. Vacuum System

The vacuum system was equipped with a diffusion pump, backed by a mechanical pump, which was used for initially evacuating the system and for pumping imaging gas during microscopy. The system was also equipped with an ion pump and a titanium sublimation pump which allowed pressures of less than 10^{-9} torr to be attained. Hastings vacuum gauge and a Varian nude ionization gauge were used for pressure measurements in the system.

After bakeout at 180°C for 10 hours, the pressure was generally in the 10^{-9} torr range. Further cooling the microscope body to the appropriate cryogenic temperatures used in the experiments reduced the pressure to about $1X10^{-9}$ torr.

2. Specimen Holder

The specimen was spot welded to a tungsten loop made of 0.005" diameter wire. Tantalum leads of 0.005" diameter wire were also spot welded to the loop on either side of the specimen. A typical specimen assembly is shown in Figure 2. The spiral ends of the tungsten loop and tantalum leads, Figure 3, were then attached to four pins provided

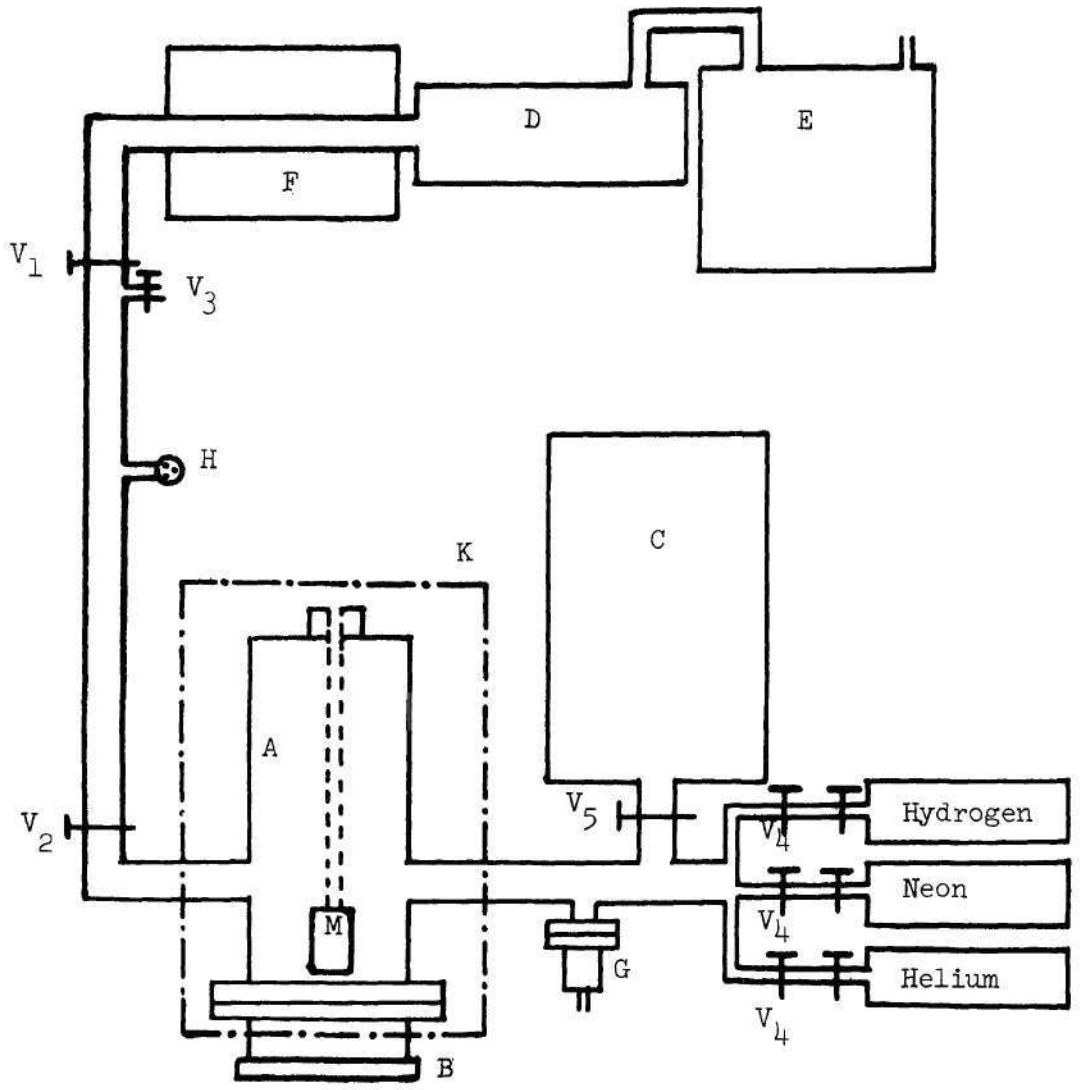

A. Microscope Body

B. Fluorescent Screen

C. Titanium Sublimation and Ion Pump

D. Diffusion Pump

E. Mechanical Pump

F. Liquid Nitrogen Trap

G. Varian Nude Ionization Gauge

H. Hastings Vacuum Gauge

K. Baking Assembly

M. Specimen Holder

V_1. Polyamide High Vacuum Valve

V_2, V_5. UHV Bakable Leak Valves

V_3. Air Admittance Valve

V_4. Variable Leak Valves

Figure 1. Schematic Diagram of the Field-ion Microscope.

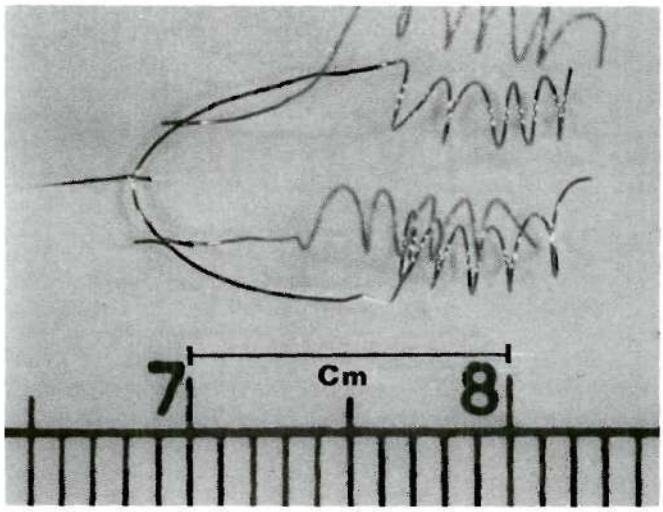

Figure 2. A Typical Specimen Assembly.

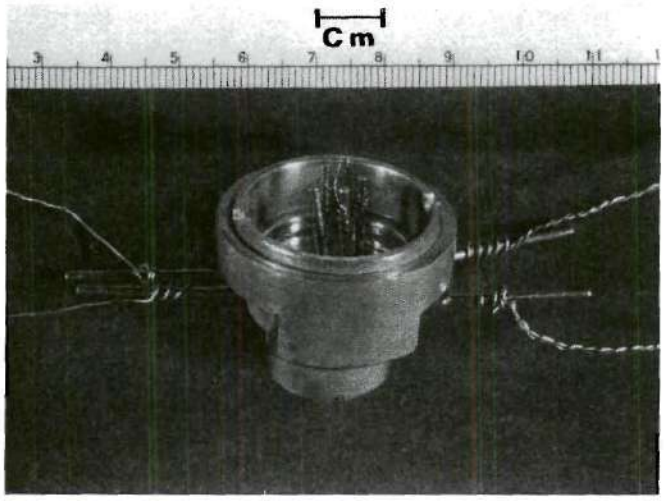

Figure 3. Specimen Holder.

in the specimen holder. These pins were electrically isolated from the rest of the microscope by saphire discs. The two pins attached to the tungsten spirals were connected to a high voltage feed-through, using thick (0.040" diameter) platinum wires. These leads were used for resistance heating and for applying the positive potential during microscopy. The other two pins, which were connected to the tantalum spirals, were connected to another high voltage feed-through, using thin (0.020" diameter) platinum wires. These leads were used to measure the potential drop across the loop, which was used to determine the specimen temperature.

3. Electrical Circuit and Temperature Measurements

The circuit diagram for heating the specimens is shown in Figure 4. It was designed to supply constant dc current which could be regulated either with the input voltage or with the 10 turn helipot of 4.9 K Ω resistance. The current in the circuit was obtained by measuring,with a Honeywell Digitex model 333, the potential drop, in millivolts, across a precision 0.1 Ω resistor of 10 watt capacity. The high wattage of this resistor ensured the stability of its resistance within 1% even when high currents of approximately 3 amperes were used.

The temperature-resistivity relations for tungsten are known (Appendix A). Therefore,measurement of the resistivity of the tungsten loop allows the temperature of the loop to be found. The resistivity is equal to the resistance multiplied by a constant 'A' which depends upon only the dimensions (length and cross-sectional area) of the wire. If the resistance is measured at a known temperature, this constant 'A' can be found. In the present experiments this was done at room temperature after mounting the specimen and evacuating the microscope. The potential

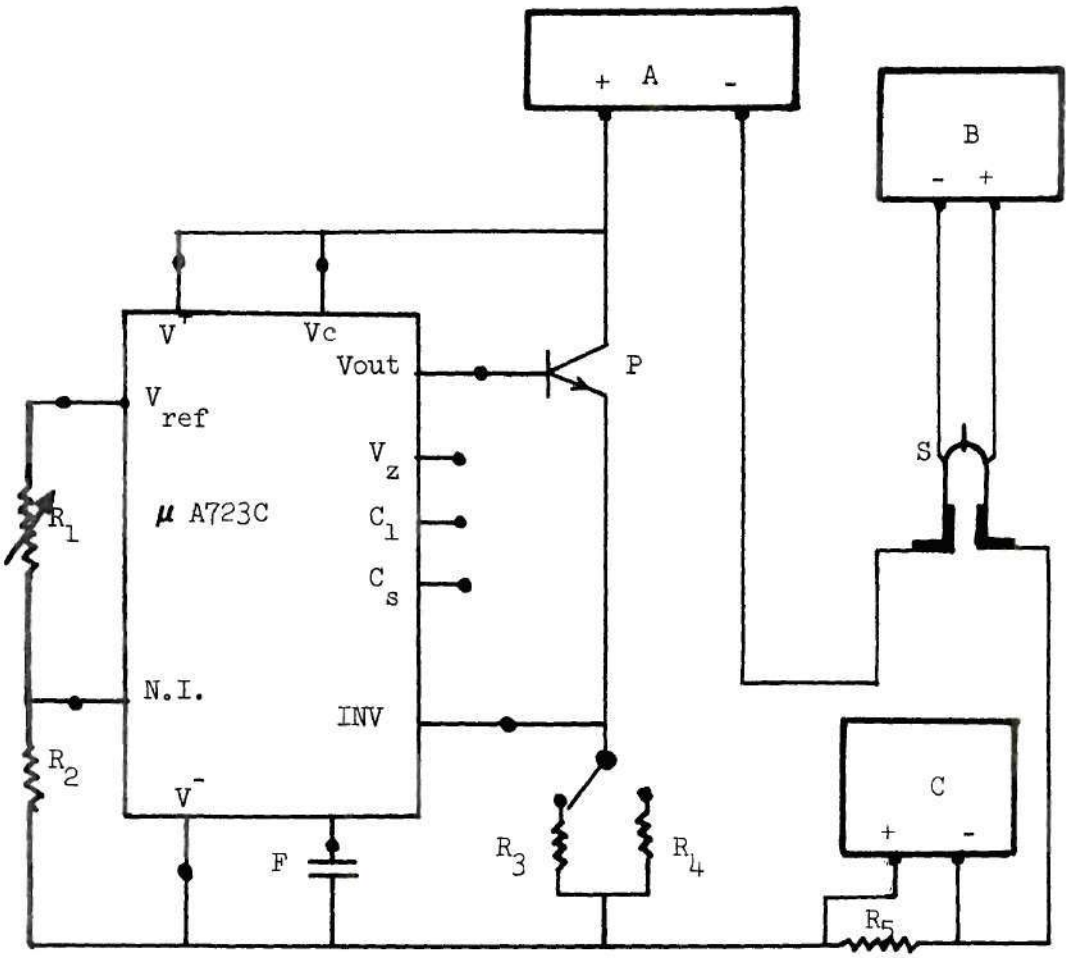

A. Hewlett Packard Supply Model 6284A (0-24 V, 0-4 Amp.)

B. Keithley Electrometer Model 610C

C. Honeywell Digitex Model 333

F. Capacitor (5 nF)

P. Power Transistor NPN Type (2N 6044)

S. Specimen Loop

μA723C Voltage Regulator by Fairchild

R_1 Helipot 10 turns (4.9 KΩ)

R_2 Resistor (3KΩ)

R_3 Precision Resistor (6Ω, 25 W)

R_4 Precision Resistor (2.2Ω, 25W)

R_5 Precision Resistor (0.1Ω, 10W)

Figure 4. Constant Current Circuit Diagram for Specimen Temperature Control and Measurement.

drop across a portion of the tungsten heating loop was measured with either a Keithley Electrometer model 610C or a Honeywell Potentiometer model 2705. The resistance of the heating loop was then calculated using this voltage and the known constant current. The specimen temperature during the thermal faceting experiments could be found by simply measuring the resistance, multiplying by 'A' and interpolating from the known resistivity-temperature relations (Appendix A).

The loop temperature measurements were within $\pm$ 5°K, found from the fluctuations in the millivolt drop across the loop. The corrections were not made for the temperature drop along the shank of the specimen because the specimen lengths were approximately 3 mm or less and the specimen temperatures were not high enough to cause an appreciable radiation loss. The radiation losses, which cause a temperature gradient along the shank, depend[64] upon the loop temperature and the thermal conductivity of the specimen. It has been estimated[64] that the temperature drop along the shank is negligible for specimens of 2-3 mm length when the loop temperature is less than 1400°K.

4. Other Features

The microscope body was so designed that the specimen could be cooled to liquid nitrogen or liquid helium gas temperatures, liquid nitrogen could be poured directly into the specimen holder dewar, while temperatures below 50°K could be obtained by regulating[65] the flow of cold helium gas from a liquid reservoir through an insulated transfer tube to the specimen holder dewar.

Research grade gases, helium and hydrogen were used to image the specimens. The appropriate gas was admitted to the system through a

variable leak valve.

A phosphor coated fibre optic screen was used to view the image and contact photography with 4 in. X 5 in. Tri-X-Pan film was used to record the images.

B. Experimental Procedure

1. Preparing the Specimen

a. Materials and Polishing Technique. The materials used in this research were VP or MARZ grade wires of 0.005" diameter obtained from Materials Research Corporation. Typical compositional analyses, supplied with the wires are given in Table 3. All of the wires were originally in the cold worked condition, but were vacuum annealed for 15-30 minutes at about half the melting point prior to preparing field-ion specimens. For preparing the specimens the wire was spot welded to a tungsten loop and electropolished to a fine tip having a radius of curvature within 400-1000 $\mathring{A}$. The polishing solutions and the conditions are given in Table 4.

b. Microscope Mounting and In-situ Preparation. After electropolishing the specimen was mounted in the field-ion microscope and the electrical connections were made as described in Section III-A-3. The system was sealed and evacuated to approximately 10^{-5} torr with the mechanical and diffusion pumps and then to the 10^{-8} torr range with the titanium sublimation and ion pumps. The system was baked at 180°C for 10-12 hours and a pressure in the range of 10^{-9} torr was obtained on cooling to room temperature. After measuring the room temperature resistance of the loop, the specimen was cooled to approximately 78°K with

Table 3. Typical Analyses of Materials

Impurity Contents in ppm by Weight	Iridium VP Grade	Tungsten VP Grade	Iron MARZ Grade	Platinum VP Grade
C	10	20	8	-
H	10	5	< 0.1	-
O	5	25	7.2	-
N	20	10	7	-
Ag	< 5	< 10	< 0.04	10
Al	10	15	-	10
Bi	-	-	< 0.008	-
Ca	10	< 5	2	< 1
Cd	-	-	< 0.08	-
Co	-	< 10	0.3	-
Cr	-	< 15	0.6	15
Cu	20	< 15	< 0.02	< 1
Fe	25	< 15	Rest	50
Hf	-	-	< 0.025	-
K	-	-	0.2	-
Mg	-	< 5	8	< 1
Mn	-	< 5	0.1	-
Mo	-	50	0.2	-
Na	10	-	0.08	-

Table 3. (Continued)

Impurity Contents in ppm by Weight	Iridium VP Grade	Tungsten VP Grade	Iron MARZ Grade	Platinum VP Grade
Nb	-	-	0.03	5
Ni	10	< 15	1.2	5
Pb	-	< 10	< 0.015	-
Pd	20	-	< 0.08	5
Pt	50	-	< 0.025	Rest
Rh	100	-	< 0.03	15
S	-	-	1.2	-
Si	20	< 10	0.5	10
Sn	-	< 10	< 0.02	-
Ta	-	-	< 1	-
Ti	-	< 10	0.5	5
V	-	-	< 0.1	-
W	-	Rest	< 0.1	-
Zn	-	15	< 0.8	-
Zr	-	-	< 0.06	5

Table 4. Specimen Polishing Solutions and Conditions

Metal	Polishing Solution	Conditions
Iridium	30% Chromic Acid	dc; 10 - 3 V
	Sat. $(NH_4)_2 CO_3$	Back polished dc; 4 V, 3-5 sec.
Tungsten	10% KOH	dc; 30-4 V
Iron	25 gms. Chromic Oxide 133 mls. Glacial Acetic Acid 7 mls. Distilled Water	dc; 22-3 V
Platinum	20% KCN	ac; 15 - 3 V

liquid nitrogen. The pressure in the system was then 10^{-9} torr or less.

The imaging gas, helium or hydrogen, was admitted to the system at a pressure of approximately 10^{-4} torr and a positive potential was slowly applied to the specimen. The image was viewed on a slanting mirror placed below the fibre optic screen. After developing the image by field evaporation to cover approximately 75% of the screen, the voltage was cut off, and the specimen was either flash cleaned in vacuum or helium (Ir, W, Pt) or chemically cleaned in hydrogen (Fe). The specimen was then reimaged, and if evidence of contamination was present in the image, the cleaning process was repeated until no contamination was indicated in the image. The specimens were then field evaporated to an approximately hemispherical end form prior to thermal faceting studies. An effort was made to stop the evaporation process just as a plane was removed and prior to additional evaporation of the next plane.

2. Annealing the Specimen

a. In Vacuum. After obtaining an image of the field evaporated end form, the voltage and the image gas supply were cut off, and the system was evacuated with the ion pump to a pressure of approximately 10^{-9} torr. The heating and the potential measuring leads were connected to the appropriate terminals and the specimen was heated at a measured temperature for a selected period of time.

After the heat treatment the specimen was reimaged and photographed. A series of photographs, taken as the image voltage was varied in increments, was often necessary to reveal the top most plane ring for each facet. The specimen was then field evaporated to the original end form and another heat treatment was performed.

b. In Hydrogen. For annealing in hydrogen a procedure similar to that given above for vacuum annealing was used. The hydrogen pressure in the system was selected to ensure at least monolayer coverage (Appendix B) on the specimen. After annealing in hydrogen the specimen was reimaged and photographed.

C. Analytical Procedure

1. Field-ion Results

a. Surface Energy Anisotropy. The true angular width of facets was obtained by multiplying the observed angular widths by the appropriate correction terms. These terms are described in Section II-C-1c.

The following relationship derived[10] from the Wulff's theorem was used to calculate the surface energy anisotropy, λ_{hkl}, from the true angular widths:

$$\lambda_{hkl} = \frac{\cos \frac{\theta_{hkl}}{2}}{\cos \frac{\theta_{max}}{2}}$$

where θ_{hkl} = true angular width of (hkl) facet, and

θ_{max} = true angular width of the lowest energy facet, i.e., (111) in FCC and (110) in BCC.

b. Facet Growth Rate. A series of micrographs were taken after annealing at a fixed temperature for increasing periods of time. On each micrograph the average diameter, in mm, of the projected facet size was measured. The facet sizes were then converted to the corresponding values in angstroms using the following relations:

for iridium (111) facet; 1 mm = $(16.2\ n_{111\text{-}221})/(d_{111\text{-}221})$ Å, and

for tungsten (110) facet; 1 mm = $(18.53\ n_{110\text{-}431})/(d_{110\text{-}431})$ Å

where $n_{hkl\text{-}h'k'l'}$ and $d_{hkl\text{-}h'k'l'}$ are the number of plane rings and the distance, in mm, on the field evaporated micrograph taken before the annealing treatment, between hkl and h'k'l' poles.

2. Facet Growth Model.

a. Mathematical Model. In this section a model for growth of an isolated facet on a field emitter is described; this model forms the basis of computer calculations given in the next section.

The model is essentially a diffusion model, in which all of the atoms of the top most plane at a constant elevated temperature are detached and migrate to the underlying planes. It should be noted that during the removal of this plane, atoms are also detaching and migrating from the underlying planes. However, this model deals with the net attachment, that is the fraction attached minus the fraction detached. Figure 5 shows a schematic diagram of a field emitter of radius R. The closest packed planes, which are usually projected in the center of the image are depicted at the apex, and are the ones for which the facet growth rate is considered in this model.

During a particular time period, depending upon the number of atoms in the first plane, all the atoms in this plane migrate to the underlying planes. The new facet size will be given by the original size of the second plane plus any change in this size due to the net

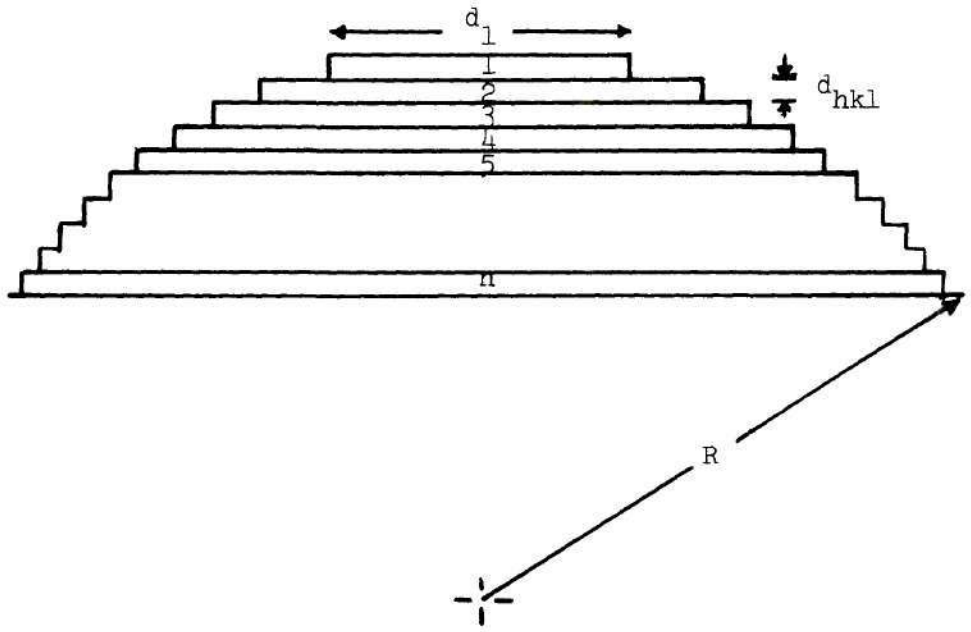

d_1 = Diameter of the First Plane

d_{hkl} = Interplaner Spacing

R = Specimen Radius

Figure 5. Schematic Diagram of a Field-ion Specimen.

attachment of atoms from the first plane. If annealing is continued the second plane atoms would then migrate in a similar fashion to the underlying planes revealing a new facet size equal to the original size of the third plane plus any change in size due to a net attachment of atoms from the first and second planes. The time required for the removal of the top two planes according to the diffusion process is proportional to the number of atoms in the first plane plus the number of atoms in the second plane plus the net number of atoms attached to the second plane from the first plane. This faceting process continues in this fashion until the facet attains the equilibrium size.

In order to use this model to determine the facet growth rates, the net fraction of available atoms attached to each of the underlying planes during the removal of each plane, should be known. Another approach is to calculate the growth rate for a number of values of this fraction and then compare these results with those obtained experimentally to determine this fraction. The latter approach is used here.

While the above model can be used with different values of the fraction of available atoms for each plane, it is reasonable to assume, as a first approximation, that this fraction, X_F, is the same for each plane for the following reasons. Both the number of atoms attached to and the number of atoms detached from a plane are proportional to the number of atoms on the net plane edge. This number increases in going from the first plane to the n^{th} plane. Since increased gain of atoms by a given plane due to the increased number of ledge sites is partially compensated for by the increased loss of atoms by that plane for the same reason, then it may be assumed that the net fraction of

available atoms attached is a more slowly varying function of the plane number than the absolute values of atoms gained or lost.

A mathematical form of the model is presented below:

Let $A_1, A_2, A_3, \ldots, A_n$ represent the number of atoms on the planes 1,2,3,....n, respectively, of a hemispherical specimen as shown in Figure 5. At time $t_1 = 0$ the facet size $d_1 = K_f \sqrt{A_1}$, where K_f is a constant. The values of K_f for iridium (111) and tungsten (110) are calculated to be 2.85 and 3.03, respectively. As all the atoms of the first plane migrate, in time $t_2 = K_t A_1$*, the net fraction of these atoms attached to the underlying planes decreases because the number of available atoms keeps on decreasing for subsequent planes. The net change in the number of atoms of each plane is represented as follows:

$$A_1 \rightarrow 0$$

$$A_2 \rightarrow A_2 + X_F A_1 = A_2'$$

$$A_3 \rightarrow A_3 + X_F (1 - X_F) A_1 = A_3'$$

$$\ldots\ldots\ldots\ldots\ldots\ldots\ldots\ldots$$

$$\ldots\ldots\ldots\ldots\ldots\ldots\ldots\ldots$$

$$A_n \rightarrow A_n + X_F (1 - X_F)^{n-2} A_1 = A_n'$$

The new facet size d_2 revealed after t_2 is equal to $K_f \sqrt{A_2'}$. If annealing is continued then after time $t_3 = K_t(A_1 + A_2')$ the net change in each plane atoms would be as follows:

---

*K_t is a constant, dependent upon the temperature of annealing and the activation energy for surface migration on field emitters (see Section II-B-2).

$$A_2' \rightarrow 0$$

$$A_3' \rightarrow A_3' + X_F A_2' = A_3''$$

$$A_4' \rightarrow A_4' + X_F (1 - X_F) A_2' = A_4''$$

.....

.....

$$A_n' \rightarrow A_n' + X_F (1 - X_F)^{n-3} A_2' = A_n''$$

The facet size d_3 now revealed after t_3 is equal to $K_f \sqrt{A_3''}$. The faceting process continues in this fashion till the facet attains the equilibrium size.

The facet size, d_i, is plotted against time, t_i, to determine the growth rate, for i = 1, 2, 3, ..., n. A similar plot of $d_i - d_1$ versus t_i gives the growth rate for change in facet size.

b. Computer Programs

i) General

A computer program was developed to calculate the facet size as a function of time, assuming a systematic migration and removing one plane at a time as described in the above model. The parameter X_F was varied from 0 to 0.5 in steps of 0.05, and the specimen radius, R was varied from 600 to 1300 Å in steps of 100 Å. This program, which is given in Appendix C, was in a combined form for faceting on iridium (111) and tungsten (110) planes. In these computer calculations all the characters with A refer to iridium and with B to tungsten. All other characters are common to both metals. The total number of planes systematically migrated are NP, (NP = n).

In the computer program the square of the diameter of each plane, d_1, d_2, d_3, ... d_n was calculated first, using the following relationship:

$$d_1^2 = 4\,[R^2 - (R - 3\,d_{hkl}/4)^2\,] = 4[R^2 - (R + d_{hkl}/4 - d_{hkl})^2\,]$$

$$d_2^2 = 4\,[R^2 - (R + d_{hkl}/4 - 2.\,d_{hkl})^2\,]$$

$$\cdots\cdots\cdots\cdots\cdots\cdots\cdots$$

$$d_n^2 = 4\,[R^2 - (R + d_{hkl}/4 - n.\,d_{hkl})^2\,]$$

where R is the specimen radius, and d_{hkl} is the interplanar spacings of{hkl}planes. The surface area of each plane was then calculated and number of atoms on each plane found from the surface area and the atomic density of the plane. After calculating the number of atoms in each of the n planes, systematic migration was performed according to the proposed model.

Typical computer results for growth parameters of iridium (111) and tungsten (110) facets are given in Appendices C-1 and C-2, respectively, for R = 800 Å and X_F = 0.10. The first column in these printouts gives the total number of atoms migrated, i.e., t_i/K_t after (i-1) planes have migrated systematically. The second column gives corresponding square root values of the number of atoms on the top plane, $\sqrt{A_i^{i-1}}$, which is equal to d_i/K_f. The third column gives the corresponding change in the square root values of the number of atoms on the top plane, $\sqrt{A_i^{i-1}} - \sqrt{A_1}$, which is equal to $(d_i - d_1) / K_f$. All these terms are explained under the general model. The last three columns give in corresponding order the logarithm of the values in the

first three columns.

ii) Calcomp Plotter

The calcomp plotter programs were coupled with the general program to plot facet size, d_i, or change in facet size, $d_i - d_1$, versus time, t_i, on a log - log scale for i = 1, 2, 3, ..., n. A program for plotting the growth of tungsten (110) facet size for various values of X_F is given in Appendix D (R = 800 $\mathring{A}$). A similar program was designed to plot facet size or change in facet size versus time for various specimen radii with a fixed value of X_F.

In general, the plotting starts from the second set of data, i.e., t_2, d_2 or $d_2 - d_1$, and continues up to the n^{th} data set, n is the total number of planes migrated systematically.

CHAPTER IV

RESULTS

The results are presented separately for each metal and are further divided into two or three sections, depending upon the metal.

Thermally Faceted End Forms

In this section typical field-ion micrographs of specimens before and after various annealing treatments are presented. The general features of the images along with other pertinent observations during the experiments are also given. References to facet sizes in this section are qualitative and based on the apparent sizes observed on the micrographs.

Surface Energy Anisotropy

In this section analytical results from the field evaporated and thermally annealed end forms are presented. True facet sizes are obtained and used to calculate the surface energy anisotropies.

Kinetics of Faceting

Measured growth rates for iridium (111) and tungsten (110) regions are presented as a third section of results in the case of these two metals. From the growth of these facets the activation energy for faceting is also calculated. The results of the corresponding model growth rates for faceting are also presented.

A. Iridium

1. Thermally Faceted End Forms

Helium gas and a specimen temperature of 78°K were used for both field evaporation and imaging of all iridium specimens. Prior to thermal faceting experiments, iridium specimens were cleaned by flash heating at approximately 2000°K and then field evaporating to a nearly hemispherical end form. A typical field-ion micrograph of an iridium specimen prepared in this way is shown in Figure 6.

Typical micrographs of iridium after various heat treatments are shown in Figures 7-9. The important features of these micrographs and other pertinent observations are given below according to the environment and temperature range for annealing.

a. In Vacuum. Iridium specimens annealed below 880°K did not show any faceting; however, some rearrangement of the specimen surface was observed from the field-ion micrographs taken before and after such treatments. Other iridium specimens which did reveal faceting had been annealed in vacuum at the following absolute temperatures (time, in minutes): 880(10), 890(32), 1125(6,20,33),1130(30,65),1142(2),1170(3, 10,21),1300(16), and 1360(16,32) or in helium at 10^{-4} torr as follows: 760(10), 790(4), 860(10),1050(5),1090(3),1160(8), 1733(4,10). No significant differences were expected or found between specimens annealed in helium and those annealed in vacuum, and the results are therefore considered to be representative of vacuum annealing in both cases.

For specimens annealed between approximately 880 and 1170°K, the order of decreasing facet size was different from that of specimens

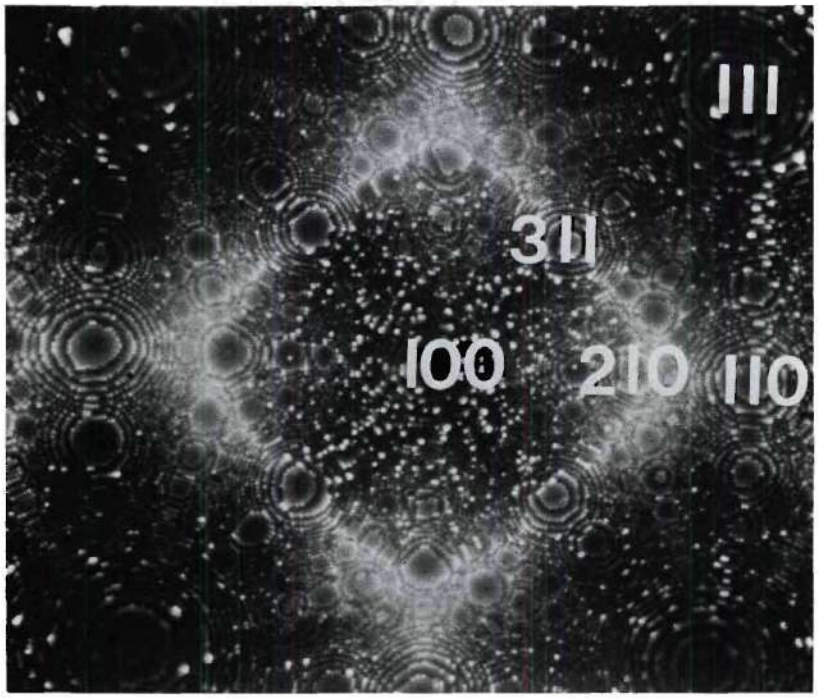

Figure 6. A Typical Field-Evaporated Iridium Specimen - 18.0 KV.

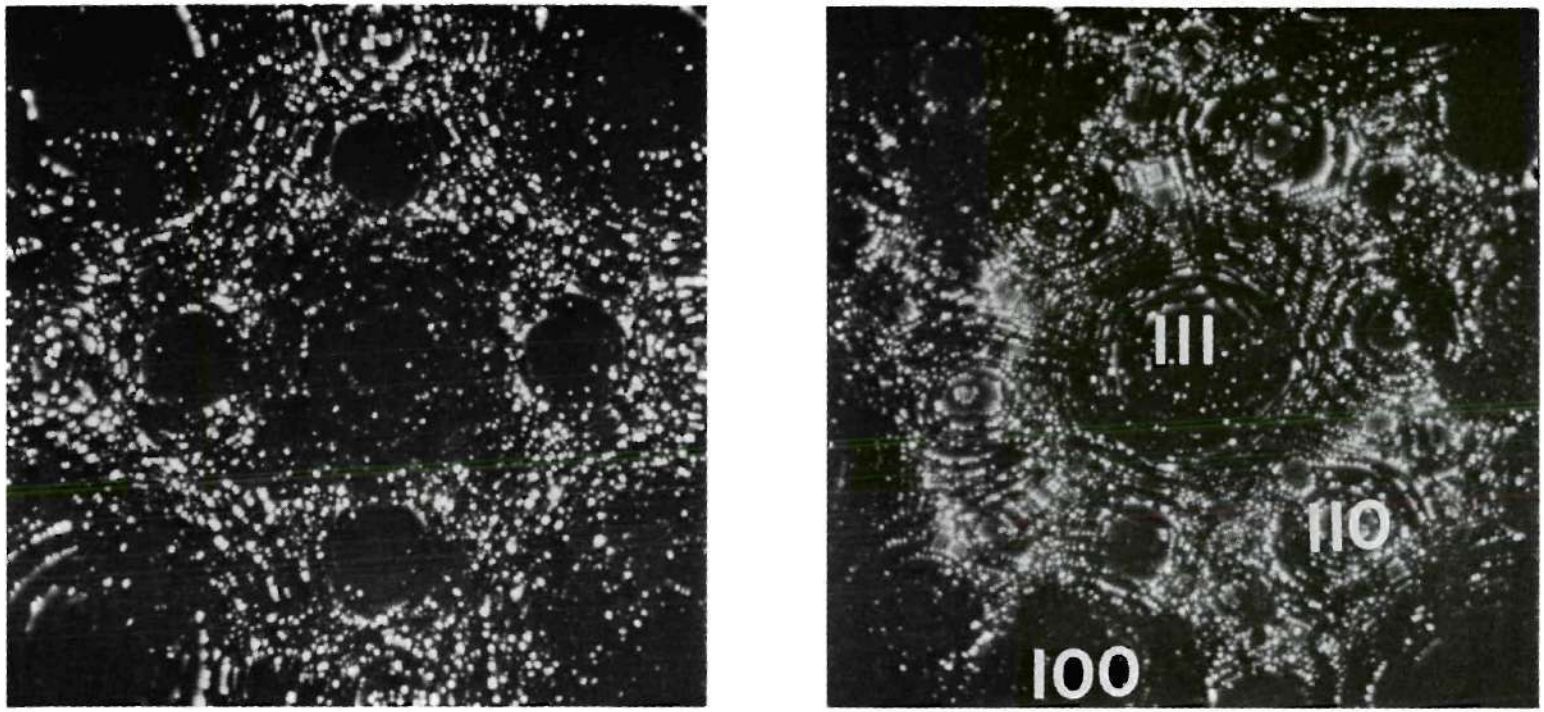

(a) (b)

Figure 7. Iridium after Vacuum Annealing: (a) at 1130°K for 65 Minutes - 16.6 KV (b) at 1125°K for 6 Minutes - 21.0 KV (c) at 1360°K for 32 Minutes - 15.7 KV (d) Flash Heated to Approximately 2200°K - 10.0 KV.

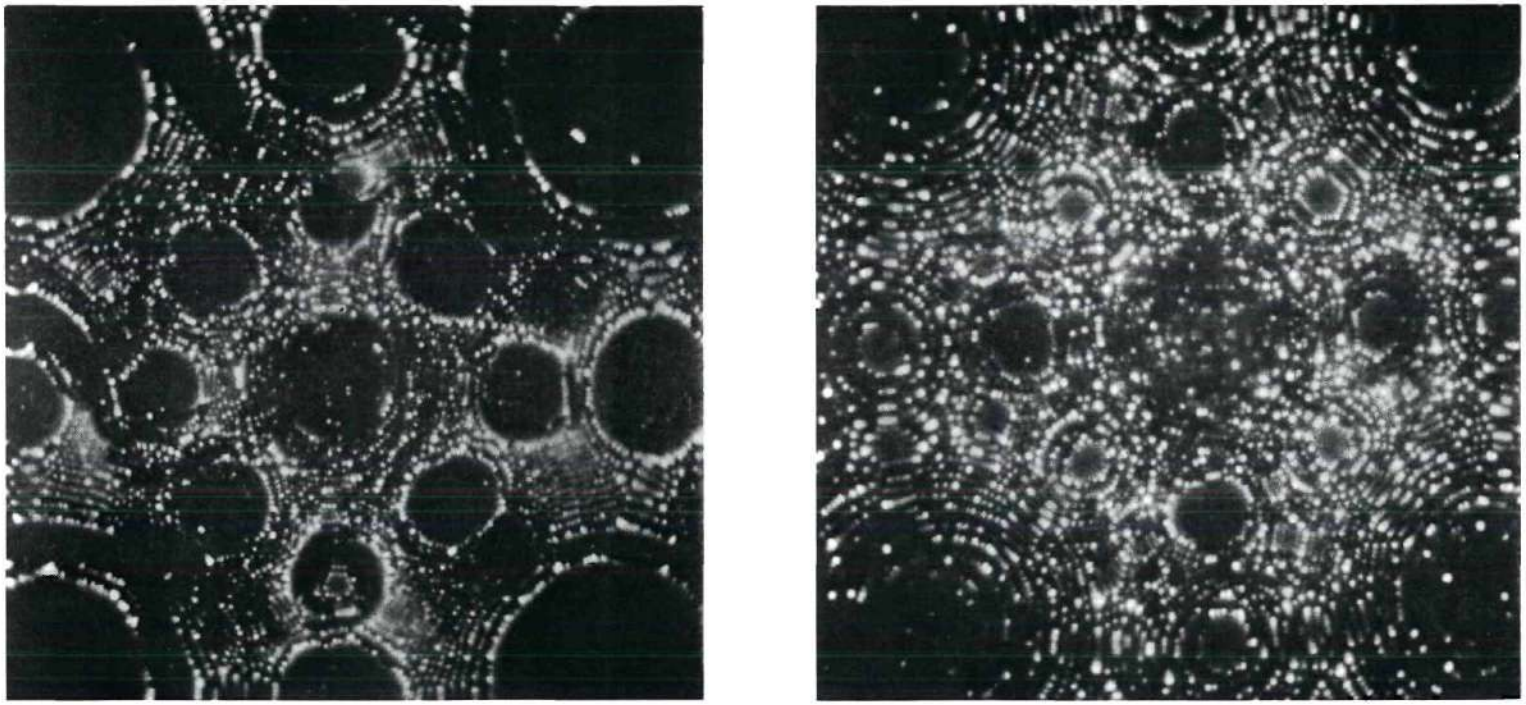

(c) (d)

Figure 7. Iridium after Vacuum Annealing: (a) at 1130°K for 65 Minutes - 16.6 KV (b) at 1125°K for 6 Minutes - 21.0 KV (c) at 1360°K for 32 Minutes - 15.7 KV (d) Flash Heated to Approximately 2200°K -10.0 KV.

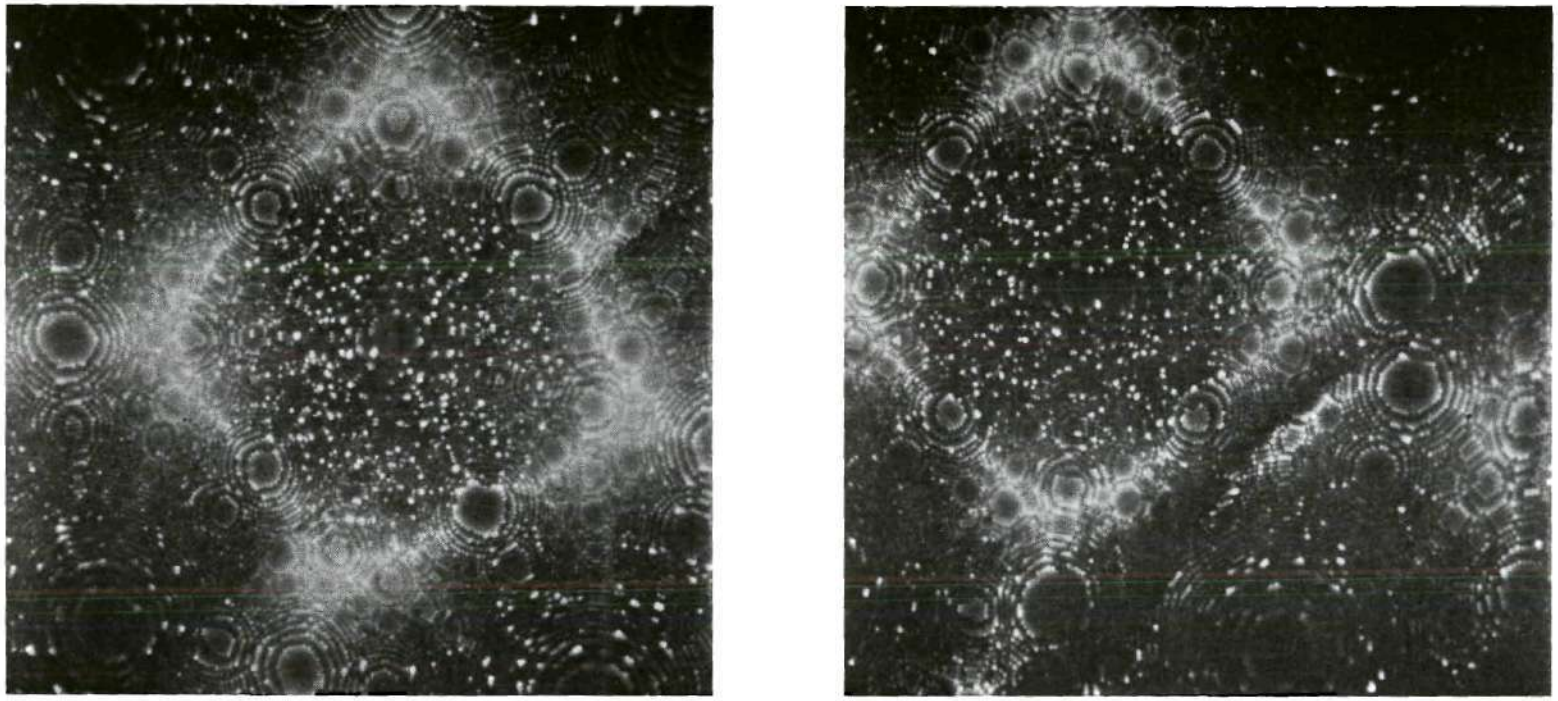

(a) (b)

Figure 8. A Grain Boundary in Iridium:
(a) Before Heating - 18.0 KV (b) After Flash Heating to 1773°K - 17.7 KV.

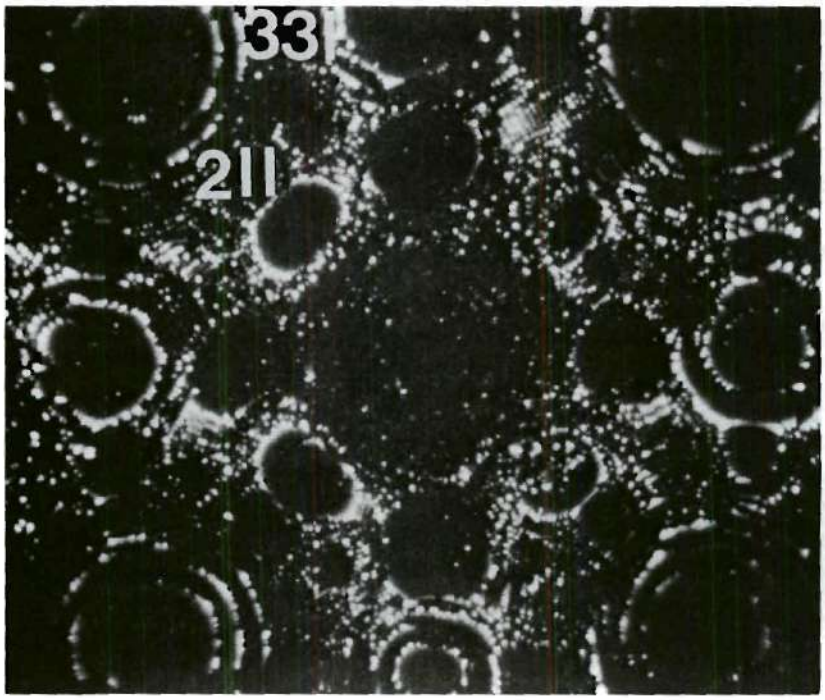

Figure 9. Iridium after Hydrogen Annealing at 1130°K for 65 Minutes -17.0 KV.

annealed in the range of 1300 to 1733°K. The results are therefore subdivided into these temperature ranges.

i) Between 880 and 1170°K

Specimens annealed in this temperature range always contained facets in the following order of decreasing size: (111), (100) and (210) facets. A typical micrograph for a specimen annealed at 1130°K for 65 minutes is shown in Figure 7(a) and is representative of other specimens in this temperature range. The image appeared to show fewer atoms than the field evaporated image; this may be due to surface irregularities developed during annealing. Although the order of faceting did not change for specimens annealed in this temperature range, the size of facets depended upon the temperature and time of annealing.

For one of the iridium specimens, which was annealed for 6 minutes at 1125°K, multiatomic steps were observed in (111), (100) and (110) regions, as shown in Figure 7(b). The step heights were estimated from the number of missing rings to be 2-4 interplanar spacings. After prolonged heating at this temperature the (100) and (110) surface steps could no longer be recognized, and the end form contained the usual (111), (100) and (210) facets observed for other specimens annealed in this temperature range.

ii) Between 1300 and 1733°K

Annealing at or above 1300°K produced facets in the following order of decreasing size: (111), (100), (110), (311) and (210). Figure 7(c) shows a typical end form obtained after annealing for 32 minutes at 1360°K. This end form was essentially the same as that obtained after 16 minutes at the same temperature, indicating that the

end form was close to equilibrium. The micrograph in Figure 7(c) also shows some multiatomic steps in the (111) regions and sharp discontinuities in the (100) rings.

The best image voltage of a given specimen did not change significantly after annealing at 1300 or 1360°K, which indicated that the specimen did not blunt during the treatment. However, some blunting was observed on a specimen flash heated to 1550°K and the blunting was appreciable for specimens annealed at 1733°K.

In one of the experiments, the heating loop broke during flash heating to approximately 2200°K. Examination of the specimen revealed only (210) facets, as shown in Figure 7(d). The size of these facets is comparable to that of (210) facets formed after long annealing periods at temperatures below 1300°K.

Grain boundary migration and possibly grooving were also observed in one of the experiments. Figure 8 shows the micrographs of an iridium specimen with a grain boundary before and after flash heating to 1773°K. In the latter micrograph, the specimen has been partially field evaporated to reveal the new position of the grain boundary; but a dark band, possibly representing grain boundary grooving is still apparent.

b. In Hydrogen. Iridium specimens were annealed in hydrogen at a pressure of 2.5×10^{-3} torr and at the following absolute temperatures (time, in minutes): 790 (4), 890 (32), 1130 (30,65), 1140 (5), 1190 (5) and 1330 (16,32). The hydrogen coverage was calculated, as described in Appendix B, using an activation energy of 34 k cal/mole for hydrogen desorption[67] and found to be 1.0, 0.5, 0.009, 0.008, 0.004 and 0.0009, respectively, at the temperatures given above.

The specimen annealed at 790°K revealed no facets. All other specimens, with one exception, revealed facets similar to those found on specimens annealed in vacuum at the same temperature, that is, the order of decreasing size was (111), (100) and (210) in the temperature range of 890 - 1190°K and (111), (100), (110), (311) and (210) at 1330°K. However, for a given temperature and time, the facets formed in hydrogen did appear to be slightly larger than those formed in vacuum.

The one exception to the above observations on facet size order occurred for the specimen annealed at 1130°K for 65 minutes. A micrograph of this specimen is shown in Figure 9. In this case the order of decreasing size of facets corresponded to approximately that observed on specimens annealed in vacuum at 1300°K or higher, that is, (111), (100), (110), (311) and (210). In addition facets of (211) and (331) planes were also observed on the micrograph.

2. Surface Energy Anisotropy

a. In Vacuum. The surface energy anisotropy can only be calculated from the equilibrium end form at a particular temperature. The end forms at temperatures lower than 1300°K revealed (210) facets, but no (110) facets. The (210) planes are of higher surface energy (see Section II-A-1) than (111), (100) and (110) planes; therefore, the (210) facets formed at lower temperatures, 880-1170°K, are in contradiction to the surface energy models and presumably do not represent the equilibrium end form.

The proper facet size order (111), (100) and (110) was observed for specimens annealed at 1300 and 1360°K. The end form after annealing for 32 minutes at 1360°K, Figure 7(c), was chosen for surface energy

anisotropy calculations for the following reasons. The observed angular width of (111) facets after annealing for 16 minutes at 1300 and 1360°K were 20.0 and 27.0 degrees, respectively; the smaller angular width at 1300°K indicated a higher surface energy for (111) planes or a lower maximum anisotropy. Since the surface energy anisotropy should increase as the temperature is lowered,[37] the end form at 1300°K was not an equilibrium one. The end form after annealing for 16 minutes at 1360°K, however, appeared to be close to the equilibrium shape since annealing for an additional 16 minutes at this temperature produced only an approximately 10% change in the observed (111) facet size. The latter end form, Figure 7(c), was therefore selected for the analysis of surface energy anisotropy.

The true facet sizes were obtained by multiplying the measured facet sizes on the micrograph times the appropriate correction terms (see Section II-C-1c). For the (111), (100), (110), (311) and (210) regions, respectively, the local radii of curvatures were found to be 1070, 925, 710, 765, and 570 Å and the magnification terms, (M_o/M_r), were 1.131, 1.025, 0.858, 0.903 and 0.741. The contraction term, (M_o/M_k) was calculated from a partially field evaporated end form after thermal faceting and was found to be 1.367.

The true facet sizes were then used to calculate the surface energy anisotropy (see Section III-C-1a). The results of these calculations are given in Table 5. The maximum surface energy anisotropy, λ_{max}, was calculated from the true size of the (111) facet.

b. In Hydrogen. A comparison of the measured angular width of the facets formed in hydrogen and in vacuum at 1130°K after 65 minutes is

Table 5. Surface Energy Anisotropy of Iridium at 1360°K

Plane hkl	Measured Facet Size (in degrees)	Correction Term M_o/M_r X M_o/M_k	True Facet Size (in degrees)	Anisotropy λ_{hkl}
(111)	30.02	1.546	46.41	1.000
(100)	22.64	1.401	31.72	1.047
(110)	17.90	1.173	21.00	1.070
(311)	12.64	1.123	15.61	1.078
(210)	12.64	1.013	12.80	1.081
λ_{max}	-	-	-	1.088

given in Table 6. It is seen that the facets formed in hydrogen were larger than those formed in vacuum, and the order of decreasing size for the former facets was approximately the same as that for facets formed in vacuum at temperatures of 1300°K and above.

3. Kinetics of Faceting

a. Measured Growth Rates and Activation Energy. The growth rates of (111) facet were measured at 1125 and 1170°K. A logarithmic plot of the data, expressed as change in facet size, $d - d_o$, versus time, t, gave two nearly parallel straight lines with slopes 0.36, as shown in Figure 10. The change in facet size was therefore proportional to $t^{0.36}$. A similar plot of facet size, d, versus time showed that the facet size was proportional to $t^{0.20}$.

The following method[3] was used to determine the activation energy for growth of (111) facets. The time required, τ, for a change in facet size of 100 Å was found from the curves shown in Figure 10 and was plotted versus the reciprocal of the absolute temperature, T, as shown in Figure 11. The third point on the latter curve, corresponding to a temperature of 880°K, was obtained from a single measurement of change in facet size after 10 minutes (indicated as a point in Figure 10) and by assuming its growth curve to be parallel to the other two curves in Figure 10. The slope of the curve in Figure 11 is related to the activation energy, Q_s, according to the following equation:

$$\partial(\log \tau)/\partial(1/T) = - Q_s/2.3\ R$$

where R is the gas constant. The activation energy was found to be 45.7 k cal/mole.

Table 6. Angular Widths of Various Facets on the Iridium End Forms Annealed at 1130°K for 65 Minutes.

Plane hkl	In Hydrogen (in degrees)	In Vacuum (in degrees)
(111)	17.7	17.0
(100)	14.8	14.3
(110)	15.2	-
(311)	11.0	-
(210)	14.3	12.0

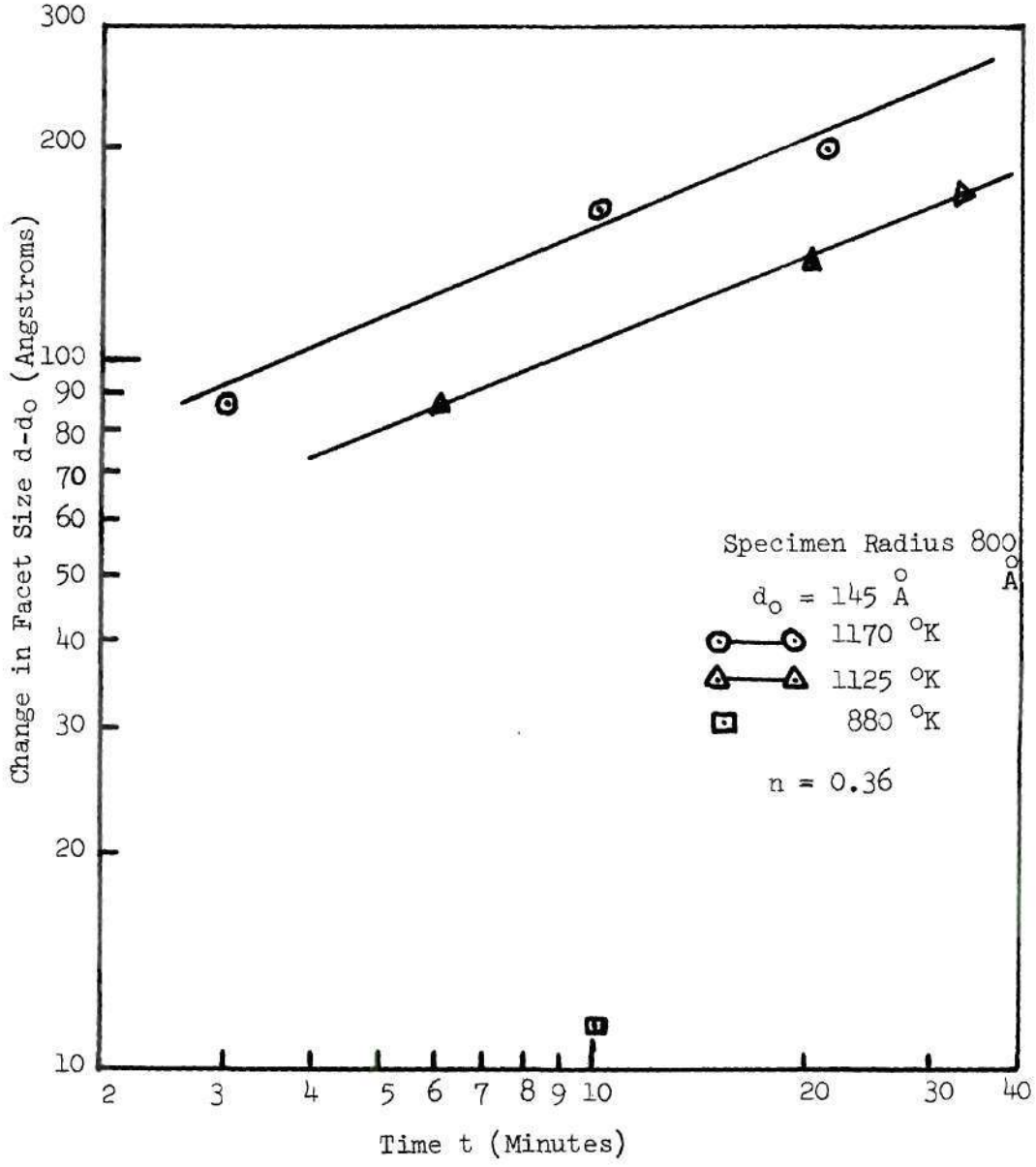

Figure 10. Growth of Iridium (111) Facets in Vacuum as a Function of Time.

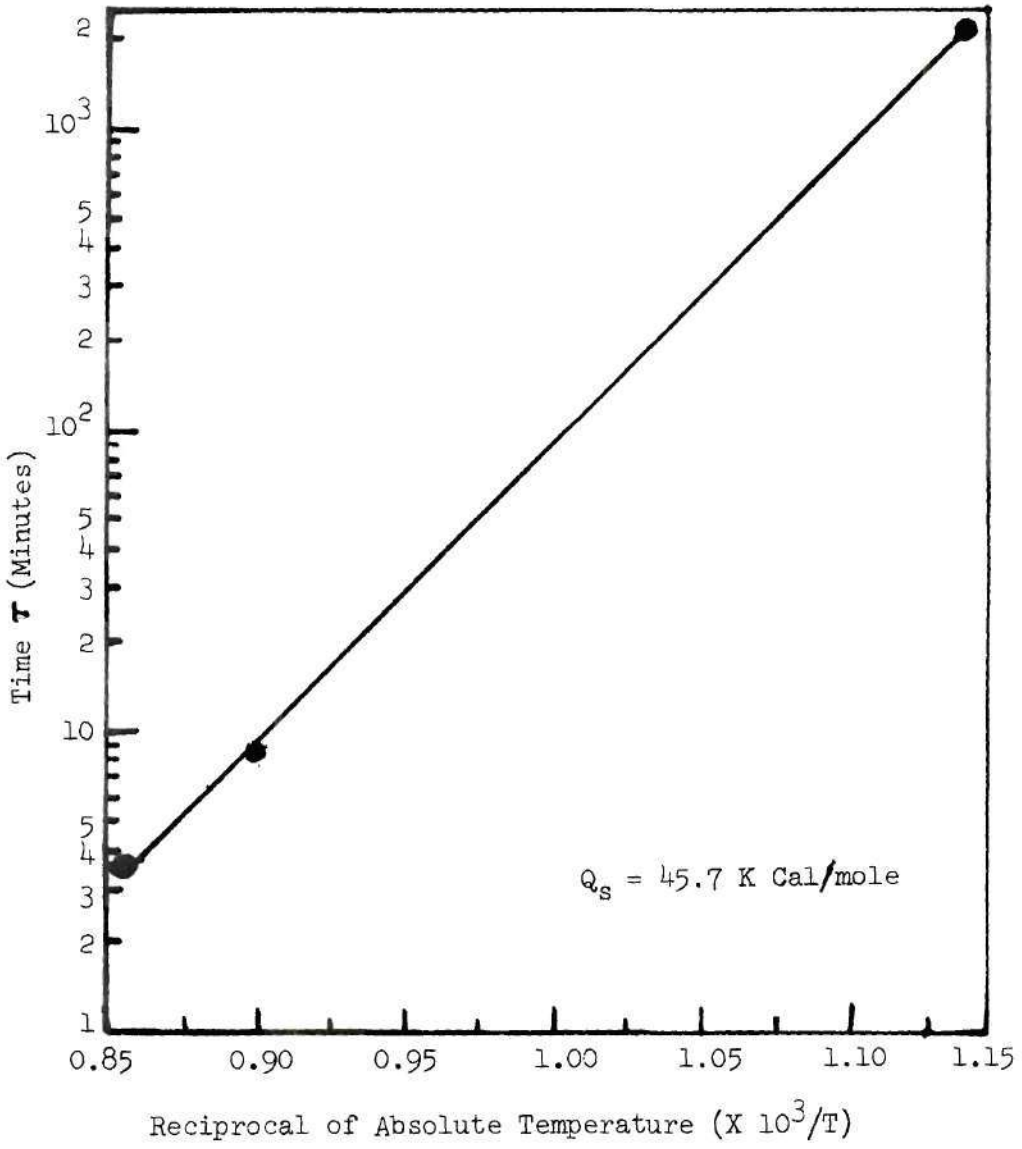

Figure 11. Temperature Dependence of Time at Which $d-d_o$ Equals 100 Å.

b. Mathematical Growth Rates. The mathematical growth curves were plotted by the calcomp plotter, as described in Section III-C-2b. Figure 12 shows the change in facet size, $d-d_o$, and the facet size, d, plotted as a function of time for a specimen with a radius of 800 Å and with value of X_F varying from 0 to 0.50. From the approximate slopes of these curves it was found that the time exponent, n, in the equation for $d-d_o$ varied from 0.40 to 0.45 and in that for d varied from 0.21 to 0.26 as the value of X_F was increased from 0 to 0.50. The value of n in either case did not change significantly as the specimen radius was varied at a fixed value of X_F, as shown in Figure 13. For $X_F=0$, as the radius was increased from 600 to 1300 Å, the time exponent in the $d-d_o$ equation varied from 0.40 to 0.43 while in the d equation it was constant and equaled 0.21.

B. Tungsten

1. Thermally Faceted End Forms

Helium gas and a specimen temperature of 78°K were used to observe field evaporated and thermally annealed end forms of tungsten. Prior to thermal faceting experiments, the specimens were cleaned by flash heating at approximately 2300°K and by field evaporating to a nearly hemispherical end form. A typical micrograph of a specimen cleaned by flash heating is shown in Figure 14(a). When the specimen was not clean a characteristic built-up structure was observed on the (100) and (111) regions after flash heating. These specimens with a built-up structure were flashed repeatedly until an end form similar to that shown in Figure 14(a) was obtained. A typical micrograph of a field evaporated end form is shown in Figure 14(b).

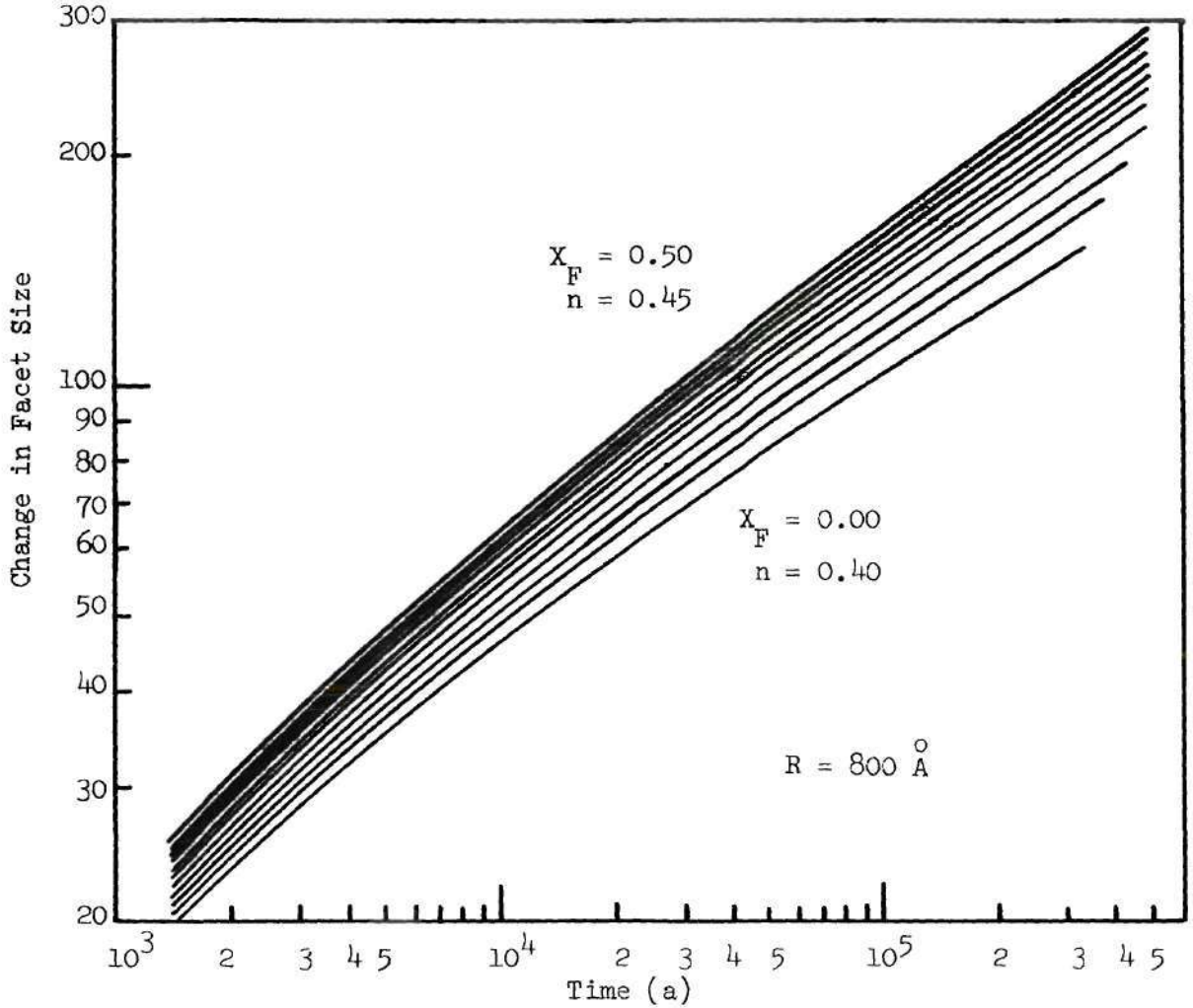

Figure 12. Mathematically Calculated Growth of Iridium (111) Facet for Various Values of X_F ($R = 800\ A^{\circ}$):
(a) Change in Facet Size versus Time (b) Facet Size versus Time

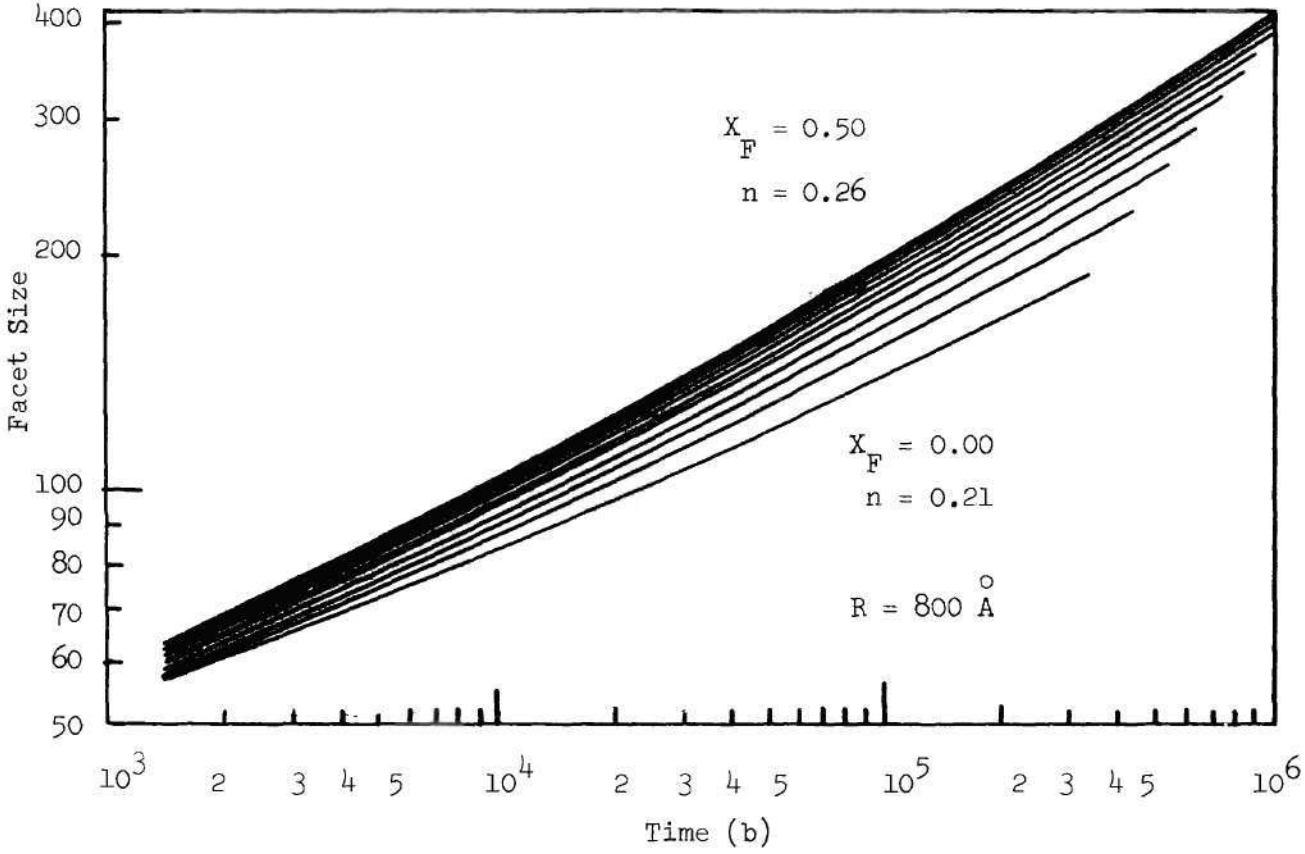

Figure 12. Mathematically Calculated Growth of Iridium (111) Facet for Various values of X_F (R = 800 Å):

(a) Change in Facet Size versus Time (b) Facet Size versus Time

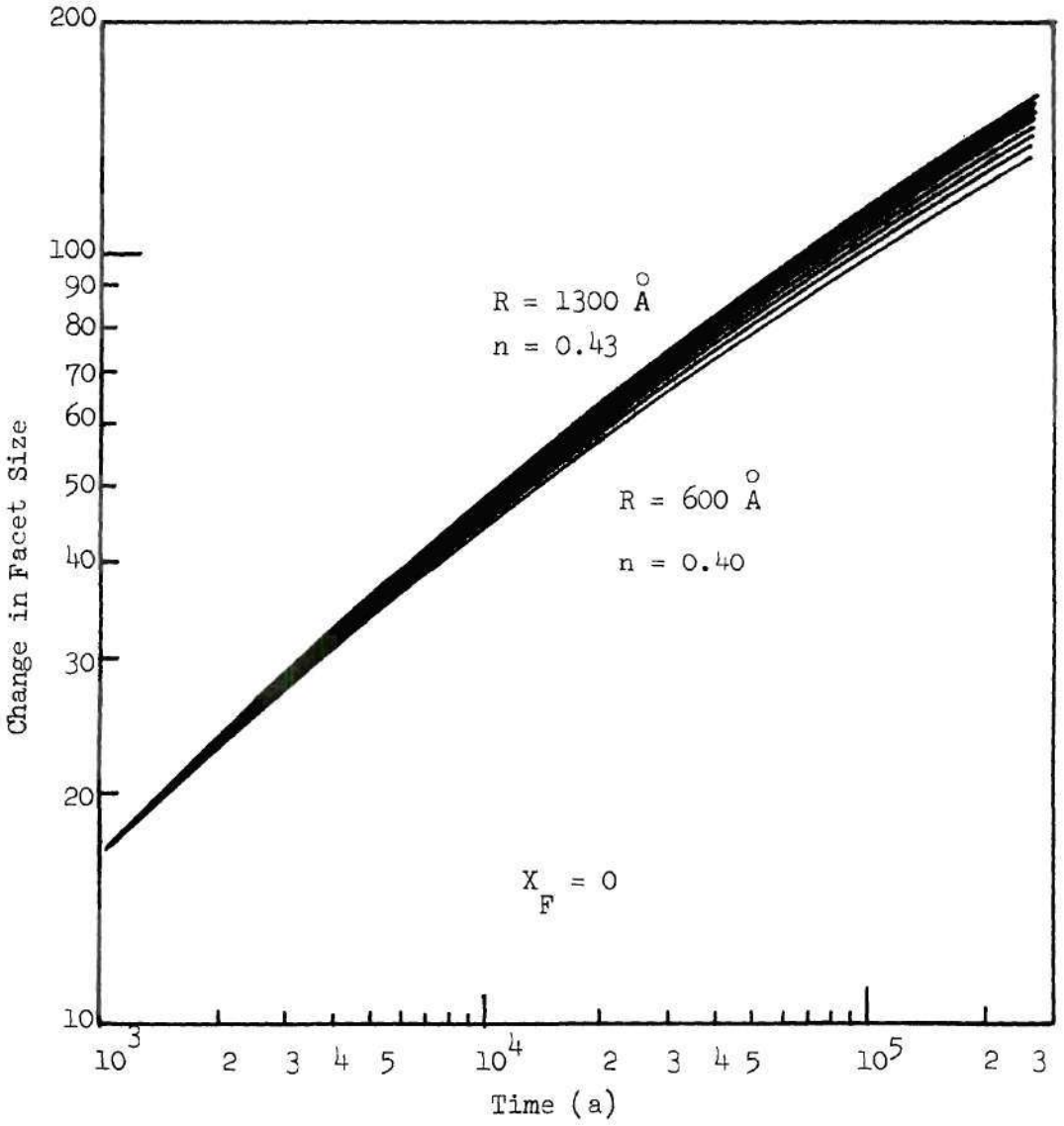

Figure 13. Mathematically Calculated Growth of Iridium (111) Facet for Various Specimen Radii (X_F=0):

(a) Change in Facet Size versus Time

(b) Facet Size versus Time

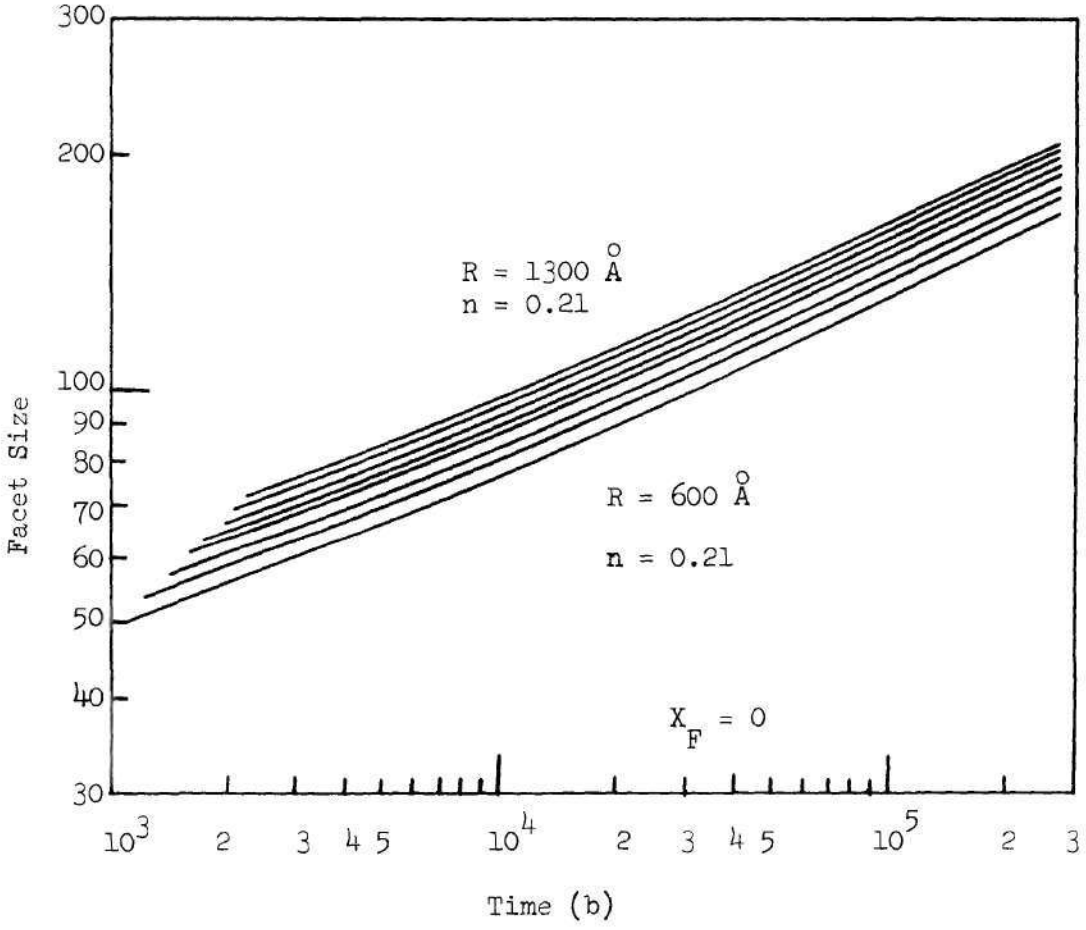

Figure 13. Mathematically Calculated Growth of Iridium (111) Facet for Various Specimen Radii (X_F=0):

(a) Change in Facet Size versus Time

(b) Facet Size Versus Time.

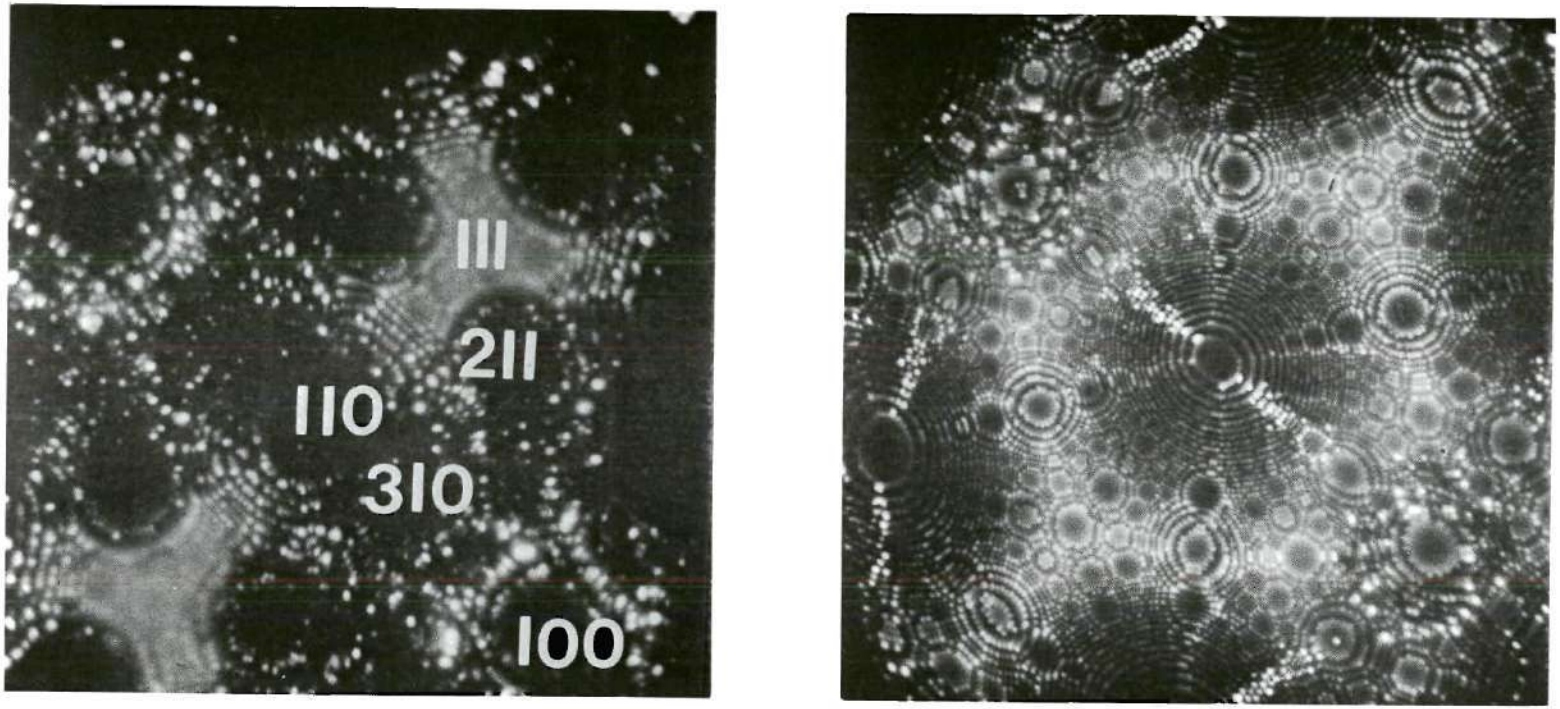

(a) (b)

Figure 14. Typical Tungsten Specimens: (a) After Flash Heating to Approximately 2200°K - 11.9 KV (b) After Field Evaporation -19.4 KV.

Typical micrographs of tungsten after various heat treatment are shown in Figures 15-16. The important features of these micrographs are given below according to the environment during annealing.

a. In Vacuum. Tungsten specimens were annealed in vacuum at the following absolute temperatures (time, in minutes): 760(32), 1000(10), 1130(10), 1210(3), 1325(16), 1425(5,30), 1550(15), 1780(5), 1860(1), T_A (1,2,4,8,16) and T_B (4.25, 8.25), where T_A and T_B were constant, but not measured, and estimated to be approximately 1750°K. Other tungsten specimens were annealed in helium at 10^{-4} torr pressure as follows: 910(8), 1200(1), 1700(2), 2100(2.5). Some specimens were annealed in hydrogen at 10^{-4} torr at the following temperatures: 1350(6), 1380(24), 1630(1.67). The hydrogen coverage at these temperatures corresponded to less than 0.0002, which is assumed negligible. No significant differences were expected or found between specimens annealed in helium or hydrogen and those annealed in vacuum, and the results are therefore considered to be representative of vacuum annealing in all cases.

The specimen annealed at 760°K did not show any faceting; however, some surface roughness was observed in the micrograph. The specimens annealed at 910 and 1000°K showed (110) and (211) facets along with some surface rearrangements in the (111) and (110-111) regions. For specimens annealed at 1130°K, the order of decreasing facet size was (110), (211), (111) and (100), as shown in Figure 15(a). The micrograph shows fewer atoms presumably due to surface irregularities that developed during annealing.

Annealing at or above 1200°K produced facets in the following order of decreasing size: (110), (211), (100) and (310). As the specimen was

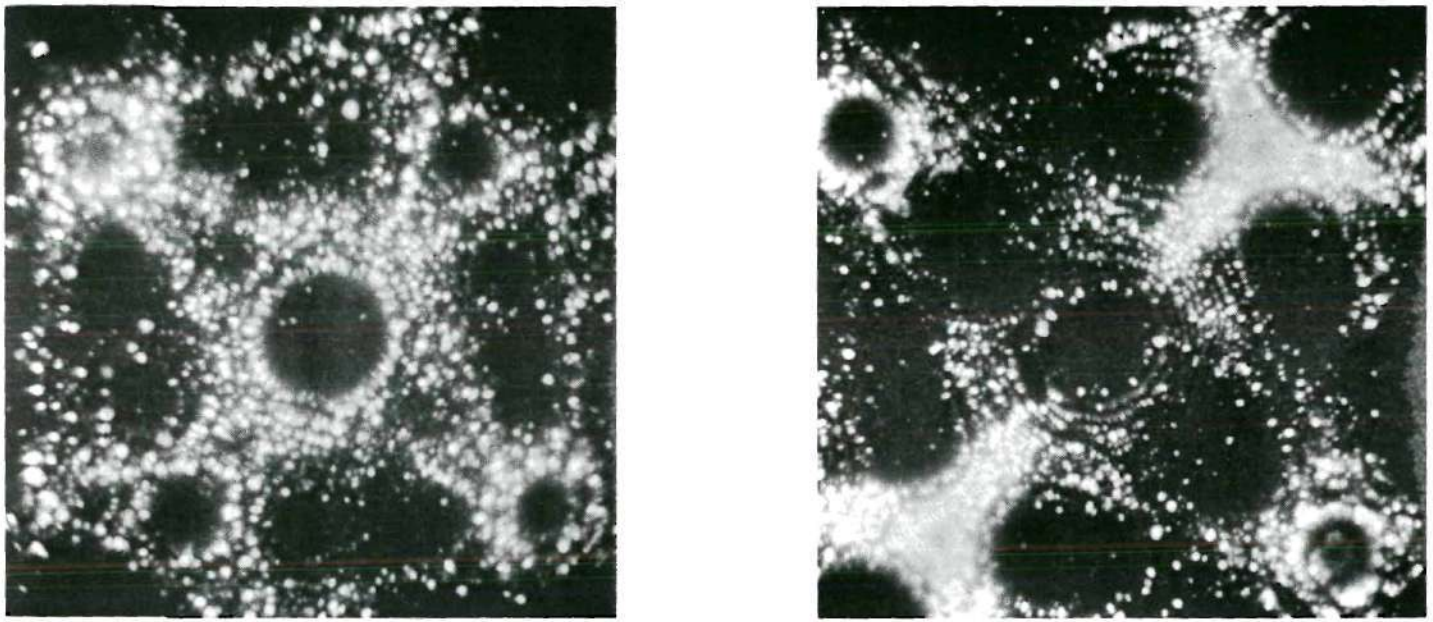

(a) (b)

Figure 15. Tungsten after Vacuum Annealing: (a) at 1130°K for 10 Minutes - 16.4 KV (b) at 1780°K for 5 minutes -18.1 KV.

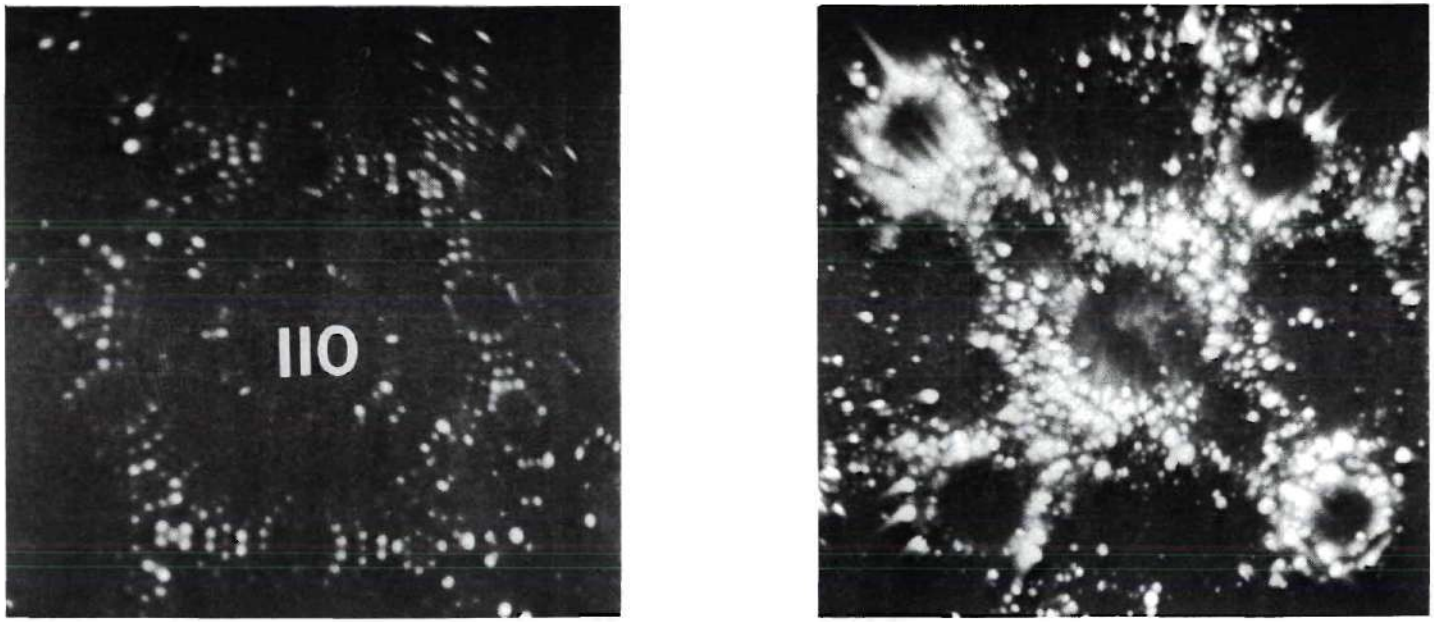

(a) (b)

Figure 16. Tungsten after Hydrogen Annealing: (a) at 650°K for 1020 Minutes - 9.2 KV (b) at 1130°K for 10 Minutes - 15.0 KV.

heated at higher temperatures or for longer times, the order of facets did not change, but the size of the facets depended upon the temperature and time of heating. Figure 15(b) is an end form after annealing at 1780°K for 5 minutes and is a representative of the end forms obtained above 1200°K. In addition to facets, the micrograph shows surface rearrangements in the region bounded by the (110-100-211) triangle. The size of facets did not change significantly when the specimen was heated to 1860°K.

The best imaging voltage did not change significantly after annealing at 1780 or 1860°K, which indicated that the specimens did not blunt during the treatment. However, blunting was observed for specimen annealed at 2100°K.

b. In Hydrogen. A list of experimental conditions for tungsten specimens annealed in hydrogen is given in Table 7. The hydrogen coverage at each temperature was calculated, as shown in Appendix B, using an activation energy of 33 k cal/mole[68] for hydrogen desorption.

The specimens annealed at 650°K for 210 and 600 minutes did not reveal any facets. When the annealing was prolonged to 1020 minutes, the (110) facets did form, as shown in Figure 16(a). The specimen annealed at 780°K for 32 minutes did not reveal any facets, however, some surface rearrangements were observed. The end form at 960°K revealed (110) and (211) facets, similar to the vacuum annealed end forms at 910 and 1000°K. The hydrogen annealed end form at 1040°K showed the order of decreasing facet size as follows: (110), (211), (100) and (310). This order was the same as that obtained after vacuum annealing at or above 1200°K. The specimens annealed at 1130 and 1210°K in hydrogen coverage of 0.33 and 0.58, respectively, revealed the order of decreasing facet size as

Table 7. Experimental Conditions for Tungsten Specimens Annealed in Hydrogen.

Temperature ^{o}K	Time, minutes	Hydrogen Pressure in Torr.	Coverage
650	210,600,1020	9.4×10^{-3}	1.0
780	32	50×10^{-3}	1.0
960	5.67	6.3×10^{-3}	0.2
1040	10	1000×10^{-3}	1.0
1130	10	150×10^{-3}	0.33
1210	3	700×10^{-3}	0.58
1270	1	7×10^{-3}	0.003
1330	16	13×10^{-3}	0.003

follows: (110), (211), (100), (111) and (310). A typical micrograph of the end form at 1130°K after 10 minutes is shown in Figure 16(b). These facets formed in hydrogen appeared to be larger than the corresponding facets formed in vacuum, Figure 15(a). The specimens annealed at 1270 and 1330°K revealed end forms similar to the vacuum annealed end forms at or above 1200°K, i.e. (110), (211), (100) and (310) facets.

2. Surface Energy Anisotropy

a. In Vacuum. The end forms at temperatures lower than 1130°K revealed (211) facets, but no (100) facets, which were predicted by the theoretical surface energy calculations reported in Section II-A-1. The end form at 1130°K revealed small (100) facets than (211) and (111) facets, which was also not expected from the calculations. The true facet size order (110), (100), (211) and (310), observed at and above 1200°K, was in agreement with the theoretical calculations. The specimens annealed above 1200°K, but below 1780°K, did not represent equilibrium, because of the lower maximum surface energy anisotropies than those revealed at 1780 and 1860°K. The end form after annealing for 5 minutes at 1780°K, however, appeared to be close to the equilibrium shape, since annealing at a higher temperature of 1860°K produced only an approximately 8% change in the observed (110) facet size. Therefore the micrographs of the specimen annealed at 1780°K for 5 minutes were used to find the surface energy anisotropy of tungsten.

The true facet sizes were obtained by multiplying the measured facet sizes on the micrographs times the appropriate correction terms (see Section II-C-1c). For the (110), (100), (211) and (310)regions, the local radii were found to be 1025, 725, 575 and 600 Å, respectively, and

the corresponding magnification terms, M_o/M_r, were 1.429, 1.132, 0.971 and 1.000. The contraction term, M_o/M_k, was calculated from a partially field evaporated end form after thermal faceting and was found to be 1.21.

The true facet sizes were then used to calculate the surface energy anisotropy (see Section III-C-1a). The results of these calculations are given in Table 8. The maximum surface energy anisotropy, λ_{max}, was calculated from the true size of the (110) facet.

b. In Hydrogen. A comparison of the measured angular widths of facets formed in hydrogen and in vacuum at 1130°K after 10 minutes is given in Table 9. It is seen that the facets formed in hydrogen were 1-3 degrees larger than those formed in vacuum for these conditions.

3. Kinetics of Faceting

a. Measured Growth Rates and Activation Energy. The growth of (110) facets were measured at approximately 1750°K for two specimens. A logarithmic plot of the data, expressed as change in facet size, $d-d_o$, versus time, t, gave a straight line with slope nearly equal to 0.315, as shown in Figure 17. The change in facet size was therefore proportional to $t^{0.315}$. A similar plot of facet size, d, versus time showed that the facet size was proportional to $t^{0.20}$.

The activation energy for growth of (110) facets, in the temperature range of 1350 to 1700°K, was determined by the method described previously for iridium. The change in facet size, $d-d_o$, was measured at various temperatures after a selected period of time. This data is given in Table 10. Also given in this table are the extrapolated values for the time, τ, required for a change in facet size of 70 Å, assuming the slope of the logarithmic plot of $d-d_o$ versus time equal to 0.315, as

Table 8. Surface Energy Anisotropy of Tungsten at 1780°K

Plane hkl	Measured Facet Size (in degrees)	Correction Term M_o/M_r X M_o/M_k	True Facet Size (in degrees)	Anisotropy λ_{hkl}
(110)	19.18	1.729	33.16	1.000
(100)	14.51	1.370	19.88	1.028
(211)	16.48	1.175	19.36	1.030
(310)	14.02	1.210	16.96	1.032
λ_{max}	-	-	-	1.043

Table 9. Angular Widths of Various Facets on the Tungsten End Forms Annealed at 1130°K for 10 Minutes.

Plane hkl	In Hydrogen (in degrees)	In Vacuum (in degrees)
(110)	23.5	21.2
(100)	13.2	12.2
(211)	16.8	14.2
(310)	13.5	12.4
(111)	15.8	12.9

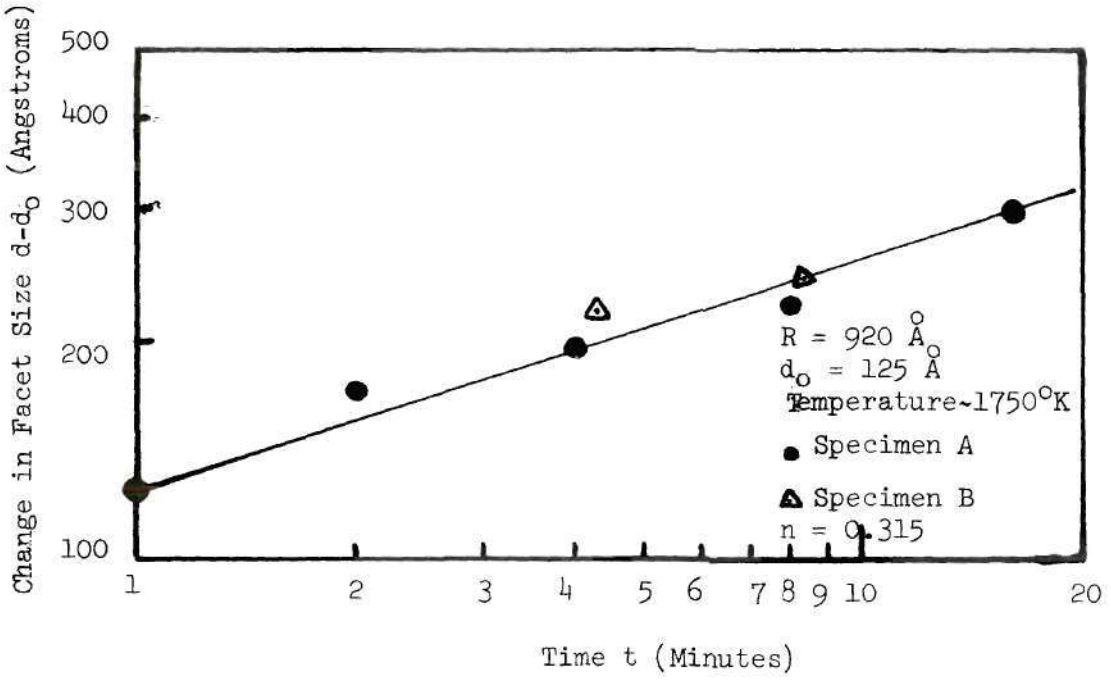

Figure 17. Growth of Tungsten (110) Facets in Vacuum as a Function of Time.

Table 10. Temperature Dependence of τ, Time for Change in Tungsten (110) Facet Size of 70 Å

Temperature °K T	$10^3/T$	Time Minutes	Measured Change in Facet Size Å	τ Minutes
1350	0.740	6	28	100
1380	0.725	27	54	62
1425	0.700	5,30	35,67	33
1630	0.614	1.67	56	3.4
1700	0.588	2	74	1.7

determined above at 1750°K. The time, τ, was then plotted against the reciprocal of the absolute temperature, as shown in Figure 18, and the activation energy, Q_s was found to be 54.5 k cal/mole.

b. Mathematical Growth Rates. Mathematical growth curves were plotted by the calcomp plotter as described in Section III-C-2b. Figure 19 shows the change in facet size, $d-d_o$, and the facet size, d, plotted as a function of time for a specimen with a radius of 800 Å and with value of X_F varying from 0 to 0.50. From the approximate slopes of these curves, it was found that the time exponent, n, in the equation for $d-d_o$ varied from 0.39 to 0.45 and in that for d varied from 0.21 to 0.24 as the value of X_F was increased from 0 to 0.50. The value of n did not vary significantly as the specimen radius was varied at a fixed value of X_F, as shown in Figure 20. For $X_F=0$, as the radius was increased from 600 to 1300 Å, the time exponent in the $d-d_o$ equation varied from 0.38 to 0.41 while in the d equation it varied from 0.21 to 0.20.

C. Iron

1. Thermally Faceted End Forms

Iron specimens were always imaged at 78°K in hydrogen gas. Hydrogen is known to give poorer resolution than neon and to interact with iron during imaging.[43] However, hydrogen imaging was convenient and also completely adequate in these studies for the following reasons. First, the facet sizes were large enough that atomic resolution was unnecessary to obtain the required information. The error involved would be about 1° in angular width, which compared to the observed angular width of facets reported below is only a 2-5% error. Second,

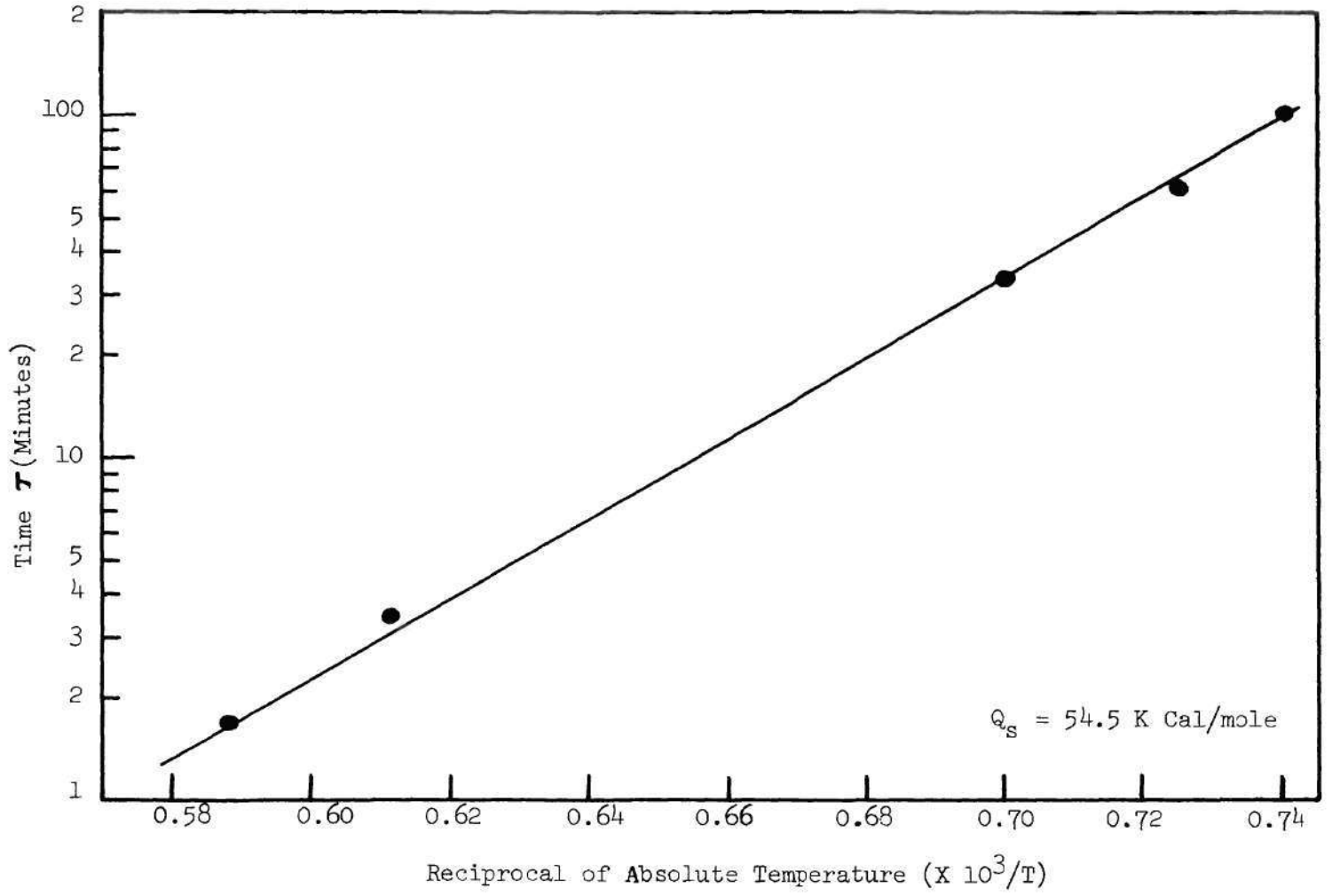

Figure 18. Temperature Dependence of Time at Which d-d_o Equals 70 Å.

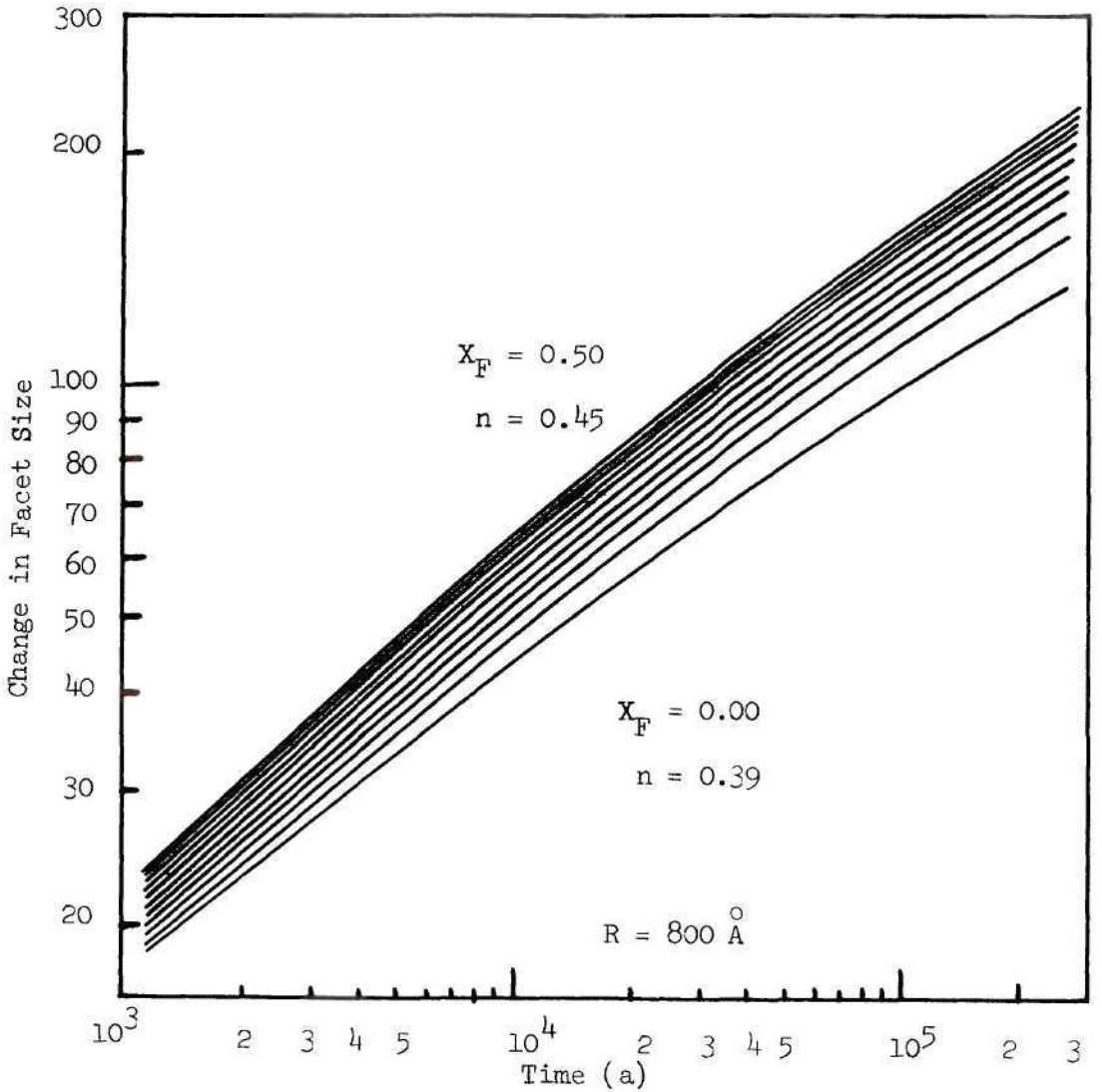

Figure 19. Mathematically Calculated Growth of Tungsten (110) Facet for Various Values of X_F (R=800Å): (a) Change in Facet Size versus Time (b) Facet Size versus Time.

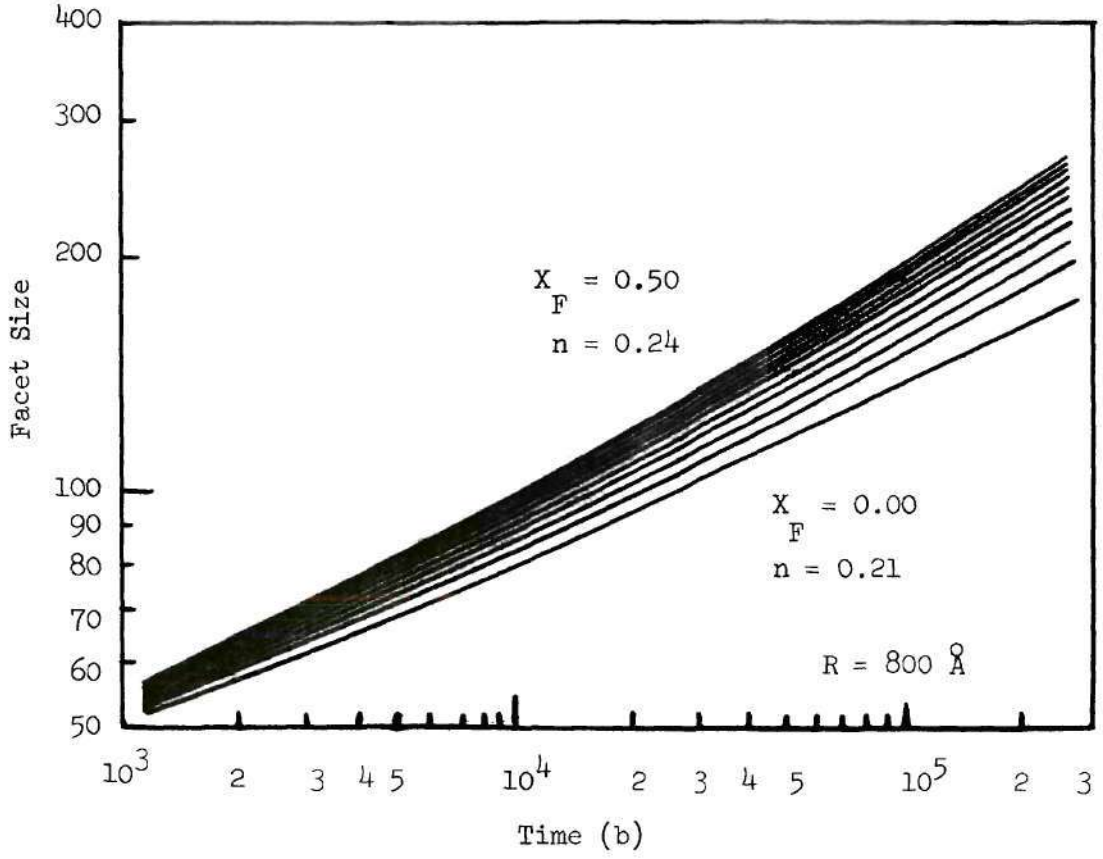

Figure 19. Mathematically Calculated Growth of Tungsten (110) Facet for Various Values of X_F (R = 800 Å):

(a) Change in Facet Size versus Time (b) Facet Size versus Time

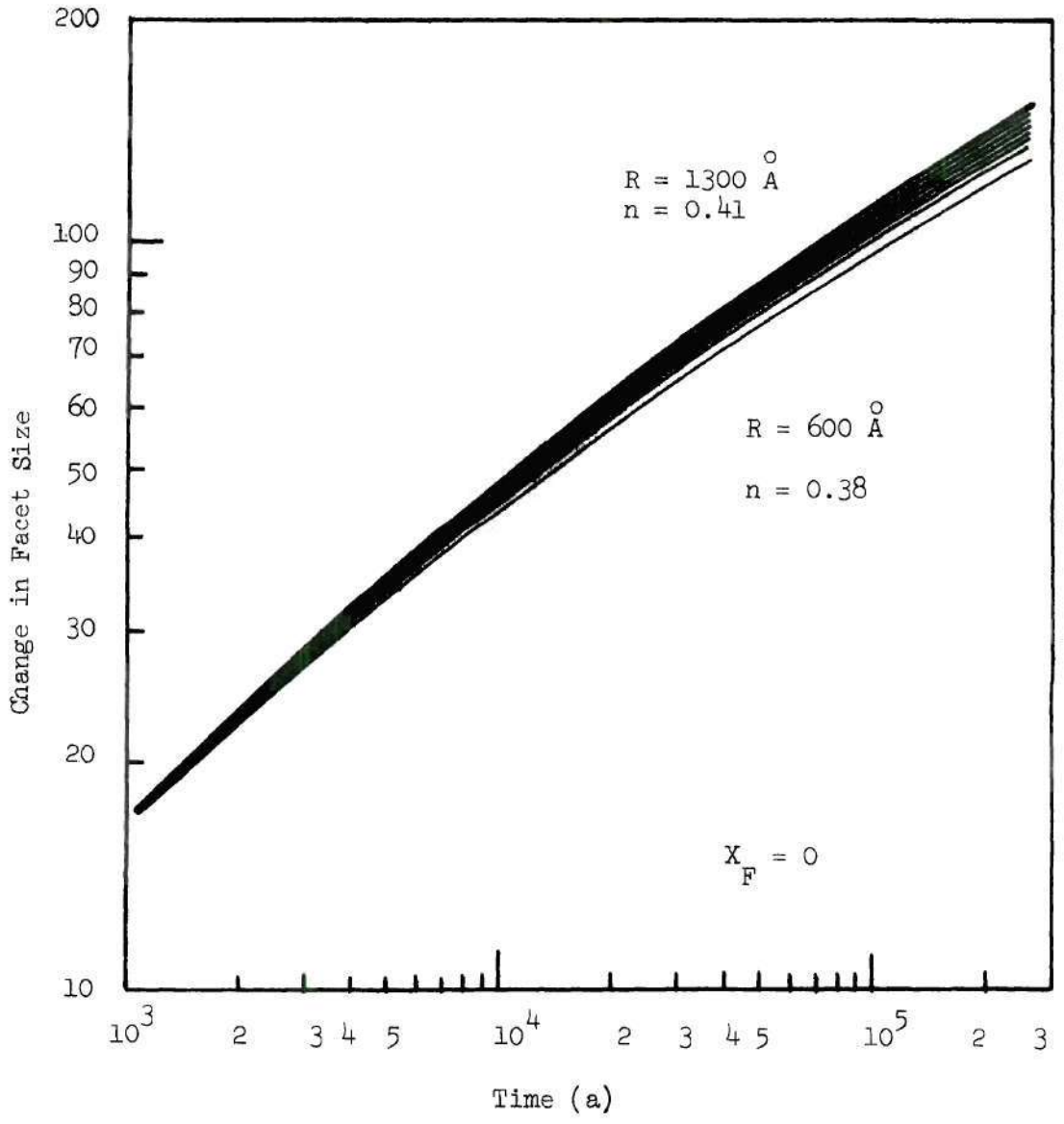

Figure 20. Mathematically Calculated Growth of Tungsten (110) Facet for Various Specimen Radii (X_F = 0):

(a) Change in Facet Size versus Time

(b) Facet Size versus Time.

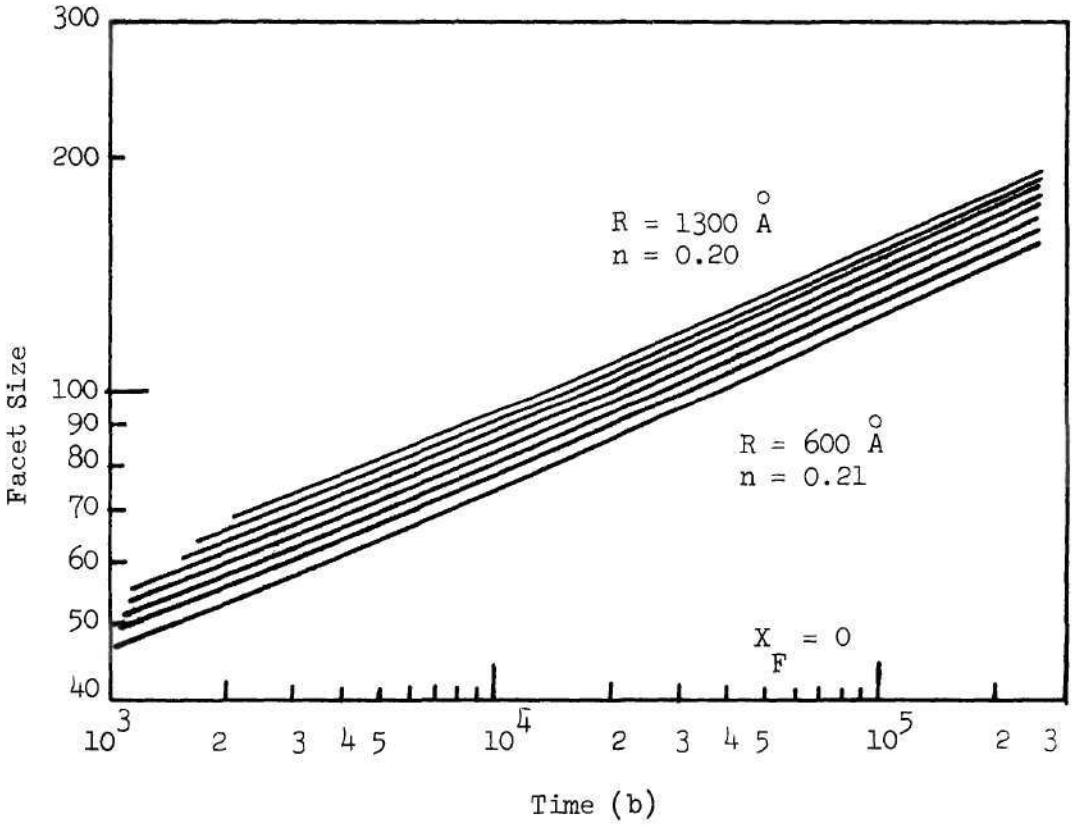

Figure 20. Mathematically Calculated Growth of Tungsten (110) Facet for Various Specimen Radii ($X_F = 0$):

(a) Change in Facet Size versus Time

(b) Facet Size versus Time.

the degree of image stability during hydrogen imaging is known to depend on the residual gases in the system. In the present studies the system was thoroughly baked out, and the residual gas pressure was in the 10^{-9} torr range. The observed hydrogen image in these studies was so stable that no ring decay was noticable during the time required to obtain and photograph the image.

In contrast to iridium and tungsten oxides, the iron oxide could not be thermally decomposed because all efforts to flash clean at approximately 1300°K resulted in specimen blunting. Therefore, prior to the faceting studies, iron specimens were chemically cleaned for 3 minutes at 800°K in hydrogen at a pressure of 10^{-2} torr. The temperature 800°K was selected because it is high enough for reduction of oxide and low enough to prevent blunting. A hydrogen pressure of 10^{-2} insured monolayer coverage assuming the heat of desorption for hydrogen to be 32 k cal/mole[67] (see Appendix B).

Hydrogen is soluble in iron to some extent at this temperature[67] and pressure. Therefore the specimens were degassed at this temperature in a vacuum of 10^{-9} torr for an additional 3 minutes to remove the dissolved hydrogen.

A typical micrograph of a specimen which had been prepared as above and then field evaporated to a nearly hemispherical end form is shown in Figure 21.

Typical micrographs of iron after various heat treatments are shown in Figures 22-25. The important features of these micrographs are given below according to the environment during annealing.

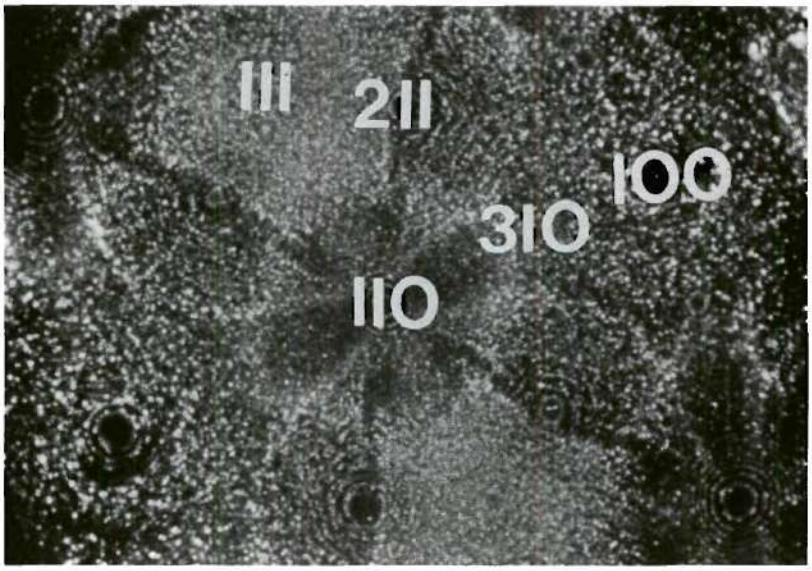

Figure 21. Typical Field Evaporated Iron Specimen - 18.0 KV.

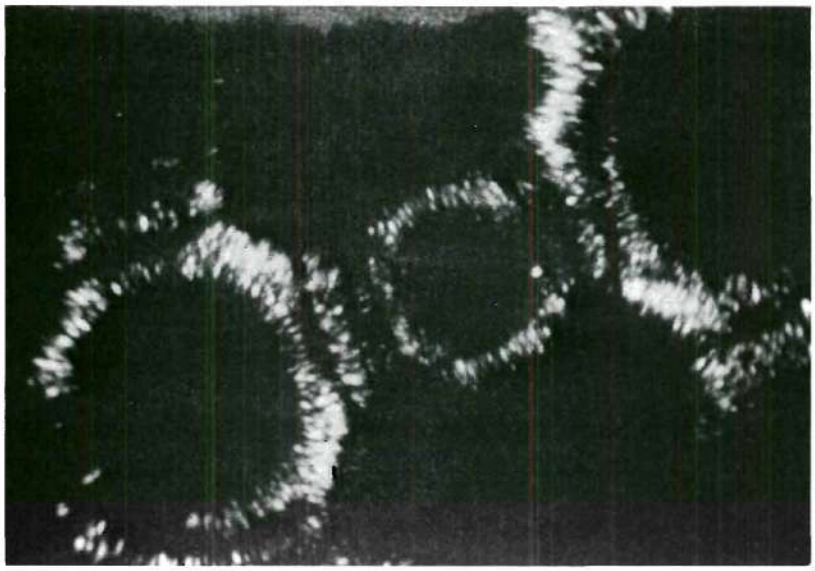

(a)

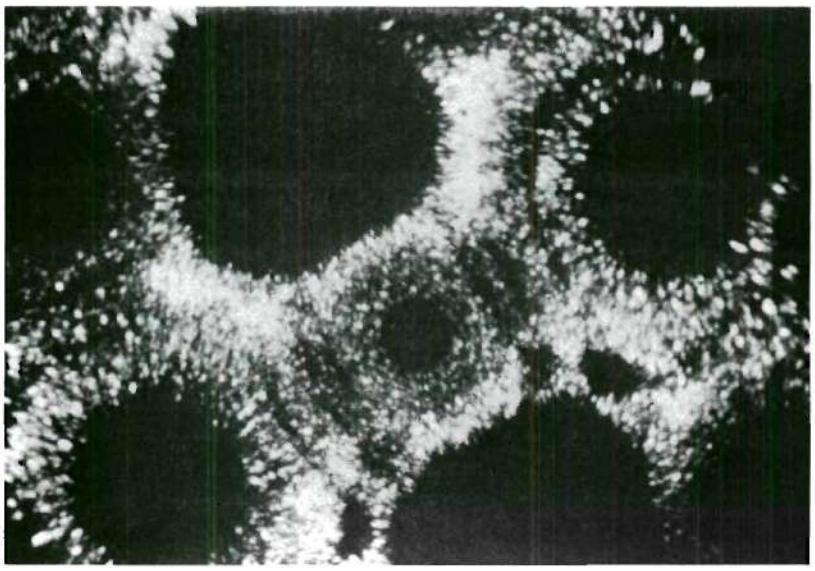

(b)

Figure 22. Iron after Vacuum Annealing at 710°K for 10 Minutes: (a) 9.5 KV (b) 10.8 KV.

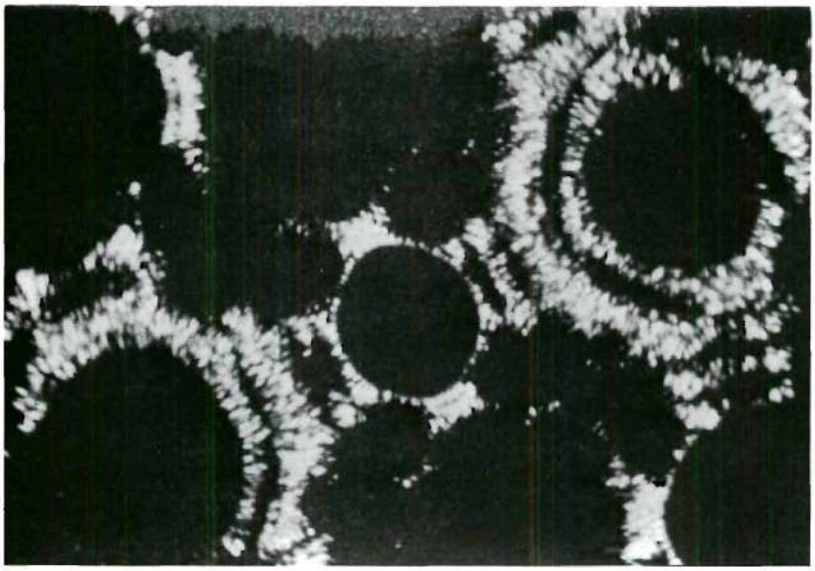

(a)

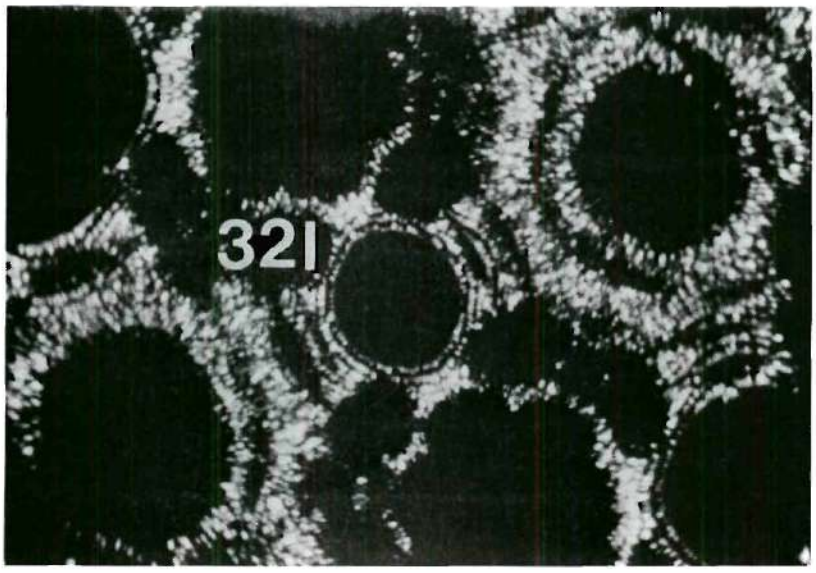

(b)

Figure 23. Iron after Vacuum Annealing at 725°K for 3 Minutes: (a) 12.0 KV (b) 12.8 KV

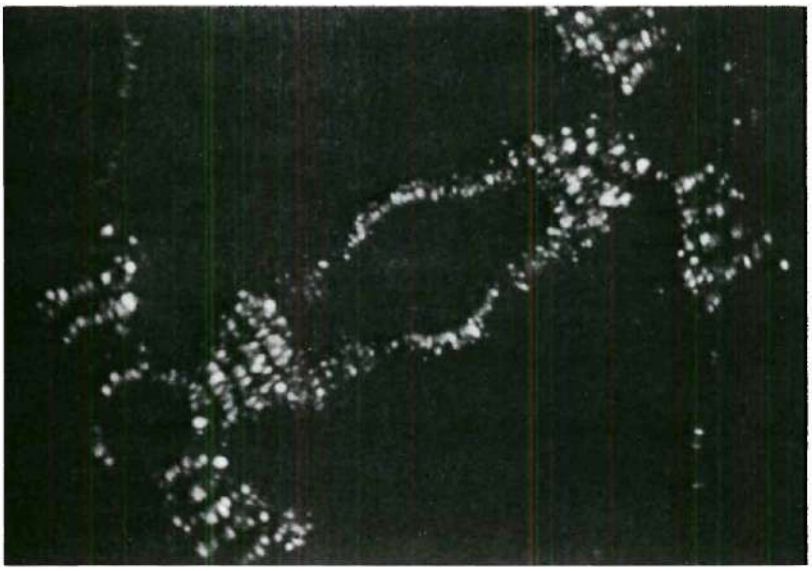

(a)

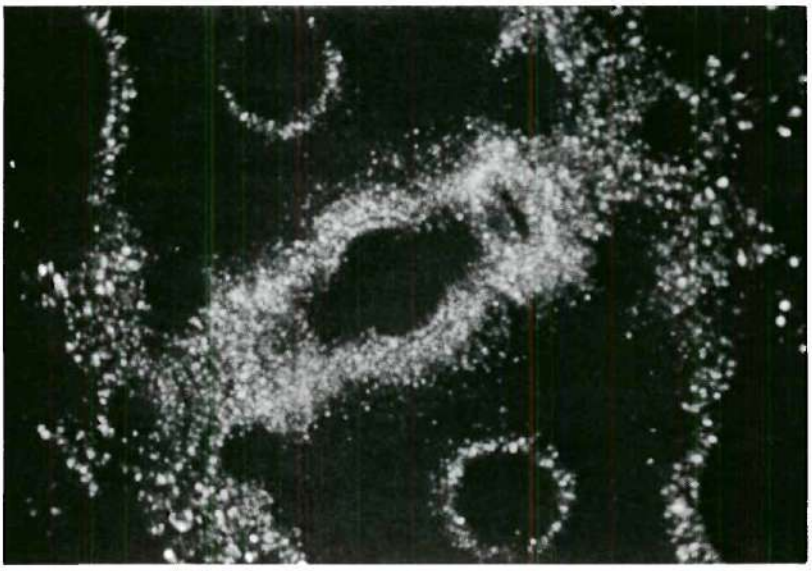

(b)

Figure 24. Iron after Vacuum Annealing at 880°K for 3 Minutes: (a) 13.0 KV (b) 14.5 KV.

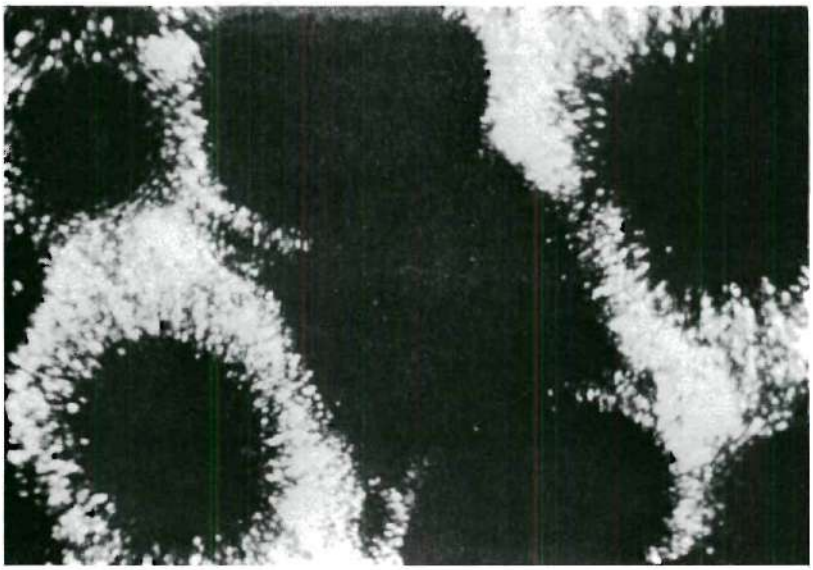

(a)

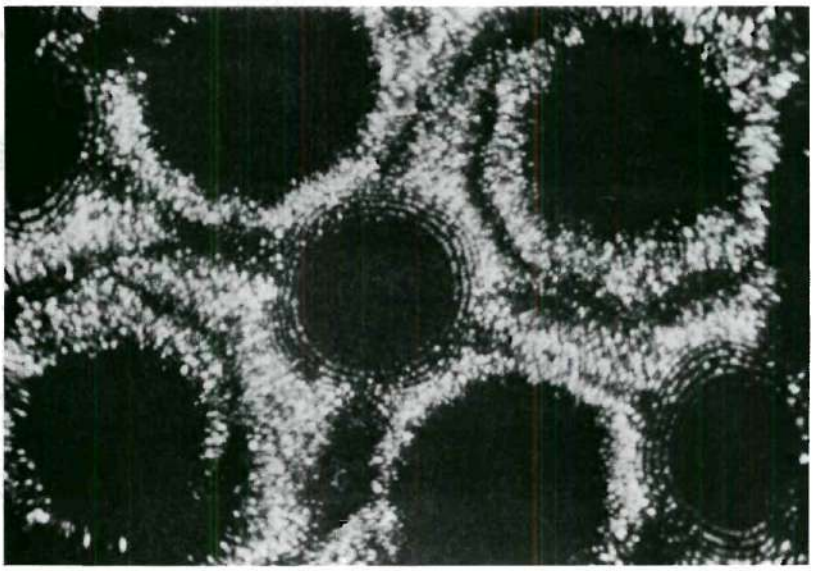

(b)

Figure 25. Iron after Hydrogen Annealing: (a) at 710°K for 10 Minutes - 12.0 KV (b) at 725°K for 3 Minutes - 13.0 KV.

a. In Vacuum. Iron specimens were observed after vacuum annealing at the following absolute temperatures (the time, in minutes, is given in parentheses): 650(5), 710(10), 725(3), 770(5), 880(3), 970(5), and 1000(2).

The end form after annealing at 650°K revealed only (111) facets. Images of the end forms at 710 and 725°K, as shown in Figures 22 and 23, respectively, revealed the order of decreasing facet size as follows: (111), (100) and (110). The sizes of (110) and (100) facets were taken from the micrographs in Figures 22(a) and 23(a) prior to any field evaporation from these planes while the (111) facet size was measured on micrographs in Figures 22(b) and 23(b). Facets of (321) planes were also observed after annealing at 725°K, as shown in Figure 23(b). The (211) regions appeared darker on the end form at 725°K, but did not reveal distinct facets. A few multiatomic surface steps were also seen near (110) and (100) regions. The end form at 770°K was similar to the end forms at 710 and 725°K.

The end form obtained after annealing at 880°K for 3 minutes, as shown in Figure 24, revealed the order of decreasing facet size as follows: (110), (211), (100), and (111). The sizes of (110) and (100) facets were obtained from the micrograph in Figure 24(a) prior to any evaporation from these planes. The sizes of (211) and (111) facets were taken after some field evaporation to reveal these facets, as shown in Figure 24(b). The former photograph revealed multiatomic surface steps in the (110) and (100) regions. The end form obtained after annealing at 970°K was essentially the same as that at 880°K except that the facet sizes were approximately 6% larger.

Evidence of specimen blunting was observed at 970°K and the extent of blunting became appreciable when the specimen was annealed at 1000°K.

b. In Hydrogen. Iron specimens were annealed in hydrogen at a pressure of 5×10^{-3} torr at the following absolute temperatures (time, in minutes, in parentheses): 710(10) and 725(3). The hydrogen coverage was calculated (Appendix B), using a heat of desorption for hydrogen of 32 k cal/mole[67], and monolayer of hydrogen was found to be present.

Specimens annealed in hydrogen at 710°K, as shown in Figure 25(a), revealed much larger (110) facets than those annealed in vacuum at this temperature. The order of decreasing facet size was (110), (111) and (100). The size of the (111) facet was comparable to the one obtained after annealing in vacuum, but the (100) facet size was larger than the corresponding size in vacuum. The end form obtained after annealing in hydrogen at 725°K, as shown in Figure 25(b), revealed the same order of facets. The size of each facet was in this case smaller than that after annealing in hydrogen at 710°K, but larger than that after annealing in vacuum at 725°K.

2. Surface Energy Anisotropy

a. In Vacuum. For specimens annealed in vacuum at 710, 725 and 770°K the surface energy of (111) appeared to be lower than that of (110) or (100) planes. This is contradictory to theoretical surface energy calculations (see Section II-A-1). The end forms at 880 and 970°K did contain the proper order of true facet sizes, and the facet sizes after annealing at 880°K were approximately the same as those after annealing at 970°K, therefore, the latter end form was assumed to be close to equilibrium and was used in calculating the surface energy anisotropy.

The true facet sizes were determined by multiplying the measured facet sizes from the micrographs times the appropriate correction terms (see Section II-C-1c). For the (110), (100), (211) and (111) regions, respectively, the local radii of curvature were found to be 1560,1155, 910 and 820* Å, and the magnification terms, M_o/M_r were 1.39, 1.14, 0.97 and 0.91. The contraction term, M_o/M_k was calculated from a partially field evaporated end form after thermal faceting and was found to be 1.07.

The true facet sizes were then used to calculate the surface energy anisotropies (see SectionIII-C-1a). The results of these calculations are given in Table 11. The maximum surface energy anisotropy, λ_{max}, was calculated from the true size of the (110) facet.

b. In Hydrogen. Comparisons of the measured angular widths of the facets formed in hydrogen and in vacuum at 710 and 725°K after 10 and 3 minutes, respectively, are given in Table 12. It is seen from the table that the facets formed in hydrogen were larger than those formed in vacuum.

The maximum surface energy anisotropies, λ_{max}, calculated from the true facet sizes of (110) planes, were as follows: at 710°K, 1.206 and 1.046 in hydrogen and in vacuum, respectively, and at 725°K, 1.075 and 1.050 in hydrogen and in vacuum, respectively.

D. Platinum

1. Thermally Faceted End Forms.

Platinum specimens imaged at 78°K in helium had very poor resolution. A lower temperature of 40-50°K, attained by flowing cold helium

*The local radius of (111) region was estimated from the ratio of best imaging voltage of (111) region to that of the whole specimen.

Table 11. Surface Energy Anisotropy of Iron at 970°K

Plane hkl	Measured Facet Size (in degrees)	Correction Term $M_o/M_r \times M_o/M_k$	True Facet Size (in degrees)	Anisotropy λ_{hkl}
(110)	27.27	1.488	40.58	1.000
(100)	17.63	1.220	21.51	1.048
(211)	19.79	1.038	20.24	1.050
(111)	16.70	0.970	16.20	1.058
λ_{max}	-	-	-	1.066

Table 12. Angular Widths of Various Facets on the Iron End Forms After Annealing at (a) 710°K for 10 Minutes (b) 725°K for 3 Minutes

Plane hkl	(a) 710°K In Hydrogen (in degrees)	(a) 710°K In Vacuum (in degrees)	(b) 725°K In Hydrogen (in degrees)	(b) 725°K In Vacuum (in degrees)
(110)	46.9	22.9	28.9	23.7
(100)	38.2	27.8	37.8	30.1
(111)	44.7	40.4	37.2	30.7

gas through the specimen holder dewar, greatly improved the resolution and was therefore used to field evaporate and image the platinum specimens. A typical micrograph of the specimen, which had been flash cleaned at nearly 1500°K, field evaporated to a nearly hemispherical end form and then imaged in helium at approximately 40°K, is shown in Figure 26.

The specimen was annealed at the following absolute temperatures (time, in minutes, in parentheses): in vacuum, 930(10), 1030(5), 1170(5) and 1240(4); in 10^{-4} torr helium, 985(15); in 2.7×10^{-3} torr hydrogen, 1030(3). The hydrogen coverage was calculated (Appendix B) and found to be 0.015, using a heat of desorption for hydrogen of 32 k cal/mole.[67] Typical micrographs of the annealed specimens are shown in Figure 27.

The end form after annealing in vacuum for 10 minutes at 930°K revealed multiatomic surface steps in (111), (100) and (110) regions. Annealing in helium for 15 minutes at 985°K produced only (111) and (100) facets, while annealing at 1030°K in vacuum produced facets in the following order of decreasing size: (111), (100), (110), (210) and (311). Two of the micrographs of the latter specimen are shown in Figures 27(a) and 27(b). The (111), (100) and (110) facet sizes were revealed at a lower specimen voltage (9.0 KV) than the (210) and (311) facets (10.1 KV). The size of (100) facets was estimated from the size of the half ring of (100) facets. The best image voltages changed appreciably after annealing at 1170 and 1240°K, presumably due to specimen blunting.

The end form after annealing in hydrogen for 3 minutes at 1030°K revealed only small (111) facets, as shown in Figure 27(c), along with a few surface steps in (111) and (100) regions.

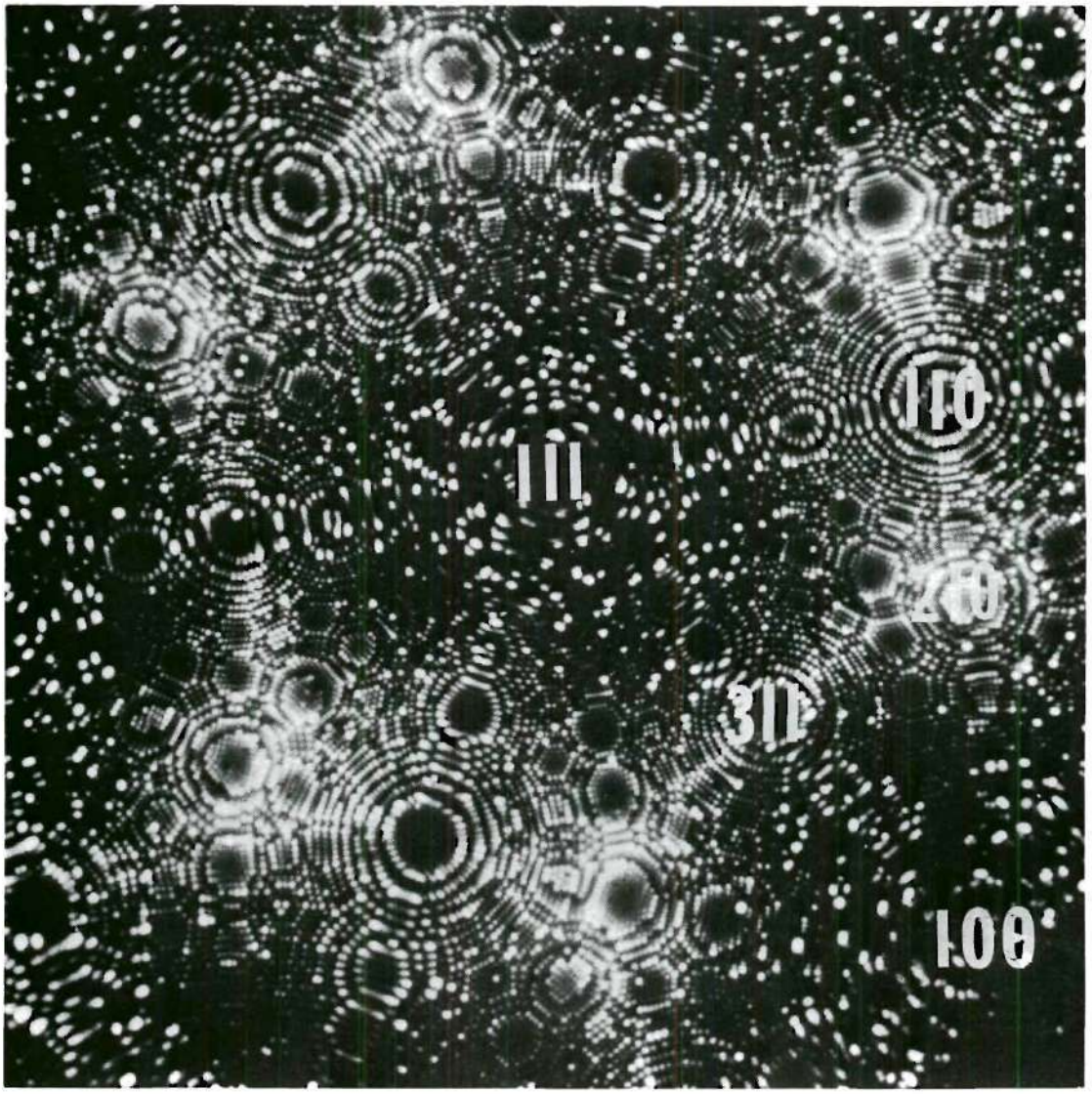

Figure 26. A Typical Field Evaporated Platinum Specimen - 15.0 KV.

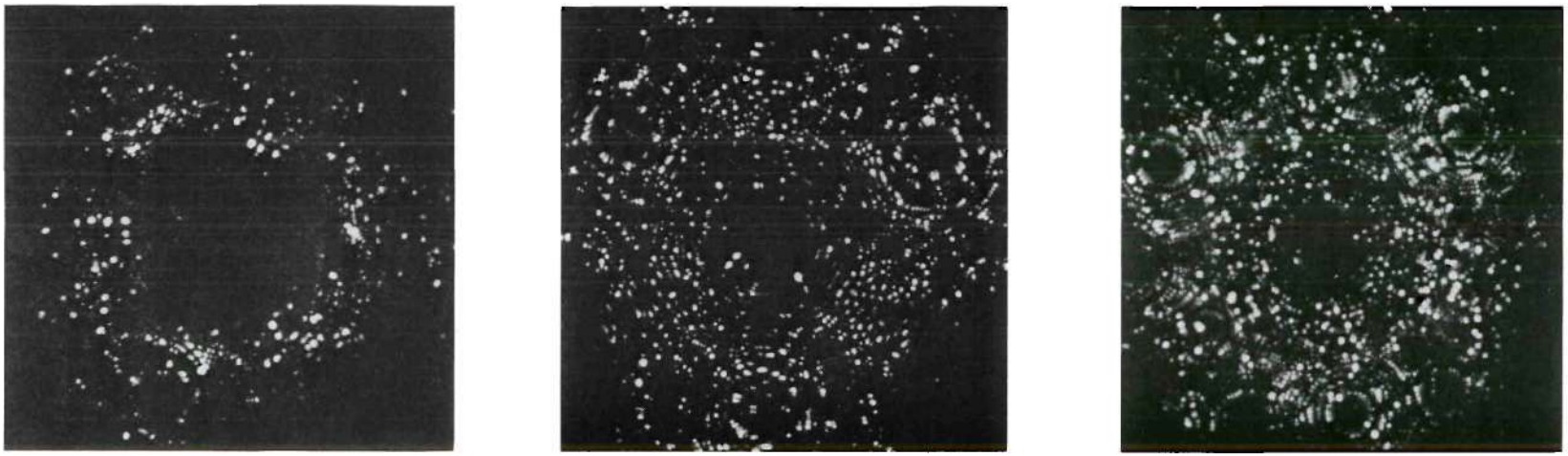

(a) (b) (c)

Figure 27. Platinum after Annealing at 1030°K: (a) in Vacuum for 5 Minutes - 9.0 KV (b) in Vacuum for 5 Minutes -10.1 KV (c) in Hydrogen for 3 Minutes - 10.4 KV.

2. Surface Energy Anisotropy

The surface energy anisotropy was calculated using the micrographs of the end form after annealing in vacuum at 1030°K, which showed the proper order of facets given by theoretical calculations (see Section II-A-1). The true facet sizes were obtained by multiplying the measured facet sizes on the micrographs times the appropriate correction terms (see Section II-C-1c). The local radii of curvature for (111), (100), (110), (311) and (210) regions on a field evaporated end form were 1125, 1020, 710, 745 and 460 Å, respectively, and the corresponding magnification terms, M_o/M_r were 1.255, 1.176, 0.925, 0.953 and 0.691. The contraction term, M_o/M_k was calculated from a partially field evaporated end form after thermal faceting and was found to be 1.378.

The true facet sizes were then used to calculate the surface energy anisotropy (see Section III-C-1a). The results of these calculations are given in Table 13. The maximum surface energy anisotropy, λ_{max}, was calculated from the true size of the (111) facet.

No comparison was made between specimens annealed in vacuum and in hydrogen, because in the latter case, only a single experiment was performed and the annealing time was not the same as in the former case. The results, however, indicated that the effect of hydrogen on the faceting rate was not very pronounced.

Table 13. Surface Energy Anisotropy of Platinum at 1030°K

Plane hkl	Measured Facet Size (in degrees)	Correction Term M_o/M_r X M_c/M_k	True Facet Size (in degrees)	Anisotropy λ_{hkl}
(111)	35.95	1.729	62.17	1.000
(100)	33.24	1.621	53.86	1.041
(110)	14.25	1.275	18.16	1.153
(311)	7.46	1.313	9.80	1.163
(210)	12.55	0.952	11.95	1.161
λ_{max}	-	-	-	1.168

CHAPTER V

DISCUSSION

A. Effect of Annealing Conditions on Faceting

1. Annealing Temperature on Vacuum Annealed End Forms.

The vacuum annealed end forms of all metals investigated showed similar characteristic features when the results were divided into certain temperature ranges, expressed as fractions of the absolute melting point, T_m. These features are summarized and discussed below according to these temperature ranges.

a. Below $\sim T_m/4$. On these end forms no thermal facets were observed; however, the images generally appeared irregular or disordered in the high index regions. The annealing temperatures, for which no facets were observed, were 760, 780 and 650°K for iridium, tungsten and iron, respectively. These results are in good agreement with the earlier studies for iridium[3] and tungsten[16] for which no facets were observed below 738 and 750°K, respectively.

b. Between $\sim T_m/4$ and $\sim T_m/2$. On these end forms both surface steps of multiatomic height and thermal facets were observed.

Multiatomic surface steps were generally found in one or more of the low index regions. In some cases, e.g. iridium (110) and (100), the steps disappeared, but, in general, multiatomic steps around the lowest index region, e.g., iridium (111), remained even after annealing at temperatures close to $T_m/2$. Similar multiatomic steps have been

reported for iridium[3] and tungsten[16] annealed in the same temperature range.

In this temperature range, the order of decreasing facet size, in general, disagreed with the theoretical surface energy calculations (Section II-A-1). The unpredicted faceting of high index planes, e.g. $(210)_f$ and $(111)_b$ in FCC and BCC metals, respectively, indicated lower surface energies than expected for these planes.

These observations may be a result of the specimen geometry prior to thermal faceting. It was found, in these studies, that the local radii of curvature for various regions on the field evaporated end form varied considerably and the specimen was not actually hemispherical. The local radii of curvature of $(210)_f$ and $(111)_b$ regions were nearly half those of $(111)_f$ and $(110)_b$ regions, respectively. According to Mullins[4] the chemical potential for thermal migration of surface atoms is inversely proportional to the radius of curvature of the surface. Therefore, the smaller radii of the $(210)_f$ and $(111)_b$ may result in a higher chemical potential for migration in these regions and a higher initial faceting rate. As faceting proceeds, however, the radii of curvature in these regions increase and the faceting due to this 'geometrical' influence eventually ceases. The above explanation was further supported experimentally by observations of a flash heated iridium specimen, which revealed only (210) facets. The size of these facets was not very different from that of (210) facets observed after long annealing periods at temperatures in the range of 880 to 1170°K.

c. Above $\sim T_m/2$. After annealing at temperatures of $\sim T_m/2$, the end forms appeared to be close to equilibrium and representative of the surface energy anisotropy of the metals. These end forms were used for surface energy anisotropy calculations, which are discussed later.

Specimen blunting occurred at temperatures higher than $T_m/2$ and became significant after annealing for only a few seconds at temperatures close to 0.57 T_m approximately. These end forms were presumably representative of the surface energy anisotropy also, but could not be used to calculate the anisotropy because the local magnification was unknown, and quite often the specimen was too blunt to image below 30 KV. The vapor pressure of each of these metals at the observed blunting temperature was below 10^{-9} torr; therefore, it is doubtful that evaporation of the metal contributed to the blunting process.

2. Hydrogen Environment on Annealed End Forms

For tungsten, iridium and iron, the angular widths of facets after annealing in hydrogen were, in general, greater than those of facets formed in vacuum under the same annealing conditions. From the results given in Tables 6, 9, and 12, it is seen that the differences were smaller for iridium and tungsten than for iron.

A pronounced effect of hydrogen on the order of facet sizes of iridium and tungsten at temperatures much less than $T_m/2$, however, was observed. The order of decreasing facet size was different from that observed in vacuum at the same temperature and was the same as that observed in vacuum at temperatures close to $T_m/2$.

All these observations can be explained by the increased diffusion rate in the presence of hydrogen (Section II-B-3b). This causes larger facet sizes in hydrogen than those in vacuum, and an approach to equilibrium end forms at temperatures much less than $T_m/2$. The increase in diffusion rate is attributed to a decrease in activation energy for surface diffusion, which is directly related to the binding strength of metals. Since surface energy is directly related to the binding strength of surface atoms, therefore, the increased diffusion rate indicates a lowering in surface energy.

B. Surface Energy Anisotropy

It has previously been reported that the experimental surface energy anisotropies of FCC metals, nickel,[9] gold[12] and platinum,[37] agreed well with those predicted by the pairwise bonding theory, while the anisotropies of BCC metals,[10,50] tungsten, iron, molybdenum, vanadium, niobium and tantalum, agreed best with those predicted by Mie potential theory. In the discussion given below, the anisotropies found in the present studies are compared with theoretically calculated values based on the above theories and on the Morse potential theory. The effect of hydrogen on the surface energy anisotropy is also discussed.

1. In Vacuum

The experimental values of surface energy anisotropy for the metals investigated are summarized in Table 14. Theoretically calculated anisotropies, based on the three models presented in Section II-A-1, are also given in Table 14. The parameters a, m, n, σ_2 and σ_3, were selected to give the closest possible agreement with the experimental anisotropies.

Table 14. Comparison of Surface Energy Anisotropies of Metals with Theoretical Anisotropies.

	Experimental	Theoretical		
		Morse Potential	Mie Potential	Pairwise Bonding Theory
IRIDIUM, at 1360°K		a=4.5	m= 6,n=12	σ_2 =.4, σ_3=.2
(111)	1.000	1.000	1.000	1.000
(100)	1.047	1.019	1.032	1.050
(110)	1.070	1.079	1.080	1.076
(311)	1.078	-	-	1.109
(210)	1.081	-	-	1.103
λ_{max}	1.088	1.099	1.095	1.112
TUNGSTEN, at 1780°K		a=4.28(+1.5)	m=5,n=8(+1.5)	σ_2=.7, σ_3=.5
(110)	1.000	1.000	1.000	1.000
(100)	1.028	1.018	1.003	1.039
(211)	1.030	1.079	1.031	1.064
(310)	1.032	1.065	1.025	1.104
λ_{max}	1.043	1.120	1.043	1.117

(continued)

Table 14. (Continued)

	Experimental	Theoretical		
		Morse Potential	Mie Potential	Pairwise Bonding Theory
IRON, at 970°K		a=4.0	m=6,n=12	$\sigma_2=.7, \sigma_3=.4$
(110)	1.000	1.000	1.000	1.000
(100)	1.048	1.019	1.048	1.048
(211)	1.050	1.060	1.061	1.075
(111)	1.058	1.061	-	1.056
λ_{max}	1.066	1.071	1.086	1.127
PLATINUM, at 1030°K		a=5.0	m=6,n=12	$\sigma_2=.3, \sigma_3=0$
(111)	1.000	1.000	1.000	1.000
(100)	1.041	1.031	1.032	1.021
(110)	1.153	1.105	1.080	1.130
(311)	1.163	-	-	1.165
(210)	1.161	-	-	1.172
λ_{max}	1.168	1.122	1.095	1.172

In the case of iridium, the observed anisotropies are in qualitative agreement with those predicted by using each of the models, but the order and magnitude of the experimental anisotropies for (111), (100) and (110) planes fit best with the pairwise bonding model, taking $\sigma_2 = 0.4$ and $\sigma_3 = 0.2$. The experimental anisotropies of (311) and (210) planes are lower than the anisotropies given by any of the three models. It is possible that the effects of original specimen geometry, as discussed in Section V-A-1b, have not been overcome and that true equilibrium has not yet been established. This is also indicated by the fact that while the experimental anisotropies of the low index planes agreed well with the theoretical values, the maximum experimental anisotropy, 8.8%, was less than the theoretical value of 11.2%. Further growth of (111) and other low index facets, which occurred very slowly at this point in the experiment, should lead to a higher observed maximum anisotropy and eventually equilibrium. The maximum anisotropy reported by Brenner[3] at 1260°K was 4%, whereas in the present work this value was found to be nearly 8.8% at 1360°K. The results of the present studies, therefore, more closely represent equilibrium than those of previous studies.

In the case of tungsten, qualitative agreement is found with each of the theoretical models; however, the best fit is found with the Mie potential calculations, using m=5, n=8 and a 1.5% lattice expansion. The experimental anisotropy of (100) plane, however, is higher than that predicted by the Mie potential. The maximum experimental anisotropy of 4.3% is in good agreement with that predicted by the Mie potential. These results are in reasonable agreement with those of previous

studies,[50] in which a Mie potential with m=5, n=7 and a 1.5% lattice expansion was found to fit. However, the previously reported value of the (100) anisotropy agreed with the theoretical value more closely than that in the present study.

In the case of iron, qualitative agreement is again found with all the models, but the best fit is found with Mie potential calculations, using m=6 and n=12. The anisotropy value of the (111) plane, however, is lower than that predicted by the Mie potential. This again could be attributed to the effect of original specimen geometry, as discussed above for iridium (311) and (210) facets. Furthermore, the specimen may not have been fully equilibrated, as indicated by the experimental maximum anisotropy of 6.6% compared to the theoretical value of 8.6%, calculated with the Mie potential. The previous results on iron,[10] using field emission microscopy, were claimed to be in quantitative agreement with Mie potential calculations using m=5, n=7 or 8. The present results are in agreement with Mie potential calculations, but with m and n values of 6 and 12, respectively. Since the image resolution is poorer in field emission microscopy than that in field-ion microscopy, therefore, a higher degree of accuracy is expected in the present studies.

In the case of platinum, qualitative agreement is found with all the models; but the best fit is found with the pairwise bonding model taking $\sigma_2 = 0.3$ and $\sigma_3 = 0$. The experimental anisotropy for (210) planes is lower than that predicted by the pairwise bonding model, which may also be attributed to geometrical effects as discussed previously for iridium (311) and (210) facets. As in the previous cases, the

observed maximum anisotropy of 16.8% is less that the predicted value of 17.2%, and absolute equilibrium may not have been reached. Earlier studies on platinum,[37] using twin boundary grooving techniques, reported the maximum anisotropies as 13.3, 11.1, 10.4 and 7.8% at 1193,1353,1573 and 1773°K, respectively. By extrapolation of these results the maximum anisotropy at 1030°K should be approximately 16.2%, which is in good agreement with the experimental value of 16.8% found in the present study. However, the extrapolated anisotropy for (100) planes[37] is approximately 10.4%, which is more than twice the value of 4.1% observed in the present study.

2. In Hydrogen

In all cases studied, it was seen that the size of facets formed in hydrogen were larger than those formed in vacuum after annealing at the same temperature and time. This may be due to a lower surface energy and/or an increased diffusion rate. The surface diffusion rate of atoms on field emitters is directly related to the surface energy and exponentially related to the activation energy for diffusion, as shown in Section II-B-2. The activation energy for diffusion, on a given plane, is directly related to the metal-metal bond energies on that plane, and it is the sum of these bond energies that determines the surface energy of the plane. The surface energy of a plane effects both the pre-exponential and exponential factors in the diffusion equation. Although these two factors are partially compensating, a decrease in the surface energy would generally lead to a high rate of diffusion, due to the exponential relation. Therefore, the greater faceting rate of metals in hydrogen compared to vacuum, which is indicative of a

decrease in metal-metal bond energies, can also be interpreted as a lowering of the surface energy in hydrogen.

The effect of hydrogen on the faceting rate depended upon the metal being investigated and was less pronounced for iridium and tungsten than for iron. The maximum effect of hydrogen on the surface energy lowering can be expressed as $\Delta\gamma_L$, defined as

$$\Delta\gamma_L = \frac{\gamma_{cpp}^{vac} - \gamma_{cpp}^{H_2}}{\gamma_{cpp}^{vac}}$$

which is found from the relationship:

$$\Delta\gamma_L = \frac{\lambda_{max}^{H_2} - \lambda_{max}^{vac}}{\lambda_{max}^{H_2}}$$

where γ_{cpp}^{vac}, $\gamma_{cpp}^{H_2}$ = surface energies of the closest packed planes under similar annealing conditions in vacuum and in hydrogen, respectively, and

λ_{max}^{vac}, $\lambda_{max}^{H_2}$ = corresponding values of maximum surface energy anisotropy.

This value, $\Delta\gamma_L$, for iridium (111) and tungsten (110) was found to be approximately 1%. In the case of iron (110), however, the effect of hydrogen was very pronounced. The largest effect was observed at 710°K, for which $\Delta\gamma_L$ was estimated to be $\simeq$ 14%.

The larger interaction of hydrogen with iron compared to other metals can be interpreted in terms of the chemisorption of hydrogen on

iron, which is non-activated. The smaller d-character of metal-metal bonding in iron, compared to tungsten and iridium, results in a higher availability of d-orbitals for chemisorption and therefore stronger chemisorption bonds.[69] This in turn weakens the metal-metal bonding and lowers the surface energy more in the case of iron.

C. Facet Growth Rates and Activation Energies

1. Facet Growth Rates

For iridium (111) planes, $d-d_o$ and d were found to be proportional to $t^{0.36}$ and $t^{0.20}$, respectively. These values of the time exponent are in agreement with Brenner's results[3] of 0.33 and 0.20, respectively. Comparing the above values with the results of the model growth rate curves, given in Section IV-A-3b, the best fit between the two is found for $X_F = 0$. For this value of X_F and a specimen radius between 600 and 1300 Å, the time exponent values are 0.425 ± 0.015 and 0.21 in $d-d_o$ and d equations, respectively.

Similarly in the case of tungsten (110) planes, the measured values of the time exponents in $d-d_o$ and d equations, were 0.315 and 0.20 respectively. The calculated values of the exponent, based on the model (see Section IV-B-3b) with $X_F = 0$ and a specimen radius between 600 and 1300 Å, are 0.395 ± 0.015 and 0.215 ± 0.015, respectively, and are in close agreement with the experimental values.

For both iridium (111) and tungsten (110) planes the exponents, in the d equations, obtained by the model with $X_F = 0$ agree very well with the experimental values. However, a slightly high value for the time exponents in $d-d_o$ equations have been obtained by these calculations.

Some of the errors involved in the analyses of the exponents are as follows. The facet sizes are observed after heating the specimen for a predetermined time, t. This time, t, may not coincide with the critical time, t_c, the time at which all the atoms of the top plane have just migrated to the underlying planes. When $t < t_c$, the migration from the top plane would not have completed and a very small facet size of this plane would have appeared in the image. When $t > t_c$, which appeared most often to be the case, the migration would have started from the next plane and again a smaller facet size than the ideal one might have been observed. Therefore, if the annealing time is anything other than t_c, the observed facet size will be smaller than that at t_c and that of the corresponding ideal facet. The smaller facet size would shift the growth curves so as to decrease the observed values of the time exponent, and hence the observed growth rate would be slower than the ideal growth rates. Other possible errors in the analyses may be due to the assumptions on which the mathematical model was based, i.e., that X_F is a constant for all the planes and that it is greater than, or equal to, zero.

2. Activation Energies

a. For Iridium (111) Faceting. The activation energy, Q_s, of 45.7 k cal/mole for iridium (111) faceting found in this work and of the 45.0 k cal/mole reported earlier by Brenner[3] using field-ion microscopy, are in good agreement. These values are 0.3 times the heat of vaporization, ΔH_v, of iridium (ΔH_v = 152 k cal/mole). Bettler and Barnes[54] reported the Q_s value of 53 k cal/mole (0.35 ΔH_v) for iridium (111) planes, using field emission microscopy.

The previous studies[70,22] on surface diffusion of copper by thermal grooving techniques at temperatures between 0.8 and 0.99 T_m, where T_m is the absolute melting point of copper, reported Q_s to be 49[70] and 41 k cal/mole.[22] These values are 0.61 and 0.51, respectively, times ΔH_v (80 k cal/mole) of copper. Choi and Shewmon[70] explained their results (0.61 ΔH_v) on the basis that the rate controlling step was the migration of kink atoms (6 nearest neighbor bonds) to the saddle positions (2 nearest neighbor bonds). Since the heat of vaporization, ΔH_v, equals 6 ϕ_1, where ϕ_1 is the energy of the nearest neighbor bond, the activation energy for surface diffusion is 2 $\Delta H_v/3$. Gjostein[22] explained his results (0.51 ΔH_v) by proposing that the rate controlling step was the migration of kink atoms to the adatom positions (3 nearest neighbor bonds). This would predict the activation energy to be $\Delta H_v/2$.

Brenner[3] explained the FIM results on iridium on the basis that the controlling step was the migration of kink atoms to a position adjacent to the kink site with 4 nearest neighbor bonds. This process would require 2 bonds to be broken and the activation energy would be equal to $\Delta H_v/3$. In the present work the observed values agree with the mechanism presented by Brenner. It might be pointed out that a theoretical analysis, similar to the one given by Brenner and in addition considering second neighbor bond contributions would result in $\Delta H_v = 6\,\phi_1 + 3\,\phi_2$, and $Q_s = 2\,\phi_1 + \phi_2$, which is again equal to $\Delta H_v/3$. From this it appears that the second neighbor interactions do not affect the ratio, R, of $Q_s/\Delta H_v$ in the case of FCC metals.

Differences in the Q_s values obtained by FIM and thermal grooving (TG) techniques may be expected due to the following reasons. The FIM

specimens, with highly curved surfaces, have a higher ratio of kink to ledge atoms than do the macroscopic specimens in TG studies. In FIM studies the migration of a kink atom to a position adjacent to the kink site and then to other positions may be more likely because of the high density of kink atoms and the low temperatures ($< 0.5\ T_m$) used. The higher temperatures ($> 0.8\ T_m$) used in TG studies may cause migration not only from the low energy kink positions but also from the higher energy ledge sites, which are more abundant on these macroscopic specimens, and therefore may lead to a higher Q_s value than that observed when kink atoms migration alone is involved.

b. For Tungsten (110) Faceting. The activation energy of 54.5 k cal/mole for tungsten (110) faceting, found in this research, is 0.273 times the heat of vaporization of tungsten (200 k cal/mole). Earlier results[29,48,54-56,58] using FEM, for the Q_s values for tungsten were in the range of 62-74 k cal/mole, i.e., 0.31-0.37 times ΔH_v. Bassett[16] reported from his FIM studies that the values of Q_s were in the range of 41-53 k cal/mole, i.e., 0.21-0.265 times ΔH_v.

Barbour et. al.[29] explained their value of 72 k cal/mole on the basis that the potential energy of surface atoms is a function of location, and the activation energy is the difference between the potential energy of the saddle position and the minimum potential energy for the atom on the surface. This difference gives the minimum value for Q_s equal to 73.5 k cal/mole. Since the migration occurs over all orientations on field emission specimens, they[29] expected the theoretical values of Q_s to be 85 k cal/mole. The discrepancy, according to them, was explained by the fact that the calculated value corresponds to the

case of an isolated atom migrating over the surface of an ideal crystal, whereas in the experimental case the migration is facilitated by the fact that a large number of atoms participate at a given time, and furthermore experimental evidence indicates that Q_s is reduced by the presence of crystal imperfections.

The results of the present work and that of Bassett[16] can be explained on the basis of a similar mechanism as given for iridium (111) faceting. Considering first nearest neighbor contributions, the kink atom on the (110) plane has 4 nearest neighbors' bonds, i.e. $\Delta H_v = 4 \phi_1$. The detachment of the kink atom and migration to a position adjacent to the kink site with three nearest neighbors would require a Q_s of $\Delta H_v/4$.

If one considers the contributions of second neighbor bonds, then ΔH_v equals $4 \phi_1 + 3 \phi_2$ and Q_s equals $\phi_1 + \phi_2$. The ratio, R, of Q_s to ΔH_v would be given by:

$$R = \frac{1 + \sigma_2}{4 + 3 \sigma_2}$$

where $\sigma_2 = \phi_2 / \phi_1$.

It is seen from the above equation, that R is dependent on the value of σ_2. A plot of σ_2 versus R, as shown in Figure 28, gives the value of $\sigma_2 = 0.5$ for which R is equal to 0.273, the experimentally observed value in this research. Figure 28 indicates that the value of σ_2 has a significant effect on the activation energy for surface migration on BCC metals. Moreover, the present result that $\phi_2 = 0.5 \phi_1$ agrees very well with the earlier results reported by Stranski and Suhrmann[71],

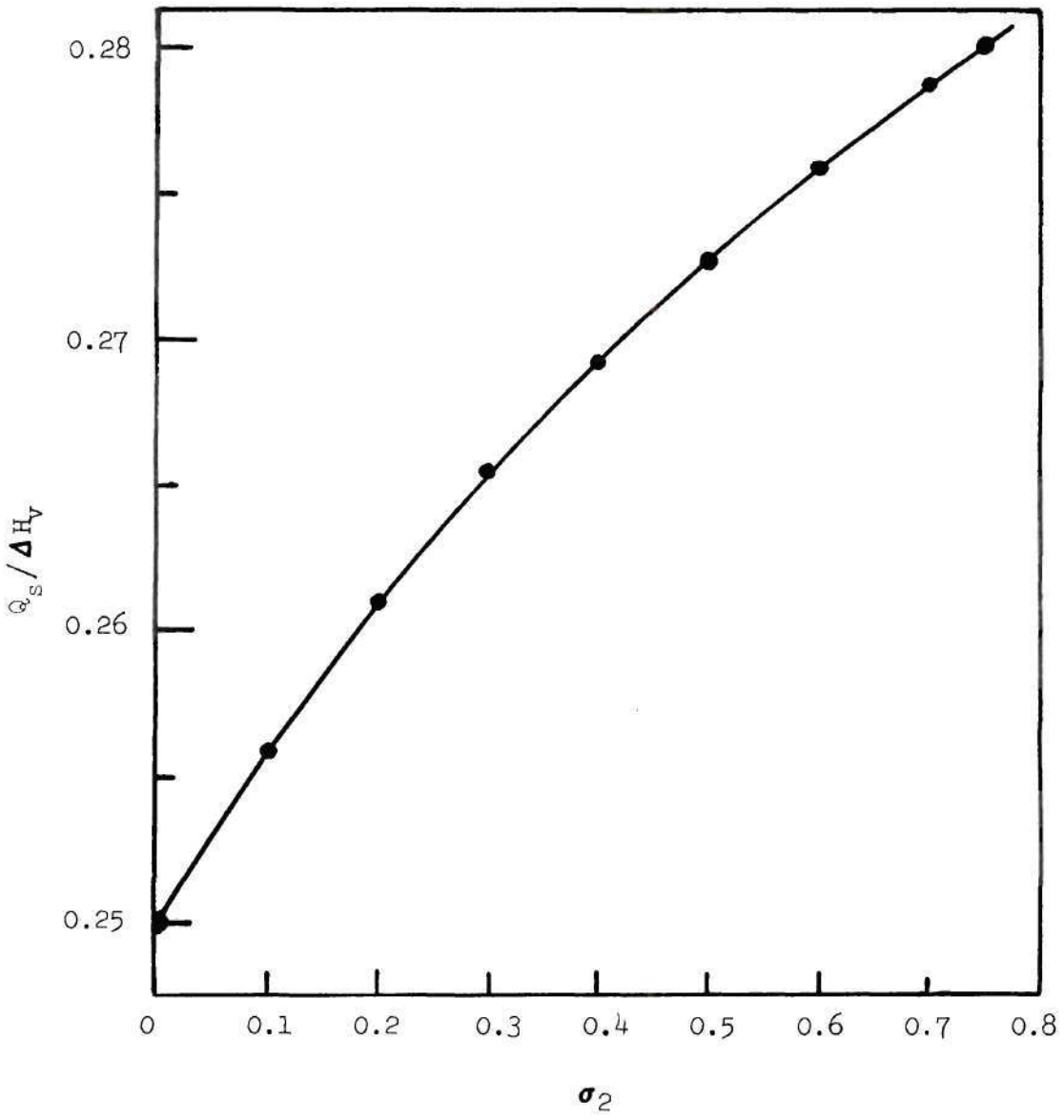

Figure 28. Dependence of $Q_s / \Delta H_v$ on σ_2 in BCC Crystals.

i.e. $\phi_2 = 0.5\ \phi_1$ and $\phi_3 < 0.05\ \phi_1$, on second and third neighbor bonds for BCC crystals.

In conclusion, the activation energy for faceting on field-ion specimens agrees with a model in which the kink atoms detach and migrate to the adjacent positions on the kink atoms and then migrate away from this position to the underlying planes.

CHAPTER VI

CONCLUSIONS AND RECOMMENDATIONS

A. Conclusions

1) Field-ion microscope can be used to study the equilibrium shapes of small crystals.

2) The surface energy anisotropy, that is the ratio of the surface energy of the (hkl) plane to that of the closest packed plane for each metal studied is as follows:

Iridium at 1360°K;

(111)	(100)	(110)	(311)	(210)	(λ_{max})
1.000	1.047	1.070	1.078	1.081	1.088

Tungsten at 1780°K;

(110)	(100)	(211)	(310)	(λ_{max})
1.000	1.028	1.030	1.032	1.043

Iron at 970°K;

(110)	(100)	(211)	(111)	(λ_{max})
1.000	1.048	1.050	1.058	1.066

Platinum at 1030°K;

(111)	(100)	(110)	(311)	(210)	(λ_{max})
1.000	1.041	1.153	1.163	1.161	1.168

3) The experimental anisotropies for iridium and platinum is in agreement with the predictions of pairwise bonding theory with $\sigma_2 = 0.4$,

$\sigma_3 = 0.2$ and $\sigma_2 = 0.3$, $\sigma_3 = 0$, respectively.

4) The experimental anisotropies for tungsten and iron are in agreement with Mie predictions with m=5, n=8 (+1.5) and m=6, n=12, respectively.

5) The presence of hydrogen increases the rates of surface diffusion and growth of facets.

6) The increased surface diffusion rate in hydrogen can be expressed as a weakening of the metal-metal bond strength and corresponds to an approximately 1% decrease in the surface energies of iridium (111) and tungsten (110) planes and an approximately 14% decrease in the surface energy of iron (110) planes.

7) The observed changes in facet size of iridium (111) and tungsten (110) planes is proportional to $t^{0.36}$ and $t^{0.315}$, respectively, where t is the time of annealing. The corresponding facet sizes, d, are both proportional to approximately $t^{0.20}$.

8) From computer simulations of the $d-d_o$ and d versus time curves based on a surface diffusion model, agreement is found with the experimental growth rate when the net fraction of available migrating atoms attached to underlying planes is equal to zero.

9) The observed activation energies for facet growth on iridium (111) and tungsten (110), respectively, planes were 45.7 and 54.5 k cal/mole, which are approximately 0.3 and 0.273 times the corresponding heats of vaporization.

10) The activation energies for faceting agree with a model in which the rate controlling step is the migration of kink atoms.

B. Recommendations

The following studies are recommended to extend the present investigation on surface energy anisotropy of metals in vacuum or in preselected environment and to understand atomically the diffusion mechanism on field emitters.

1) The surface energy anisotropy of other transition metals should be determined to evaluate the surface energy models.

2) The effect of hydrogen on the surface energy and surface diffusion of industrially important metals and alloys should be investigated.

3) The mechanism of hydrogen embrittlement should be investigated in terms of the effect of hydrogen on the surface energy. For example, the 14% lowering of the surface energy of iron (110) planes may be related to the hydrogen embrittlement of ferrous materials.

4) The model for facet growth, presented in this investigation, should be further modified to account for the initial surface steps observed on annealed specimens and for the variation of the fraction attached with the size of the underlying plane.

5) The activation energy for surface diffusion should be further studied by this technique to further elucidate the mechanism of surface diffusion on field emitters.

APPENDIX A

RESISTIVITY OF TUNGSTEN AT VARIOUS TEMPERATURES

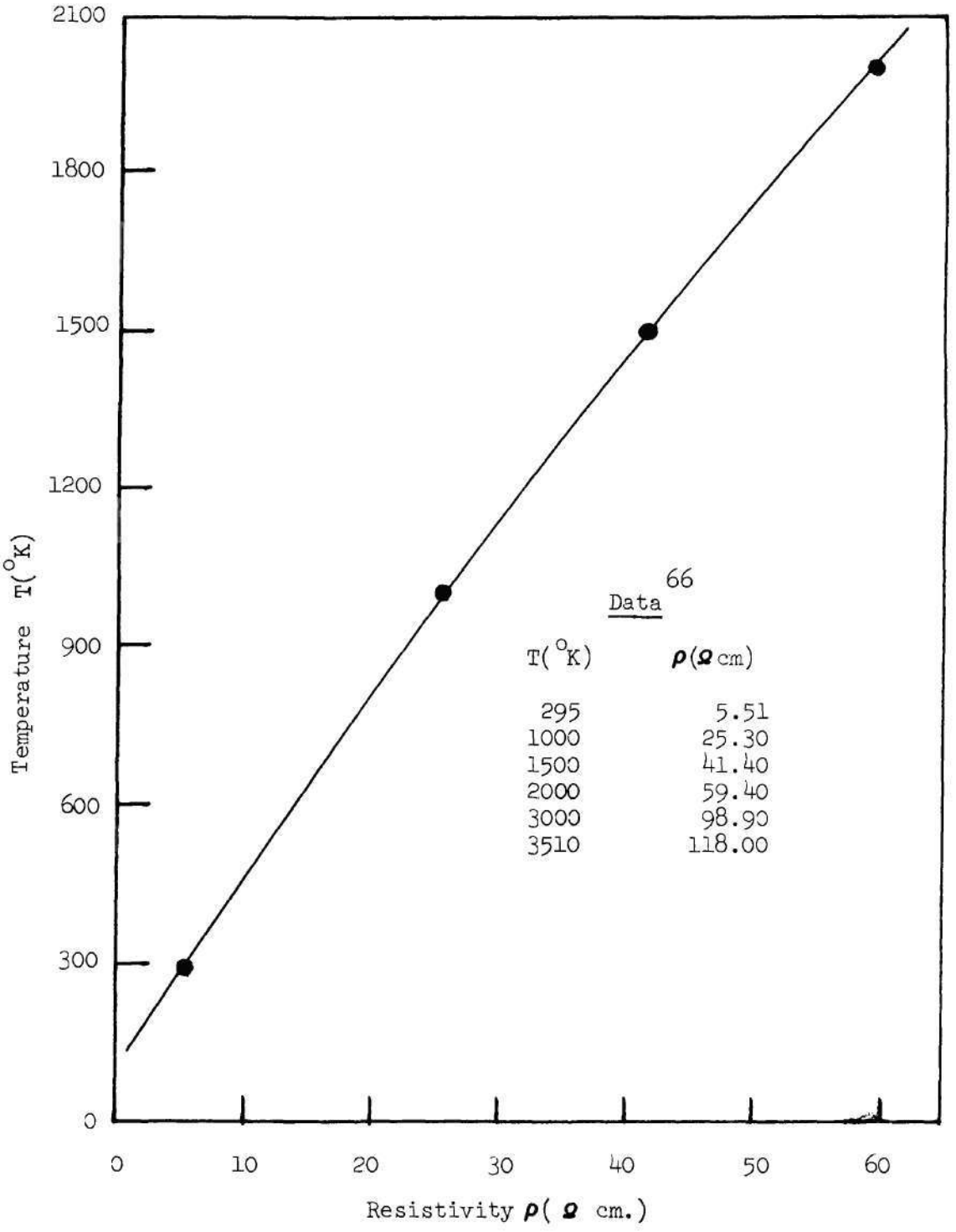

APPENDIX B

METHOD TO CALCULATE HYDROGEN COVERAGE ON A METAL SURFACE

The activation energy for desorption is related to the desorption rate of gas atoms from the surface at a particular temperature for first order desorption kinetics according to the following equation:[68]

$$dn/dt = \nu_o n \exp(-E_d/RT)$$

where dn/dt = desorption rate,

n = number of surface atoms,

ν_o = pre-exponential term related to vibrational frequency,

E_d = activation energy for desorption,

R = gas constant, and

T = absolute temperature

The integrated form of the above equation gives the following expression for the stability time, t, of gas molecules or atoms on the metal surface:

$$t = (1/A) \exp(E_d/RT)$$

where

$$A = \frac{\nu_o}{\log_e n} \simeq 10^{13}/\text{sec.}$$

From the known E_d for hydrogen on a given metal, the stability time, t_T, at a given temperature, T, for hydrogen on the surface can be found. It has been shown that a monolayer of gas is formed on a surface in one second at a pressure of 10^{-7} torr, assuming a sticking coefficient of unity. That is, at 10^{-7} torr enough molecules to cover the surface collide with the surface every second. If the stability time is less than one second, the pressure or the number of collisions must be increased proportionately to maintain a monolayer. Therefore, the pressure required, p_T, to maintain a monolayer at the given temperature, T, when the stability time is t_T is given by:

$$p_T = 10^{-7} / t_T.$$

The surface coverage during the experiment is then the ratio of the hydrogen pressure in the system to the theoretical pressure, p_T, required for a monolayer at that temperature. While the calculated coverage was much greater than one in several cases, the chemisorbed layer is generally assumed to be no greater than monolayer in coverage.

APPENDIX C

GENERAL PROGRAM TO CALCULATE FACET SIZE VERSUS TIME

```
Card
No.                                  Program
 1          DIMENSIØN AP(25,25),BP(25,25),SAP(20),SBP(20),APS(20),
 2         1BPS(20),DAP(20),LSA(20),LSB(20),LAP(20),LBP(20),LDA(20),
           LDB(20), DBP(20)
 3      C   PRØGRAM FØR CALCULATING FACET GRØWTH RATE FØR IRIDIUM
 4      C   (111) AND TUNGSTEN (110) PLANES
 5      C   TERMS WITH 'A' ARE FØR IRIDIUM AND 'B' FØR TUNGSTEN
 6      C   APS=FACET DIAMETER, DAP= CHANGE IN FACET DIAMETER
 7      C   XF=FRACTION ATTACHED,RA=SPECIMEN RADIUS(Å),SAP=FACET TIME
 8          IMPLICIT REAL (L)
 9          NP=20
10          PI=4. * ATAN (1.)
11          A=3.8389
12          B=3.1648
13          SAP(1)=1.
14          SBP(1)=1.
15          AD=A/SQRT(3.)
16          BD=B/SQRT(2.)
17          YA=SQRT(6.)* PI/(A**2)
18          YB=SQRT(2.)* PI/(B**2)
19          DØ 70 NF=1,11
```

```
20          XF=NF/20. -0.05
21          R=600
22      10  DØ 5 I=1,NP
23          J=1
24          RA=R
25          RB=R
26          AP(I,1)=YA*(R**2-(R+1.*AD/4.-I*AD)**2)
27          BP(I,1)=YB*(R**2-(R+1.*BD/4.-I*BD)**2)
28          APS(1)=SQRT(AP(1,J))
29          BPS(1)=SQRT(BP(1,J))
30       5  CØNTINUE
31      50  J=J+1
32          K=J-1
33          N=K
34          DØ 35 I=1,NP
35          IF(I-J) 40,55,45
36      40  AP(I,J)=0
37          BP(I,J)=0
38          GØ TØ 35
39      55  AP(I,J)=AP(I,K)+AP(N,K)*XF*(1-XF)**(I-J)
40          BP(I,J)=BP(I,K)+BP(N,K)*XF*(1-XF)**(I-J)
41          M=I-1
42          SAP(I)=SAP(M)+AP(N,K)
43          SBP(I)-SBP(M)+BP(N,K)
44          LSA(I)=ALØG10(SAP(I))
```

```
45          LSB(I)=ALØG10(SBP(I))
46          APS(I)=SQRT(AP(I,J))
47          BPS(I)=SQRT(BP(I,J))
48          LAP(I)=ALØG10(APS(I))
49          LBP(I)=ALØG10(BPS(I))
50          DAP(I)=APS(I)-APS(1)
51          DBP(I)=BPS(I)-BPS(1)
52          LDA(I)=ALØG10(DAP(I))
53          LDB(I)=ALØG10(DBP(I))
54          GØ TØ 35
55       45 AP(I,J)=AP(I,K)+AP(N,K)*XF*(1-XF)**(I-J)
56          BP(I,J)=BP(I,K)+BP(N,K)*XF*(1-XF)**(I-J)
57       35 CØNTINUE
58          IF(J.EQ.NP) GØ TØ 60
59          GØ TØ 50
60       60 WRITE(6,65)RA
61          WRITE(6,15)XF
62          WRITE(6,30)(SAP(I),APS(I),DAP(I),LSA(I),LAP(I),LDA(I),
            I=1,NP)
63          WRITE(6,75)RB
64          WRITE(6,15)XF
65          WRITE(6,30)(SBP(I),BPS(I),DBP(I),LSB(I),LBP(I),LDB(I),
            I=1,NP)
66       65 FØRMAT (////,1X,4HRA=  ,1X,F10.4)
67       75 FØRMAT (////,1X,4HRB=  ,1X,F10.4)
68       15 FØRMAT (/,1X,4HXF=  ,1X,F10.6)
```

```
69        30  FØRMAT (/ 3E11.5,10X,3F10.4)
70            R=R+100
71            IF(R.GT.1300.) GØ TØ 70
72            GØ TØ 10
73        70  CØNTINUE
74            STØP
```

1. Computer Results for Growth Parameters of Iridium (111) Planes

RA=800.0
XF=0.100

t/K_t	d/K_f	$d-d_1/K_f$	log t/K_t	log d/K_f	log $d-d_1/K_f$
.10000+01	.37247+02	.00000	.0000	.0000	.0000
.13884+04	.58064+02	.20817+02	3.1425	1.7639	1.3184
.47598+04	.74397+02	.37149+02	3.6776	1.8716	1.5700
.10295+05	.88754+02	.51506+02	4.0126	1.9482	1.7119
.18172+05	.10197+03	.64723+02	4.2594	2.0085	1.8111
.28570+05	.11444+03	.77193+02	4.4559	2.0586	1.8876
.41666+05	.12638+03	.89135+02	4.6198	2.1017	1.9500
.57639+05	.13793+03	.10068+03	4.7607	2.1397	2.0030
.76664+05	.14918+03	.11193+03	4.8846	2.1737	2.0490
.98918+05	.16018+03	.12294+03	4.9953	2.2046	2.0897
.12458+06	.17100+03	.13375+03	5.0954	2.2330	2.1263
.15382+06	.18164+03	.14440+03	5.1870	2.2592	2.1596
.18681+06	.19216+03	.15491+03	5.2714	2.2837	2.1901
.22373+06	.20255+03	.16530+03	5.3497	2.3065	2.2183
.26476+06	.21284+03	.17560+03	5.4229	2.3281	2.2445
.31006+06	.22305+03	.18580+03	5.4915	2.3484	2.2691
.35982+06	.23318+03	.19593+03	5.5561	2.3677	2.2921
.41419+06	.24324+03	.20599+03	5.6172	2.3860	2.3139
.47336+06	.25324+03	.21599+03	5.6752	2.4035	2.3344
.53749+06	.26318+03	.22594+03	5.7304	2.4203	2.3540

2. Computer Results for Growth Parameters of Tungsten (110) Planes

RB=800.0
XF=0.10

t/K_t	d/K_f	$d-d_1/K_f$	log t/K_t	log d/K_f	log $d-d_1/K_f$
.10000+01	.34496+02	.00000	.0000	.0000	.0000
.11910+04	.53774+02	.19278+02	3.0759	1.7306	1.2851
.40826+04	.68900+02	.34404+02	3.6109	1.8382	1.5366
.88298+04	.82196+02	.47700+02	3.9460	1.9148	1.6785
.15586+05	.94435+02	.59939+02	4.1927	1.9751	1.7777
.24504+05	.10598+03	.71487+02	4.3892	2.0252	1.8542
.35736+05	.11704+03	.82546+02	4.5531	2.0683	1.9167
.49435+05	.12774+03	.93241+02	4.6940	2.1063	1.9696
.65752+05	.13815+03	.10366+03	4.8179	2.1404	2.0156
.84838+05	.14834+03	.11385+03	4.9286	2.1713	2.0563
.10684+06	.15835+03	.12386+03	5.0287	2.1996	2.0929
.13192+06	.16821+03	.13372+03	5.1203	2.2259	2.1262
.16022+06	.17795+03	.14345+03	5.2047	2.2503	2.1567
.19188+06	.18757+03	.15308+03	5.2830	2.2732	2.1849
.22706+06	.19711+03	.16261+03	5.3561	2.2947	2.2111
.26592+06	.20656+03	.17206+03	5.4247	2.3150	2.2357
.30858+06	.21593+03	.18144+03	5.4894	2.3343	2.2587
.35521+06	.22525+03	.19075+03	5.5505	2.3527	2.2805
.40595+06	.23451+03	.20001+03	5.6085	2.3702	2.3011
.46094+06	.24371+03	.20922+03	5.6636	2.3869	2.3206

APPENDIX D

CALCOMP PLOTTER PROGRAMS FOR FACETING ON IRIDIUM (111) AND TUNGSTEN (110) PLANES

Card No.	Program
1	DIMENSIØN AP(25,25),BP(25,25),SAP(20),SBP(20),APS(20),
2	1BPS(20),DAP(20),DBP(20),LSA(20),LSB(20),LAP(20),LBP(20),
3	1LDA(20),LDB(20),C(200),V(200),IBUF(5000)
4	C TUNGSTEN (110) FACET SIZE FØR VARIØUS XF VALUES
5	NN=19
6	V(NN+2)=1000.
7	C(NN+2)=10.
8	V(NN+3)=0.5
9	C(NN+3)=0.25
10	CALL PLØTS (IBUF(1),5000,2)
11	CALL LGAXIS(0.0,0.0,20H TIME , -20,
12	18.0,0.0,V(NN+2),V(NN+3))
13	CALL LGAXIS(0.0,0.0,20H FACET SIZE , 20,
14	18.0,90.0,C(NN+2),C(NN+3))
15 - 27	Cards from General Program (Appendix C) 8 - 20
28	R = 800.
29 - 66	Cards from General Program(Appendix C) 22 - 59
67	60 WRITE (6,75) RB
68 - 72	Cards from General Program (Appendix C) 64-65, 67-69

```
      DØ  6  I=1,NP
      V(I)=SBP(I)
      C(I)=BPS(I)
    6 CØNTINUE
      CALL LGLINE (V(2),C(2),NN,1,0,0,0)
   70 CØNTINUE
      CALL PLØT (3.3,3.3,999)
      END
```

BIBLIOGRAPHY

1. C. Herring, in Structure and Properties of Solid Surfaces, Edited by R. Gomer and C. S. Smith, University of Chicago Press (1953)5.

2. J. Boling and W. W. Dolan, J. Appl. Phys. 29 (1958) 556.

3. S. S. Brenner, Surf. Sci. 2 (1964) 496.

4. W. W. Mullins, In Metal Surfaces, Structure, Energetics and Kinetics, ASM Seminar (1962) 17.

5. J. K. Mackenzie, A. J. W. Moore and J. F. Nicholas, J. Phys. Chem. Solids 23 (1962) 185.

6. A. Ponslet and D. Bariaux, in Society of Chemical Industries, monograph no. 28, (1968) 80.

7. P. Adam and H. Wever, Surf. Sci. 21 (1970) 307.

8. M. McLean and B. Gale, Phil. Mag. 20 no. 167 (1969) 1033.

9. H. Mykura, Acta Met. 9 (1961) 570.

10. M. Drechsler and J. F. Nicholas, J. Phys. Chem. Solids 28 (1967) 2609.

11. H. Sang and W. A. Miller, Surf. Sci. 28 (1971) 349.

12. W. L. Winterbottom and N. A. Gjostein, Acta Met. 14 (1966) 1041.

13. C. Herring, Phys. Rev. 82 (1951) 87.

14. G. Wulff, Z. Krist. 34 (1901) 449.

15. A. J. W. Moore, in Metal Surfaces Structure, Energetics and Kinetics, ASM Seminar (1962) 155.

16. D. W. Bassett, Proc. Roy. Soc. London 286 (1965)191.

17. P. G. Shewmon and W. M. Robertson, in Metal Surfaces, Structure, Energetics and Kinetics, ASM Seminar (1962) 67.

18. N.A.Gjostein, presented in the ASM Seminar on Diffusion, (Oct. 1972) Cleveland, Ohio.

19. J. W. Gibbs, in On the Equilibrium of Hetrogeneous Substances, collected works, Longmans, Green and Co., Vol. I., New York (1928).

20. J. M. Blakely, Prog. Mat. Sci. 10 (1963) 395.

21. G. Neumann and G. M. Neumann, in Surface Self Diffusion of Metals, Diffusion Monogram Series, Published by Diffusion Information Center, Bay Village, Ohio (1972).

22. N.A.Gjostein, Metal Surfaces, Structure, Energetics and Kinetics, ASM Seminar (1962) 99.

23. F.C. Frank, in Growth and Perfection of Crystals, Edited by Doremus et.al. (1958) 304.

24. C. Herring, J. Appl. Phys. 21 (1950) 301.

25. C. Herring, in Symposium on Physics of Powder Metallurgy, 1949, Edited by W. E. Kingston, McGraw Hill, N.Y. (1951).

26. W. W. Mullins, J. Appl.Phys. 28 (1957) 333.

27. W. W. Mullins, J. Appl. Phys. 30 (1959) 77.

28. W. W. Mullins, Trans. AIME 218 (1960) 354.

29. J. P. Barbour et al., Phys. Rev. 117 No. 6 (1960) 1452.

30. E. W. Müller, Z. Physik 126 (1949) 642.

31. A. J. Melmed, J. Appl. Phys. 37 (1966) 275.

32. M. McLean and J. P. Hirth, Surf. Sci. 12 (1968) 177.

33. F. J. Bradshaw, R. H. Brandon and C. Wheeler, Acta Met. 12 (1964) 1057.

34. G. E. Rhead, Acta Met. 13 (1965) 223.

35. R. Shuttleworth, Metallurgia 38 (1948) 125.

36. W. L. Winterbottom and N. A. Gjostein, Acta Met. 14 (1966) 1033.

37. M. McLean and H. Mykura, Surf. Sci. 5 (1966) 466.

38. M. McLean, Acta Met. 19 (1971) 387.

39. B. Mills, M.Mclean and E. D. Hondros, Phil. Mag 27 (1973) 361.

40. M. McLean, J. Mat. Sci. 8 (1973) 571.

41. B. E. Sundquist, Acta Met. 12 (1964) 67.

42. R. Gomer, in Field Emission and Field Ionization, Harvard Press (1961).

43. E. W. Müller and T. T. Tsong, Field Ion Microscopy, Principles and Applications, Elsevier (1969).

44. J. J. Hren and S. Ranganathan, Field Ion Microscopy, Plenum Press, New York (1968).

45. R. F. Hochman, E. W. Müller and B. Ralph, Applications of Field Ion Microscopy in Physical Metallurgy and Corrosion, Georgia Institute of Technology, Atlanta (1969).

46. K. M. Bowkett and D. A. Smith, Field Ion Microscopy, North Holland (1970).

47. E. W. Müller, Adv. in Elec. and Electron Phys. 13 (1960) 83.

48. A. J. Melmed, in Experimental Methods of Materials Research, Edited by Herbert Herman, Interscience (1967) 104.

49. D. G. Brandon, in Advances in Optical and Electron Microscopy, Volume 2, Edited by Barer et. al., Academic Press (1968)343.

50. A. Müller and M. Drechsler, Surf. Sci. 13 (1969) 471.

51. W. W. Mullins, Phil. Mag. 6 (1961) 1313.

52. W. M. Robertson, The Crystallography of Impurity Adsorption in Copper Surfaces, Thesis, Carnegie Inst. of Tech.(1962) cited in A. J. W. Moore, Metal Surfaces ASM Seminar (1962).

53. P. C. Bettler and F. M. Charbonnier, Phys. Rev. 119 (1960) 85.

54. P. C. Bettler and G. Barnes, Surf. Sci. 10 (1968) 165.

55. I. L. Sokolovskaia, Zh. Tekh. Fiz. 26 (1956) 1147.

56. I. L. Sokolovskaia, Izvest. Akad. Nauk, Ser. Fiz. Khim. 20 (1956) 1151.

57. I. L. Sokolovskaia, H. Neumann and E. Kloze, Fiz. Tverd. Tela 6 (1964) 1439, 1744.Translation: Sov. Phys. Solid State 6 (1964/65) 1126, 1369.

58. M. Pichaud and M. Drechsler, Surf. Sci. 32 (1972) 341.

59. A. J. Melmed, J. Appl. Phys. 38 (1967) 1885.

60. M. Drechsler and R. Vanselow, Z. Krist, 107 (1956) 161.

61. W. Maiwald and D. Stark, Naturwiss, 51 (1964) 403.

62. G. Ehrlich and F. G. Hudda, J. Chem. Phys. 44 (1966) 1039.

63. P. G. Shewmon, in Diffusion in Solids, McGraw Hill, New York (1963) 47.

64. M. Pichaud, A. Müller and M. Drechsler, Surf. Sci. 26 (1971) 14.

65. G. Meyrick, Rev. Sci. Inst. 39 (1968) 1954.

66. Handbook of Chemistry and Physics, Chemical Rubber Publishing Company, Cleveland, Ohio 38th Edition (1956) 2366.

67. G. C Bond, Surf. Sci. 18 (1969) 11.

68. L. D. Schmidt, in Adsorption Desorption Phenomena, Edited by Ricca, Italy (1971) 391.

69. G. C. Bond, in Catalysis by Metals, Academic Press, New York (1962) 7.

70. J. Y. Choi and P. G. Shewmon, Trans. AIME 224 (1962) 589.

71. I. N. Stranski and R. Shurman, Ann. Physik, Series 6, 1 (1947) 153.

VITA

Rajinder Kumar, son of Satya Devi and Ram Kishan, was born in Shahkot, Punjab, India, on February 26, 1948. After early education at Shahkot, he joined Hindu High School in Kaithal, and then Arya Higher Secondary School in Ludhiana. While at these schools he received board and state scholarships, respectively. He graduated from the Arya Higher Secondary School in April, 1964, with the sixteenth rank in the Punjab University of more than 30,000 students, and won the National Scholarship to pursue further studies. He then joined the Indian Institute of Technology in Kharagpur, India and graduated in May, 1969 with the Bachelor of Technology (Hons) degree in Metallurgical Engineering. While at the Indian Institute of Technology, he participated in many activities and was the secretary of small area games in the year 1966-67. He was an executive member of the Society of Metallurgical Engineers in the year 1967-68. He won the hostel blues for basketball, badminton and table tennis.

In September, 1969, he was admitted for graduate studies at the Georgia Institute of Technology. He received the Master of Science degree in Metallurgy in June, 1971. He coauthored a paper entitled "Surface Properties of Titanium and Titanium Alloys," which was presented in the Conference on the Stress Corrosion Cracking of Titanium (1971) held in Atlanta. He also coauthored a paper entitled "Hydrogen-ion Microscopy of Titanium", which appeared in Surface Science, 29 (1972) 447-53. He is a member of Sigma Xi and American Society of Metals.